Search for Very-High-Energy Gamma-Ray Emission from Primordial Black Holes with VERITAS

Simon Archambault

Doctor of Philosophy

Department of Physics

McGill University

Montreal, Quebec

May 13^{th}, 2016

A thesis submitted to McGill University in partial fulfillment of the requirements of the degree of Doctor of Philosophy.

“The highest activity a human being can attain is learning for understanding, because to understand is to be free.” -Spinoza

ACKNOWLEDGEMENTS

This thesis would not have been possible without the help and support of many friends, family and colleagues.

I would first like to thank Prof. David Hanna, whose mentoring over the past five and a half years has helped me reach a greater understanding and appreciation for the work required of an experimentalist. Without his invaluable insights and advice, this thesis would not be as complete or polished as it now is. His unwavering support, through both critics and praises, through a few different potential thesis topics, was instrumental in getting this done in a timely manner. Maybe now I will remember to present my figures with log scales on my axes.

I cannot write this acknowledgement without mentioning the help and support of Sujeewa Kumaratunga. She made coming home every day a delight, even during the most challenging moments of this PhD and of the writing of this thesis. Without her reassurances, support, discussions (sometimes heated) and love, I would lack the peace of mind needed to accomplish such a project.

I want to also thank my parents, who made me grow up in an environment encouraging the pursuit of knowledge and science, even if according to them I should have been done with this PhD about four years ago!

Many thanks to my friends who have provided enough distractions from the work for me not to go insane.

And to my many colleagues and fellow collaborators. Sean Griffin, whose help through a lot of my work was invaluable, as well as covering for some embarrassing incidents. Jon Tyler, whose (mostly) unfunny puns shall be missed, for some reason. Gordana Tešić, with whom the large exchange of emails made this work possible. Pascal Fortin, at the SAO (Smithsonian Astrophysical Observatory), for his support and help for many of the work I have had to do over at the VERITAS site, making the trips over there something to look forward to. I want to thank Ken Ragan, Ben Zitzer, Qi Feng, David Staszak, Étienne Bourbeau, Tony Lin, Andrew McCann, Michael McCutcheon, Gabriel Chernitsky, Samuel Trépanier and Jean-François Rajotte for many helpful and stimulating discussions.

Finally, thanks to all of the VERITAS collaboration, without their continued efforts, there would not be any experiment today, and this particular grad student would probably still be looking for a thesis topic!

This research is supported by grants from the U.S. Department of Energy Office of Science, the U.S. National Science Foundation and the Smithsonian Institution, and by NSERC in Canada. We acknowledge the excellent work of the technical support staff at the Fred Lawrence Whipple Observatory and at the collaborating institutions in the construction and operation of the instrument.

ABSTRACT

Primordial black holes are black holes that may have formed from density fluctuations in the early universe. It has been theorized that black holes slowly evaporate. If primordial black holes of initial mass 10^{14}g (or 10^{-20} times the mass of the Sun) were formed, their evaporation would end in this epoch, in a bright burst of very-high-energy gamma rays. A Cherenkov telescope experiment like VERITAS can then look for these primordial black hole bursts in its data, in the hopes of constraining the rate-density of their final evaporation. This work describes the search for such black holes, using the VERITAS telescopes, as well as developing new techniques in order to reach better limits. The 99% C.L. upper limits obtained in this work are of 2.22×10^4 pc^{-3} yr^{-1}, an improvement from previous VERITAS limits by a factor of 6, as well as from limits measured by other experiments.

RÉSUMÉ

Les trous noirs primordiaux sont un type de trous noirs qui pourraient s'être formés par des fluctuations de densité durant les premiers instants de l'univers. Il est aussi probable que les trous noirs, de façon général, s'évaporent continuellement. Si des trous noirs primordiaux avec une masse initiale de 10^{14}g (ou de 10^{-20} fois la masse du Soleil) se sont formés, leur évaporation se terminerait à notre époque, dans une explosion de rayons gamma à très hautes énergies. Des télescopes à rayonnement Cherenkov, tel que ceux utilisés par l'expérience VERITAS, peuvent chercher ces explosions de trous noirs dans leurs données, dans l'espoir de restreindre leur abondance. Le travail décrit ici détaille cette recherche de trous noirs primordiaux, utilisant les données des télescopes VERITAS, tout en développant de nouvelles techniques dans l'espoir de pouvoir atteindre de meilleures limites que celles obtenues par les mesures précédentes. Les limites supérieures obtenues dans ce travail, à un niveau de confiance de 99%, sont de 2.22×10^4 pc^{-3} yr^{-1}, une amélioration par rapport aux dernières limites obtenues par VERITAS par facteur 6, ainsi qu'à d'autres mesures de différentes expériences.

STATEMENT OF ORIGINAL CONTRIBUTIONS

The author of this thesis has made several contributions to the VERITAS experiment over the years, on a number of scientific research topics as well as on the running, maintenance, and calibration of the experiment.

This thesis is a feasibility study of the search for primordial black holes with VERITAS, using recently-developed tools. The author has studied the point-spread function of the telescopes, as well as the effect of varying time windows. He also compiled a list of runs to use for the search, developed a large portion of the analysis; for instance, the burst-finding mechanism from a given list of gamma-like events, and computing the limits from the resulting burst distributions.All of Chapters 7 and 8 details the author's contributions. Note that the author has described a new tool for the analysis (Boosted Decision Trees) in detail, but it should be specified that the development and testing of this tool was not done by the author himself, but by other members of the VERITAS collaboration.

Outside of the work covered as the main topic of this thesis, the author also developed and tested a calibration tool for the VERITAS experiment, measuring the whole-dish reflectivity of the telescopes. This work is described in an appendix of this thesis. The author was involved in every step of the development, from designing and building the apparatus, as well as installing it, testing it, and maintaining it. This apparatus is now installed on the VERITAS telescopes permanently, and it is used regularly by the VERITAS collaboration. A publication on the results from this work is in progress.

The author worked on a variety of projects throughout his PhD, not discussed in this thesis. He contributed to the analysis of a search for flaring activity from the Crab Nebula, following reports from the Fermi Gamma Ray

Space Telescope. The result of this work has since been published in [1].

The author was involved in a feasibility study for the measurement of the electron and positron Moon shadow to measure their ratio, in an effort to confirm a positron excess at VHE energies.

The author also participated in a number of presentations of his work, notably at the 2013 International Cosmic Ray Conference (ICRC) in Rio de Janeiro, as well as various CRAQ (Centre de Recherche en Astrophysique du Québec) meetings and VERITAS collaboration meetings. A presentation of the whole-dish reflectivity measurement at the 2014 CAP (Canadian Association of Physicists) conference in Sudbury, Ontario, awarded him an Honourable Mention for Best Student Oral Presentation.

TABLE OF CONTENTS

LIST OF TABLES

LIST OF FIGURES

CHAPTER 1
Introduction

Stephen Hawking has been at the forefront of studies on the behavior of black holes, and his work is the main motivation for the search carried out in this thesis. He first postulated the existence of black holes having been formed in the early universe, now known as primordial black holes (PBHs) [2], in 1971. A few years later, he postulated the possibility of black holes to be evaporating [3], similar to the behavior of a blackbody.

This has launched a field of research from different experiments, in the hopes of detecting this evaporation. One of the ways to detect these PBHs is through their emission of very-high-energy (VHE) gamma rays. This particular field of astrophysics is relatively young, having detected its first source, the Crab Nebula, in 1989 [4].

It is possible to use VHE gamma rays to look for the final evaporation of PBHs. This thesis describes such a search methodology, using the VERITAS (Very Energetic Radiation Imaging Telescope Array System) telescopes. The main purpose of this work is to study the feasibility of this type of search, using newly-developed analysis techniques and methodologies.

First, a quick description of the field of VHE gamma-ray astrophysics is given, detailing the different production mechanisms in astrophysical objects that lead to these emissions. The third chapter will then give a description of the different types of black holes that can exist, from solar-mass to supermassive ones, as well as intermediate-mass black holes. PBHs will be covered in greater detail as this is the main topic of this thesis.

Chapter four goes into the details of black hole evaporation mechanisms, and how this can be applied to PBHs. Understanding this mechanism is important for developing a search methodology. An overview of the different searches done in the past, by different experiments, in light of the information on PBH evaporation, will be given.

The VERITAS experiment, used for the search for PBHs in this work, will then be described, with a focus on its hardware and experimental technique. This will then be followed by an overview of the standard VERITAS analysis, as well as a discrimination method, boosted decision trees (BDTs), recently developed by the collaboration. BDTs, a powerful tool to remove background events, will be used extensively in the search for PBHs, as it offers a significant improvement over the standard analysis used in the past by VERITAS.

The seventh chapter will detail the specifics of the analysis on the search for PBHs, looking for bursts of gamma rays that may have come from such black holes in their final stages of evaporation. This chapter will outline the new tools used (such as BDTs, and a better understanding of the angular resolution of the detector), as well as the methods to count the bursts found in VERITAS data.

Finally, upper limits on the rate-density of the final evaporation of PBHs will be calculated from the results of the analysis, showing the improvements provided by the new analysis methods used in this work. Comparisons will be given with the results of other experiments, as well as some implications on a potential discovery of PBHs.

CHAPTER 2
Very-High-Energy Gamma-Ray Astrophysics

Very-High-Energy Gamma-Ray Astrophysics is a relatively new field of astrophysics. It originated with the discovery of cosmic rays, charged particles of high energy coming from the sky [5]. Since cosmic rays are charged, their trajectories are deflected by the magnetic fields along their paths, so they appear to be coming from random directions as seen from Earth. This means that to determine the origin of cosmic rays, some other methods need to be developed. This is why very-high-energy (VHE) gamma rays, in the GeV to TeV regime, became an interesting avenue of research, as they point back to their source, which is capable of producing high energy particles and therefore cosmic rays.

This chapter will review the different production mechanisms of gamma rays, from a particle physics point of view. Different astrophysical phenomena can provide environments for these mechanisms to take place, but this thesis will cover the production of one particular potential source of VHE gamma rays: primordial black holes (PBHs).

The methods for detecting these gamma rays will be discussed, with a quick overview of the techniques used to detect them.

2.1 Gamma-Ray Production Mechanisms

Gamma rays are the part of the electromagnetic spectrum (see Figure 2–1) above about 0.1 MeV. VHE gamma rays are a sub-band in the gamma-ray regime, in the energy range of approximately 100 GeV to 100 TeV.

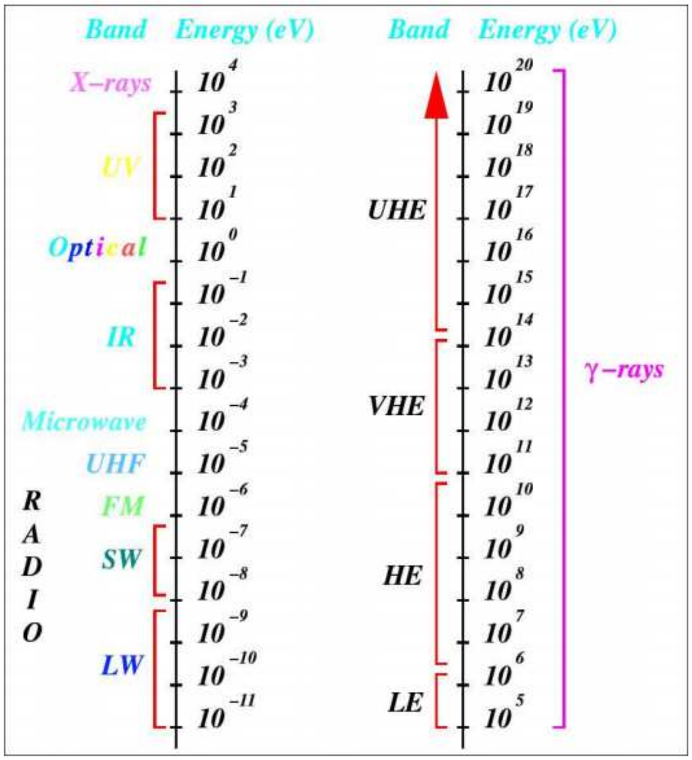

Figure 2–1: The electromagnetic spectrum. Gamma rays are the part of the spectrum starting at 0.1 MeV and above, and VHE gamma rays are defined to be between 100 GeV and 100 TeV. Figure from [6]

The question that came about when they were discovered was what processes are involved in giving photons that much energy. To answer that, one turns to particle physics to look for the typical production processes of gamma rays.

2.1.1 Fermi Acceleration

Most of the gamma-ray production mechanisms come from charged particles of high energies; so a quick look at what is involved in particle acceleration is warranted.

There are two types of charged particle acceleration in astrophysical sources. One is through a strong electric field, like one can find on the magnetosphere of a pulsar. The second one is called Fermi acceleration, and comes in two types: first- and second-order acceleration.

Ironically, the second-order process was the first one proposed, by Enrico Fermi in 1949 [7]. He postulated that charged particles could collide stochastically with gas clouds in the interstellar medium. This process would diffuse the particles and have them gain energy with each collision. The average energy gain ($\Delta E/E$) is proportional to $(v/c)^2$, with v being the gas cloud's velocity and c, the speed of light [8].

The first-order acceleration is a more efficient process, and was discovered later [9]. In this situation, it is thought that a strong shock is propagating through a diffuse medium. The charged particles in the medium go through the shock, and each time gain energy ($\Delta E/E$) proportional to (v/c), where v is the velocity of the shock wave. This results in a power-law spectrum, with index close to 2 [8]. Such shock waves are present in supernova remnants or active galactic nuclei, making this mechanism a very plausible explanation for the acceleration of charged particles.

However, these processes do present a few problems. One of them is called the "injection problem", whereby it is necessary for the particles to initially have energies larger than the thermal energies of the gases' particles. In that way, they will be able to cross the shocks and get accelerated [8]. The processes involved for the particles to reach these initial energies remain a mystery. Another problem is that this process can only accelerate the particles up to 10^{15} eV, whereas the measured cosmic ray spectrum extends all the way to 10^{20} eV [10]. Some other mechanisms are needed to explain how the particles can gain such energies.

2.1.2 Inverse Compton Scattering

One of the main VHE gamma ray production processes is Inverse Compton Scattering [11]. A low energy photon scatters off a high energy electron, which loses its energy to the photon:

$$e \; + \; \gamma_{\text{low energy}} \; \rightarrow \; e_{\text{low energy}} + \gamma_{VHE} \tag{2.1}$$

The energy of the scattered photon typically becomes:

$$E'_p \; \sim \; \gamma^2 E_p \tag{2.2}$$

where γ is the Lorentz factor from relativity ($\gamma = 1/\sqrt{1 - v^2/c^2} = E_p/m_e c^2$) of the incident charged particle, and E_p is the initial photon energy [8]. In the Thomson regime (where $\gamma h\nu \ll m_e c^2$ and $\gamma h\nu$ is the photon energy in the center-of-mass reference frame), the resulting spectrum of the scattered photons will follow a power-law of index $(1 + \alpha)/2$, if the electron population follows a power-law spectrum of index α [4].

Low-energy photons are prominent in the interstellar environment, either from thermal emission from stars or through synchrotron emission of high-energy electrons in magnetic fields. That, and the presence of astrophysical objects where electrons are accelerated through the Fermi acceleration process make this particle interaction a very common one for VHE emissions.

2.1.3 Synchrotron Radiation

Synchrotron radiation is a less important mechanism when considering VHE astrophysics; it is dominant at the lower energy ranges. A high-energy electron will emit synchrotron radiation when accelerating, in this case, when forced to travel in a curved trajectory by a magnetic field. The electron will lose some energy in the form of a gamma ray of energy E_{syn} [12]:

$$E_{syn} = 3\mu_B \left(\frac{E}{mc^2}\right)^2 B \sin\theta \quad (2.3)$$

where $\mu_B = e\hbar/2m_e c$ is the Bohr magneton, E is the electron's energy and B is the magnetic field strength.

In order for an electron to emit a photon of 1 TeV by synchrotron radiation in a relatively weak magnetic field (for example, the Crab Nebula has a magnetic field of ~ 0.1 mG [13]), it would need to be accelerated to the PeV range, but synchrotron losses will prevent it from reaching those energies.

A plausible way of reaching VHE emissions with synchrotron radiation is through synchrotron self-Compton interactions, where the electron will emit a gamma ray through synchrotron radiation, and then the gamma ray will itself scatter through inverse Compton scattering with another high-energy electron, giving it more energy.

2.1.4 Neutral Pion Decay

Not only is neutral pion decay a common process in VHE astrophysics, it is also the main contributor of gamma-ray emission from primordial black holes (PBHs, see Section 4 for an explanation of the neutral pion decay contribution to the PBHs' gamma-ray emissions). Protons and other heavier nuclei can be accelerated in astrophysical environments through Fermi acceleration, and then interact with ambient nucleons or photons. These interactions predominantly produce charged and neutral pions [4]. In the case of PBHs, pions are directly emitted by the black holes following the spectrum from Hawking radiation (see Chapter 4.1), i.e. they naturally have high energies without having to be accelerated. Charged pions will decay into muons and neutrinos 99.9% of the time, while neutral pions decay into two photons 98.8% of the time, with a lifetime of 10^{-16} seconds [14]:

$$\text{p} \ + \ \text{nucleus} \ \rightarrow \ \text{p}' \ldots + \ \pi^{\pm} \ + \ \pi_0 \ + \ldots \tag{2.4}$$

followed by:

$$\pi^0 \rightarrow 2\gamma; \ \pi \rightarrow \mu\nu_\mu; \ \mu \rightarrow e\nu_\mu\nu_e \tag{2.5}$$

Neutral pions can also decay into an electron-positron pair and a photon, 1.2% of the time. Heavier and rarer hadrons (like K mesons and hyperons) would also be produced in similar reactions. However, these processes are not as likely and tend to be neglected [4].

2.2 Detection Mechanisms

Detecting gamma rays presents an interesting challenge, as the atmosphere will absorb them and they will not make it to the ground. Two options remain, however. One is to go into space to catch them before they get absorbed by the atmosphere, and the other is to look for the result of the gamma ray's interaction with the atmosphere. Either way, particle physics interactions are very important in describing the detection methods of gamma rays. The following section will describe electron-positron pair production, interaction used by the Fermi Gamma-Ray Space Telescope [15], followed by a description of bremsstrahlung. The formation of particle showers will be described, which uses a combination of pair production and bremsstrahlung emissions. Finally, the Cherenkov radiation emitted by the shower will be explained, as it is the emission that VERITAS is looking for.

2.2.1 Pair Production

Pair production consists of the production of an electron-positron pair from a gamma ray. In order to be able to produce the pair, the gamma ray needs to have enough energy, i.e. at least twice the rest mass of the electron, for energy to be conserved. Also, to respect conservation of momentum, the process needs to occur in the electric field of a nucleus, which will absorb some of the excess momentum [4]. Pair production becomes the dominant gamma-ray interaction process at $\sim$30 MeV, and is used by detectors like the Fermi Gamma-Ray Space Telescope (see Section 4.4.2 for a short description). In that detector, the gamma ray pair-produces and the electron-positron pair is detected by tracking their paths in the detector and measuring their energies with the use of a calorimeter [15]. The pair's trajectories can be used to reconstruct the trajectory of the original gamma ray, which points back to its point of origin. Pair production is also an essential component of the development of particle showers in the atmosphere, as explained in Section 2.2.3

2.2.2 Bremsstrahlung

German for "braking radiation", bremsstrahlung is the emission of photons by an electron passing through the electric field of a nucleus, losing energy in the process (for an electron of energy E, the emitted photon would have, on average, an energy of $E/3$ [8]). In short, it decelerates the electron, hence the name "braking radiation". This interaction is also particularly important in the development of a particle shower, discussed in the next section.

2.2.3 Particle Showers

As was discussed in the previous sections, both pair production and bremsstrahlung require the presence of the electric field of a nucleus in order for the respective interactions to take place. This becomes interesting if one considers what happens when radiation (either cosmic rays or gamma rays) reach the Earth's atmosphere: they generate extensive air showers. Figure 2–2 shows a schematic of particle shower evolution, as well as a Monte

Carlo simulation showing the difference in appearances between electromagnetic and hadronic showers (in this case a photon and proton-initiated shower respectively).

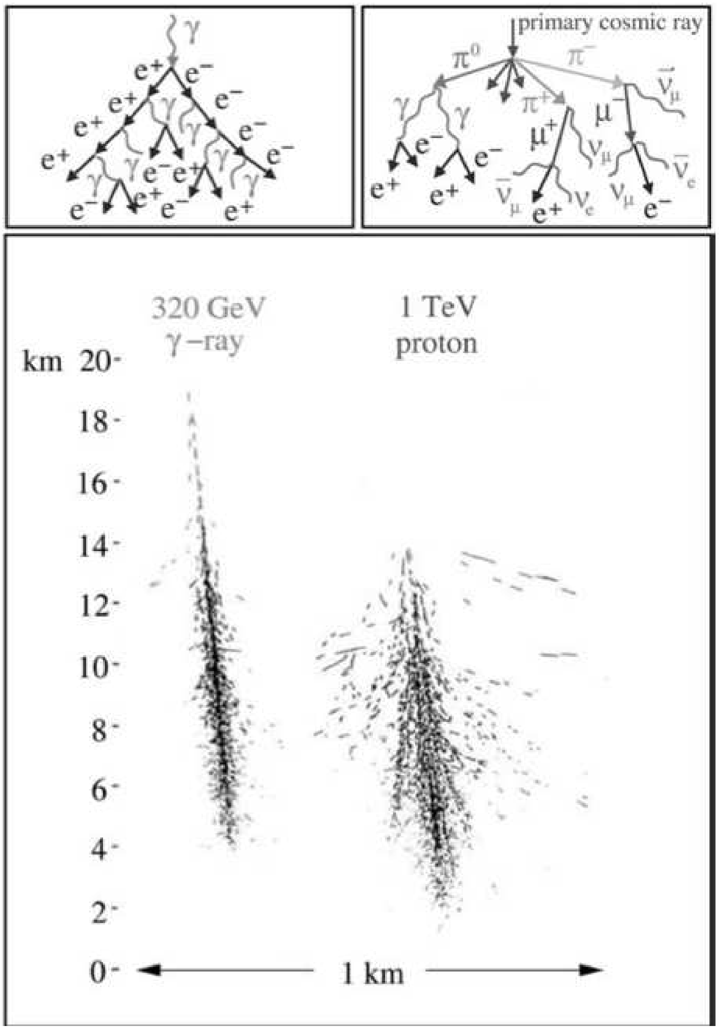

Figure 2–2: Schematic and Monte Carlo simulation of the tracks of particles in photon and proton-initiated air showers. The photon shower is more compact, with small lateral development, while the proton shower has more particles gaining transverse momentum, with some of them ending up in electrons/positrons or gamma rays creating their own electromagnetic shower. Image from [4].

In the case of a gamma-ray shower (or, more generally, an electromagnetic shower), the photon reaches the atmosphere and will pair produce into an electron and a positron. The two particles then undergo bremsstrahlung, each emitting a gamma ray, which will each pair-produce into an electron/positron pair. The newly-created electron/positron pairs will in turn bremsstrahlung and keep the cycle going. This process will end when the electrons reach an energy of E_c, the critical energy where the dominant energy loss process is through ionisation and not bremsstrahlung. The resulting particles then stop participating in the particle shower's growth [8]. Since both the electron/positron pair production and bremsstrahlung are beamed forward, the shower will be fairly narrow. Some lateral evolution will develop as the charged particles scatter with atmospheric nuclei, and deflect due to the Earth's magnetic field. Particle showers of gamma rays from 100 GeV to TeVs will reach a development maximum at about 10 km of altitude, and can reach across to a few kilometers in length [4].

In contrast, cosmic-ray showers from hadrons (primarily protons and helium nuclei) will generate particles, like pions and kaons, with large transverse momentum, which will themselves eventually decay into gamma rays or electrons/positrons and each of those will generate its own electromagnetic shower [4]. This will result in a much larger lateral propagation of the particle shower, with many different electromagnetic showers propagating at different points across that lateral distribution.

There is also the possibility of a cosmic electron or positron-generated electromagnetic shower. This will be virtually identical to the gamma-ray-induced shower, and consists of an irreducible background in the gamma ray signal. However, hadronic showers are the most dominant background, and are in principle distinguishable from electromagnetic showers. The electron background follows a power-law spectrum of index -3.3 between 10 GeV to 1 TeV

[16], and will only dominate the background at very low energies, becoming negligible in the order of a few GeVs.

Some experiments (like Milagro, or HAWC, both shortly described in Section 4.4.8) use the particles in the showers to detect gamma rays. They consist of large pools of water in which the resulting charged particles from the showers interact and cause the medium to emit Cherenkov light (described in the next section). Since most particles do not make it to the ground, those detectors are built at high-altitude in an effort to catch them before they get absorbed in the atmosphere (HAWC is built at an altitude of 4100 meters while Milagro was at an altitude of 2630 meters).

2.2.4 Cherenkov Radiation

If a charged particle moves in a medium of refractive index n, at a velocity that is faster than the speed of light in that medium (c/n), it will generate an electromagnetic shockwave, forming a light cone propagating in the same direction as the particle [8]. This shockwave is called Cherenkov radiation.

In the case of a particle shower, the generated electrons/positrons will go faster than the speed of light in the atmosphere, and will each generate Cherenkov light propagating to the ground. The angle θ of the light cone with respect to the shower propagation direction is:

$$\cos\theta = \frac{c}{n(\lambda)v} \tag{2.6}$$

where c is the speed of light, v is the velocity of the charged particle and $n(\lambda)$ is the index of refraction of air, for light of wavelength λ. The spectrum of Cherenkov photons depends on the wavelength as $1/\lambda^2$. It increases with the shorter wavelengths; however, at low wavelengths, photons get absorbed by the atmosphere, which results in a peak in the Cherenkov spectrum around 330 nm, before falling down with lower wavelengths.

Once the electrons and positrons no longer have enough energy and their velocities reach the speed of light in the air, they will stop causing the emission of Cherenkov light. This happens at energies between 20 and 40 MeV, depending on where the particles are in the atmosphere, as the air density changes and affects the index of refraction, which in turn changes the speed of light in the air. n varies with the density of air (proportionally to $n-1$), itself varying with the pressure, temperature and amount of water vapor in the atmosphere [17]. The density diminishes with altitude, which lead to n decreasing towards 1 as the altitude rises.

As mentioned in the previous section, Cherenkov radiation is used to identify the particles from a particle shower with experiments like Milagro or HAWC, where the medium is water. By contrast, experiments like VERITAS (commonly referred as Imaging Array of Cherenkov Telescopes, IACTs) use the Cherenkov emission from a particle shower in the atmosphere. The typical altitude of the maximum of the shower development is about 10 km, and with the telescopes being on the ground, the resulting light pool extends in a radius of $\sim$ 100 m. Even though the particles in the shower do not make it to the ground, the Cherenkov light they produce does, which allows the IACTs to have a lower energy threshold than the particle shower experiments. The VERITAS telescope array, as well as its detection technique, will be described in Chapter 5.

CHAPTER 3
Black Holes

A black hole is one of the most dense astrophysical objects that can be found in nature, resulting in a region in space-time where the gravitational force is so strong that nothing, not even light, can escape it. From a theory perspective, the idea of black holes has been explored as early as in 1795, by Pierre-Simon de Laplace, who described the behavior from the perspective of Newtonian gravity. Using Newton's gravitational potential energy (GMm/r), and equating it with the kinetic energy $mv^2/2$ gives one the speed v which an object of mass M, at a distance r, needs to have to escape the gravitational potential :

$$\frac{1}{2}mv^2 = \frac{GMm}{r} \tag{3.1}$$

If the speed is c, the speed of light, then there exists a radius R_g in which an object at $r < R_g$ will not be able to escape:

$$R_g = \frac{2GM}{c^2} \tag{3.2}$$

However the idea was not pursued, nor accepted by the scientific community at that time. After Einstein developed his general theory of relativity [18], Karl Schwarzschild was able to derive a solution to the Einstein equations on the behavior of the gravitational field around a central, spherical mass with no charge or angular momentum [19]. He found the radius inside which, for a given mass, light would not be able to escape. That radius is called the Schwarzschild radius, and is:

$$R_s = \frac{2GM}{c^2} \tag{3.3}$$

which is the same expression that was found using Newtonian gravity (Equation 3.2). From this equation, it can be inferred that if an object of mass M is completely contained within a radius R_s, light will be unable to escape from it.

It has been deduced that any black hole can only be described in terms of its mass, electric charge and angular momentum [20]. This is called the "no-hair theorem"; it has yet to be proven mathematically, but can be understood through reasoning. Any matter inside the event horizon is unobservable, thus cannot be used to tell the black holes apart, and all that is observable is the mass, electric charge and angular momentum. It then becomes a simple matter of classifying the different types of black holes based on their electric charge and angular momentum, as shown in Table 3–1. Each of those types corresponds to a solution to the Einstein equations, resulting in different, if similar, Schwarzschild radii.

Black Hole	Angular Momentum (J)	Electric Charge (Q)
Schwarzschild	$J = 0$	$Q = 0$
Reissner-Nordström	$J = 0$	$Q \neq 0$
Kerr	$J \neq 0$	$Q = 0$
Kerr-Newman	$J \neq 0$	$Q \neq 0$

Table 3–1: Types of black holes based on their electric charge Q and angular momentum J.

With this theory having been developed, the question then remained whether or not black holes existed, or could exist in the universe. Two types of black holes have been discovered: stellar-mass and supermassive black holes. Others have only been postulated, like primordial and intermediate-mass black holes.

3.1 Stellar-Mass Black Holes

What sort of natural process could create a black hole? Even though the description of space-time using Schwarzschild's solution to the Einstein equations is mathematically consistent, it does not necessarily mean that there would be a physical way for black holes to appear, or exist in the universe.

In 1939, Robert Oppenheimer found that a collapsed star, with a large enough mass, could be dense enough to form a black hole [21]. In essence, it opened up the idea that a star can eventually collapse on itself due to its gravitational attraction, to a point where the density is high enough that light cannot escape it.

Basically, a star is stable because of the balance between its own gravitational attraction leading towards collapse, and the nuclear reactions taking place inside the star, creating an outward pressure tending to break it apart. The nuclear reactions in the star are possible due to the presence of a fuel (usually hydrogen, though if massive enough, the star will start burning other elements). The amount of the burning element slowly diminishes, to a point where there is not enough to sustain the nuclear reactions at a level where they offset the gravitational pull. The star will collapse onto itself, raising pressure, which in turn will raise temperature to a level where the star will start nuclear reactions with a new fuel (hydrogen converts to helium, and the increasing temperature during the star's collapse will eventually ignite the helium, which becomes the new, main, fuel source). If the star is not massive enough (i.e. less than 0.1 $M_\odot$), it will simply collapse into a white dwarf, where the outward pressure balancing out gravity comes from the electron degeneracy pressure inside the star. More massive stars will reignite during collapse with a new fuel source, and the same will happen: either it will turn into a white dwarf if there is not enough mass to go to the next stage, or collapse until the pressure is large enough to trigger a nuclear reaction using the new fuel source. This continues until iron becomes the dominant fuel source. Nuclear fusion with iron actually consumes more energy than it generates, so a core-collapse becomes inevitable.

In the end, if a star has less than $\sim 10\ M_\odot$, it will eventually end its life as a white dwarf. Through their lifetime, these stars will shed their mass through solar winds, enough to have less than $1.4 M_\odot$, resulting in a white dwarf. The $1.4 M_\odot$ limit is called the Chandrasekhar limit [22]. If the mass is above $1.4 M_\odot$, the electron degeneracy pressure will not be enough to overcome the gravitational pull, and the star will undergo core-collapse through electron capture on protons to create neutrons. The collapse will result in a supernova explosion, leaving behind a neutron star, where the gravity is balanced by short-range repulsive neutron-neutron interactions (from the nuclear force, also known as the residual strong force, which becomes repulsive when the nucleons are closer than 7×10^{-16} m) and neutron degeneracy pressure. If the mass of the core after its collapse and the supernova explosion is above the Tolman-Oppenheimer-Volkoff limit (1.5 to 3 $M_\odot$)[23], then the core will keep collapsing and form a black hole[1] .

3.1.1 Experimental Evidence of Stellar-Mass Black Holes

This development in stellar evolution theory made it possible for black holes to exist, and the particular ones described here are called stellar-mass

[1] It is possible that there is one further stage between the neutron star and the black hole, the resulting stage being of a star where collapse is prevented by quark degeneracy pressure, or quark-star [24]. However this is still hypothetical and in the absence of evidence to the contrary, it is assumed that if the mass is above the Tolman-Oppenheimer-Volkoff limit, the end result is a black hole.

black holes. The next question is whether or not the theory is correct, and if there are such black holes out there.

Due to the fact that no light can escape a black hole, finding one turns out to be quite a challenge. As a matter of fact, no black holes have as of yet been *definitely* discovered. The best that can be done is to infer the presence of a black hole through its interaction with neighboring objects, like another star. This section will briefly explain the studies done on a historically relevant black hole candidate, Cygnus X-1.

Cygnus X-1 was one of the first x-ray sources to be identified, during a rocket flight in 1965 [25]. With subsequent observations, it was found that x-ray emissions varied, and the source position became better known. It was eventually associated with the star HDE 226868. Optical studies of the star found that it was orbiting a very massive object. It was so close to it, in fact, that it was found that the star's outer atmosphere is being ripped away by the companion's mass, having it spiralling towards the object, compressed by the gravitational attraction, and emitting x-rays [26]. Further observations have put the mass of the companion at $14.8 \pm 0.1\ M_{\odot}$(corresponding to a Schwarzschild radius of ~ 44 km). Furthermore, it was found that the x-ray emissions would sometimes burst for a duration on the order of a millisecond, which would indicate that the emitting region would be less than 10^2 km. This implied mass and size serves to reinforce the notion that the companion could only be a black hole [27].

No direct observations of the black hole have ever been made; in fact it would be impossible. Because of that, it cannot be said with certainty that the companion is a black hole, and over the years other models have come up trying to explain the observations [28, 29]. However, none of them has been convincing enough to put down the black hole hypothesis [30]. It remains possible that in the future, a new explanation will arise that will fit the observations better, but it is becoming more and more difficult[2] .

Other stellar-mass black hole candidates have since been found, like V404 Cygni [31], GX 339-4 [32] and V616 Mon [33], all exhibiting similar behavior to Cygnus X-1.

More recently, the LIGO collaboration has discovered the gravitational wave signature of black hole mergers. The first one involved stellar-mass black holes (both around 30 $M_\odot$)[34], and the second involving black holes of 14.2 and 7.5 $M_\odot$ [35].

3.2 Supermassive Black Holes

Supermassive black holes, which are black holes in the mass range of hundreds of thousands to billions of $M_\odot$, were originally postulated in the 1960s, with the observations of quasars, and more generally with objects called Active Galactic Nuclei (AGN)[36]. These objects are typically high-redshift galaxies, implying that they were formed in the early universe, with powerful emissions from their central cores. The inferred luminosities of these cores are $\sim 10^{12}$ times the luminosity of the Sun, produced in a small region, less than a light-year across (A Schwarzschild radius of one light-year corresponds to a black hole mass of $\sim 3 \times 10^{12} M_\odot$) . Also, the radiation in the x-ray band is highly variable on the timescale of an hour, and, remembering from

[2] In fact, Stephen Hawking, who spent quite a bit of time studying black holes, took a bet with Kip Thorne that Cygnus X-1 *is not* a black hole, despite the fact he believed the contrary. He said that winning the bet would be his consolation prize if it turned out that black holes did not exist. However, he eventually conceded the bet as the mounting evidence pointed more and more towards Cygnus X-1 being a black hole.

the similar behavior exhibited by Cygnus X-1, implies that the attributed size of the emission sites is even smaller. Only an extremely massive object (on the order of millions of solar masses) could explain this behavior, as it would cause thermal emissions due to the neighboring matter accreting into it. This would also explain the presence of collimated structures, or jets, of accelerated particles following preferred directions, consistent with jets created by black holes. Figure 3–1 shows such a jet emitted from galaxy M87, with a black hole of mass of about $3.5 \times 10^9\ M_\odot$ (corresponding Schwarzschild radius of $\sim 10^{10}$ km) [37].

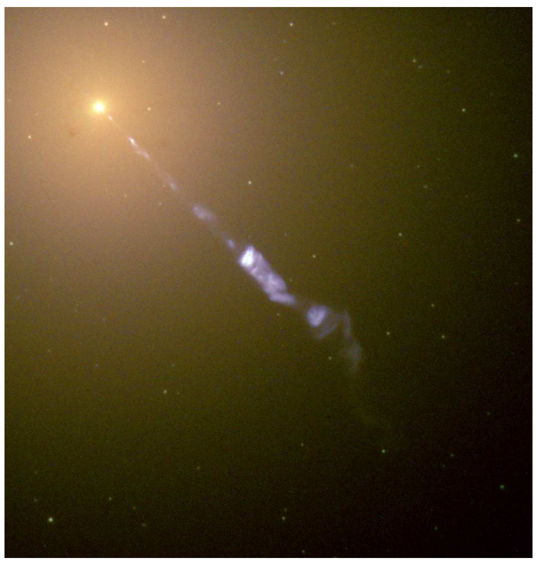

Figure 3–1: Optical image of M87, from the Hubble Space Telescope. The jet of matter ejected from the galactic center is clearly visible.

However, the most convincing argument that supermassive black holes do exist comes from observations of the movement of the stars around the center of our own galaxy (the Milky Way), in the location of the object Sagittarius A* (Sgr A*) (see Figure 3–2 for the description of the stars' orbits).

These movements suggest an object of $3.61 \times 10^6\ M_\odot$ (corresponding Schwarzschild radius of 1.1×10^7 km). The size of the object can also be

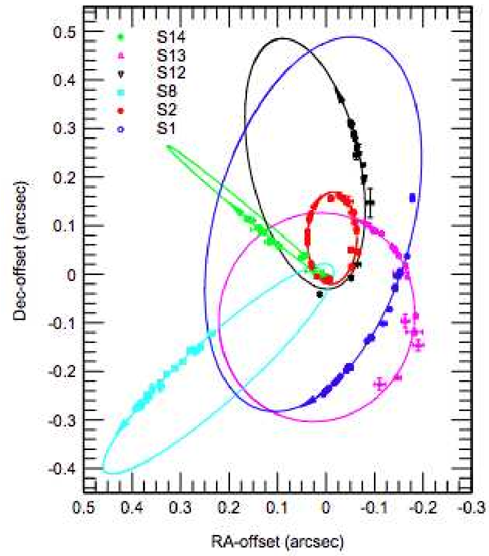

Figure 3–2: Orbits determined for 6 stars around the supermassive black hole at the galactic center, Sgr A*. From analysis of the orbits, the mass of the central object was found to be $3.61 \times 10^6\ M_\odot$. [38]

deduced to be less than 6.25 light-hours [38]. The only hypothesized astrophysical object that can have such a density is a black hole.

The origin of such black holes remains a mystery and is still being researched. An obvious hypothesis is that a stellar-mass black hole was able to accrete matter over cosmological timescales, or merge with other black holes. This would require an unusually high density of matter nearby it, and stands in seeming contradiction with the black holes from quasars at high redshift, i.e. quasars that already existed in the early universe [39]. Those imply the formation of supermassive black holes over much shorter timescales. Other potential models involve large gas clouds collapsing prior to star formation and eventually forming a supermassive black hole [40], or by local over-densities in the early universe (see Section 3.4).

3.3 Intermediate-Mass Black Holes

Intermediate-mass black holes (IMBH) are black holes in the range of 100 to 1 million $M_\odot$. The existence of such black holes remains hypothetical. As a matter of fact, no mechanism is yet known to be able to produce these black holes, as stars are not able to reach these masses. Some possibilities could be the merger of stellar-mass black holes, which could be detected by LIGO[3] , or the collision of massive stars resulting in a collapse into an IMBH [41].

The search for IMBH is focused on a few types of objects. Low-luminosity active galactic nuclei would have central black holes whose mass can be estimated around the range of IMBH [42]. Ultra-luminous x-ray sources in nearby galaxies, within star-forming regions, could be harboring IMBH [43]. Finally, the centers of globular clusters, based on the velocity measurements of their stars, could also contain them. However, other explanations can also fit with the observations, like with the G1 cluster (as seen in Figure 3–3), where the stars' velocities can fit just as well with the presence of a central massive object with lower densities than a black hole [44].

3.4 Primordial Black Holes

There is one other type of black hole that is left to be described, and is the main focus of this work. Primordial black holes (PBH) were originally hypothesized by Stephen Hawking in 1971 [2], and are still being searched for today (see Chapter 4 for the methods used to look for them, as well as a

[3] Note that the result of the 2 mergers seen by LIGO result in black hole masses of 62 $M_\odot$ [34] and 21 M_odot [35], leaving them in the stellar-mass black hole range

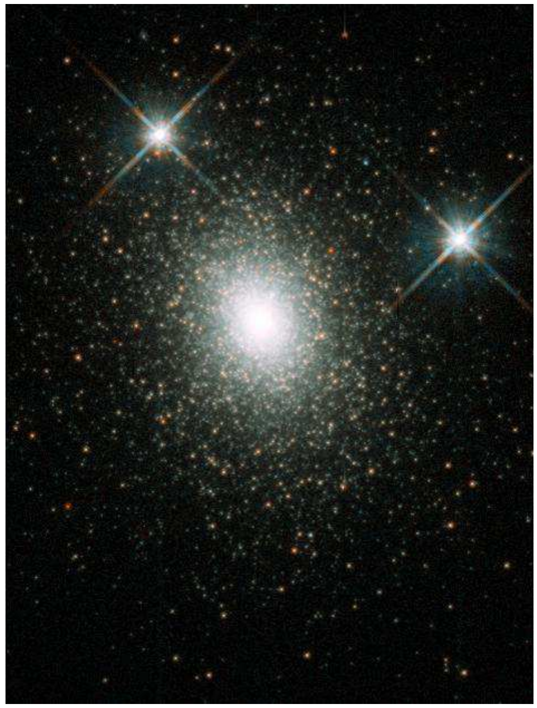

Figure 3–3: The G1 globular cluster, from the Hubble Space Telescope. At its center lies a potential candidate for an intermediate-mass black hole.

summary of what has been done thus far). They would have formed during the early universe through localized over-densities.

3.4.1 Production Mechanisms

There are three ways for these early density fluctuations to have happened: large density fluctuations, cosmic string loops and bubble collisions. The focus here will be on the large density fluctuations (see Section 3.4.3 for a description of the other models).

The first case is the one described by Carr and Hawking [45], where during the period of radiation domination (up to ∼47000 years after the Big Bang), expected density fluctuations could generate areas with a large over-density, which would collapse under the gravitational force into a PBH.

In order for that to happen, there needs to be a region where the local energy density is larger than the average density. That local density is measured with the density contrast $\delta(\vec{x})$. This can be expressed through a Fourier Transform:

$$\tilde{\delta}(\vec{k}) \;=\; V^{-1} \int_V \delta(\vec{x}) \exp(i\vec{k} \cdot \vec{x}) d^3x \tag{3.4}$$

where V is the local volume of the considered region. In the standard model of cosmology, the spectrum of fluctuations is expressed in terms of $\tilde{\delta}(\vec{k})$ as:

$$P(k) \propto k^2 |\tilde{\delta}(\vec{k})|^2 \propto k^n \tag{3.5}$$

where $P(k)$ is the power spectrum of the fluctuations and is isotropic with $k \;=\; |\vec{k}|$, and n is the power index.

This is where Carr and Hawking found the values that δ should take, in order for a local overdensity to collapse into a black hole:

$$1/3 \;\leq\; \delta \;\leq\; 1 \tag{3.6}$$

The lower limit comes from the need for the overdensity of a region to be large enough for gravity to stop it from increasing due to the expansion of the universe. This means that the size of the region R_c has to be larger than Jeans' length[4] . $R_J \;=\; \sqrt{w} \times R_H$, where w is the equation of state parameter in $p = w\rho$ with value 1/3 and R_H is the cosmic horizon radius. For the upper limit, if δ is larger than 1, it would mean that the overdensity region would collapse and form a separate closed universe. From this, it follows that the

[4] Jeans' length is the critical radius of a cloud where gravity stops its expansion

mass of the newly-formed PBH (M_{PBH}) would be on the order of the horizon mass M_H, or the mass contained within the horizon radius R_H:

$$M_{PBH} = w^{3/2} M_H \tag{3.7}$$

where M_H is the horizon mass at the time when the density fluctuations develop.

If the fluctuations turn out to be scale invariant, it would mean that PBH can form at any scale, i.e. at any point in the early universe, and therefore have a mass distribution that follows:

$$\frac{dn}{dM_{PBH}} \propto M_{PBH}^{-5/2} \tag{3.8}$$

Numerical simulations suggested that the above work was not complete. Niemeyer and Jedamzik [46] realised that, because of the near-critical gravitational collapse, the PBH mass depends on the size of the fluctuation from which it formed, at the time of its creation :

$$M_{PBH} = \kappa M_H (\delta - \delta_c)^{\gamma} \tag{3.9}$$

where γ and κ are constants of order unity. γ is the order parameter of the phase transition, and κ is a constant which depends on the spectral density fluctuation. δ_c is the critical density corresponding to the threshold for the formation of the black hole. Different calculations were made to find a value for δ_c, going from 0.3 to 0.5 [47].

3.4.2 Physics Probed by the Search for Primordial Black Holes

Primordial black holes have not yet been detected. While there is some discussion that intermediate-mass and supermassive black holes could have originated from those, it has not yet been proven. This work will describe the search for low-mass primordial black holes ($\sim 10^{14}$g, Schwarzschild radius of 10^{-16} m). In any case, whether or not PBHs are found, the result will give valuable information about the early universe.

An obvious result of a search would be on the measure of the relic density of PBHs. As will be explained in the next chapter, a PBH of initial mass of about 10^{14}g will finish its evaporation about today. Since the initial mass is proportional to the horizon mass at the time of the formation, which is itself proportional to its formation time, today's PBH evaporation rate is a probe of the relic density of PBHs in the early universe.

Taking F_{PBH} to be the fraction of regions in the early universe of mass M that collapse into PBHs, it follows that the root-mean-square amplitude of the density perturbations entering the horizon at that mass, $\epsilon(M)$, is related [48]:

$$F_{PBH}(M) \;\sim\; \epsilon(M)\exp\left[-\frac{w^2}{2\epsilon(M)^2}\right] \tag{3.10}$$

with w being the same as before, namely the equation of state parameter of the universe. Assuming the masses of PBHs extend over a wide mass range, and that radiation density scales as $(1+z)^4$ while matter density scales as $(1+z)^3$, the relic density of PBHs can be found using the present day's density:

$$\Omega_{PBH} \;=\; F_{PBH}\Omega_R(1+z) \;\approx\; 10^{18}F_{PBH}t^{-1/2} \tag{3.11}$$

where t is the formation time of the PBH in seconds, z is the redshift, and Ω_R is the cosmic microwave background density, taken to be $\approx 10^{-4}$.

PBHs can also be used to study the power spectrum of the primordial density fluctuations, giving clues to the spectral index n described in Equation 3.5. Kim, Lee and MacGibbon [49] were able to constrain the index using an initial mass function from the Carr-Hawking model (Equation 3.8), giving $n \leq 1.23 - 1.25$.

PBH constraints on the power spectrum are fairly weak, but can reach perturbation scales much smaller than that of the cosmic microwave background [50]. Furthermore, it is possible that the power spectrum k is not independent of the spectral index n, so the constraints can be much more sensitive over a wide range of scales.

Other effects of PBHs would come from their evaporation, with the particles that are emitted. PBH evaporations during the early universe could have interacted with the matter and radiation present back then, potentially modifying the cosmic microwave background [51], or having an influence in the creation of entropy [52], of baryogenesis [53] or of nucleosynthesis [54]. It could even have an impact on the Newton's gravitational constant G over cosmological timescales, according to more exotic theories [48].

It should also be mentioned that PBHs of a mass $> 10^{15}$g can serve as a potential component of dark matter in the form of cold non-baryonic dark matter (CDM). PBHs having formed before baryogenesis are therefore non-baryonic, so they would be suitable candidates [55].

However, observations of gravitational lensing and dynamical constraints rule out PBH masses of less than 10^{20}g, as a significant source of dark matter (not forgetting that below 10^{14}g, PBHs would have already evaporated). Masses greater than 10^{25}g have been constrained as well by experiments like the MACHO collaboration [56] and WMAP [57]. This leaves the range between 10^{20} and 10^{25}g to consider. A recent study has shown that that remaining window has been ruled out, based on the existence of old neutron stars in regions where the dark matter density is particularly high [58]. In [58], the authors assume that if PBHs of these masses were interacting with these neutron stars, the PBHs would fall into the neutron star's core and eventually disrupt them by rapid accretion. The continued presence of neutron stars in such regions puts sufficient constraints on PBHs of these masses to rule them out as the main component of dark matter.

3.4.3 Other Exotic Phenomena from the Early Universe

In section 3.4.1, the focus for the explanation of the PBH formation mechanism was on the large scale density fluctuations. Other methods were mentioned, namely formation through cosmic strings or bubble collisions, which will be briefly discussed here.

Cosmic string loops are a concept stemming from quantum field theory when describing the early universe. The cosmic strings themselves are topological defects that might have been formed during phase transitions[5] in those times. A number of strings may evolve, form a network, become long and intersect with each other, forming loops. It is possible that an oscillating cosmic string loop will oscillate and fall into a configuration where all its dimensions are less than its Schwarzschild radius, causing it to collapse into a PBH, with masses similar to the horizon mass [59], like in the case of large-scale density fluctuations. The mass per unit length of the string would determine how many PBHs formed, and since cosmic string loops can collapse at any point in the radiation-dominated era of the universe, it will also have an extended mass function $dn/dM_{PBH} \propto M_{PBH}^{-5/2}$.

For the bubble collisions, this is done through the first-order phase transition in the early universe. First-order phase transitions happen with the formation of bubbles, expanding and colliding until the old phase disappears

[5] Phase transitions in the early universe are periods of symmetry-breaking where the different fundamental forces begin to differentiate themselves

completely. In the early universe, these bubbles form as well, and wall collisions between bubbles can sometimes lead to the formation of PBHs with masses of the order of the horizon mass. The wall collisions will concentrate the kinetic energy within the gravitational radius, causing collapse [60]. However, very special conditions on the rate of bubble formation need to be met, in order to get enough bubble collisions to create a cosmologically interesting abundance of PBHs, without the phase transition occurring instantaneously.

3.5 Conclusion

It is now clear that black holes can exist in different types. PBHs are one of the types, and thus far have remained undetected. The topic of this thesis is on the search for such PBHs, and understanding where they come from and what they may look like now is important to achieve that goal. With this in mind, the physical behavior of PBHs needs to be understood in order to have a way to look for them.

CHAPTER 4

Search for Primordial Black Holes

Primordial black holes (PBHs) have, at this point, a strong theoretical foundation. The next step is to experimentally determine their existence. Different methodologies exist for finding them, used by various experiments across the years. An explanation of the expected behavior of PBHs will be included here, from the work done by Stephen Hawking up to the emission model describing the expected gamma-ray spectrum, followed by the experiments that have used these predictions to look for them. None of them have had any success thus far.

4.1 Hawking Radiation

As mentioned in the previous chapter, black holes have such strong gravity that not even light can escape them. So, presumably, one would not expect to be able to see emissions from a black hole. However, Hawking, while working on the thermodynamics of black holes, discovered that they could indeed emit particles [3]. In 1970, Jacob D. Beckenstein found a formula that described how the mass change dM is related to the change of the horizon surface dA, its angular momentum dJ and charge dQ [61]:

$$\mathrm{d}M \;=\; \frac{\kappa}{8\pi}\mathrm{d}A \;+\; \Omega\mathrm{d}J \;+\; \Phi\mathrm{d}Q \tag{4.1}$$

where κ is the surface gravity of the black hole, Ω is its angular velocity, and Φ, its electrostatic potential. Following this, in 1971, Hawking showed that the sum of the areas of a black hole horizon can only increase or stay constant [2]:

$$\delta A \;\geq\; 0 \tag{4.2}$$

This looks a lot like the second law of thermodynamics, stipulating that the entropy of a system can only increase or stay constant ($\delta S \;\geq\; 0$). Linking those two together, one can associate Equation 4.1 with the first law of thermodynamics:

$$\mathrm{d}E \;=\; T\mathrm{d}S \;-\; p\mathrm{d}V \tag{4.3}$$

where ΩdJ and ΦdQ represent the work portion of the equation, and the change of energy dE corresponds to the change of mass dM in Equation 4.1. This then implies that black holes have entropy, and a temperature, which allows them to radiate as a blackbody. Hawking showed that a black hole would emit particles of spin s following the spectrum [62]:

$$\frac{\mathrm{d}^2N}{\mathrm{d}E\mathrm{d}t} \;=\; \frac{\Gamma_s(ME)}{2\pi\hbar}\left[\exp\left(\frac{E \;-\; n\hbar\Omega \;-Q\Phi}{k_BT_{BH}}\right) - (-1)^{2s}\right]^{-1} \tag{4.4}$$

where E is the emitted particle's energy, and where:

$$k_BT_{BH} \;=\; \frac{\hbar c^3}{8\pi GM} \;=\; 1.06\left(\frac{M}{10^{13}g}\right)^{-1}\;\mathrm{GeV} \tag{4.5}$$

with T_B being the black hole temperature, which depends on the gravitational constant G, the reduced Planck constant $\hbar$, the speed of light c and is inversely proportional to the mass M. It is multiplied by the Boltzmann constant k_B to get an energy. Since the initial black hole rotation and its electric field are radiated away faster than the mass (the emitted particles take away angular momentum and electric charge from the PBH), one can assume Ω and Φ to be zero and get [62]:

$$\frac{\mathrm{d}^2N}{\mathrm{d}t\mathrm{d}E} = \frac{\Gamma_s(ME)}{2\pi\hbar}\left[\exp\left(\frac{E}{k_BT_{BH}}\right) - (-1)^{2s}\right]^{-1} \tag{4.6}$$

where Γ_s is the coefficient of absorption of the incident particles emitted by the black hole that would fall back in and is:

$$\Gamma_s(M_{BH}, E) = 27\left(\frac{x}{8\pi}\right)^2 \gamma_s(x) \tag{4.7}$$

with $x = 8\pi GM_{BH}E/\hbar c^3$ and $\gamma_s(x)$ tends to 1 for large x. Figure 4–1 shows the behavior of γ_s for different spin particles.

For $E \gg mc^2$, Γ_s can be approximated as [62]:

$$\Gamma_s(M_{BH}, E) = \frac{27G^2M^2E^2}{\hbar^2c^6} \tag{4.8}$$

or, when $E \to 0$, as [62]:

$$\Gamma_{1/2} = \frac{2G^2M^2E^2}{\hbar^2c^6} \tag{4.9}$$

$$\Gamma_1 = \frac{64G^4M^4E^4}{3\hbar^4c^{12}} \tag{4.10}$$

It is interesting to note that if a black hole evaporates, it means that the area A is in fact decreasing, seemingly contradicting the earlier statement linking the area with entropy. However, considering the entire entropy $S_{tot} = S_{BH} + S_{ext}$ of the whole system of the black hole and its environment solves that problem, as the whole system's entropy increases even if the black hole's decreases.

The remaining lifetime of the black hole can be found using the following equation:

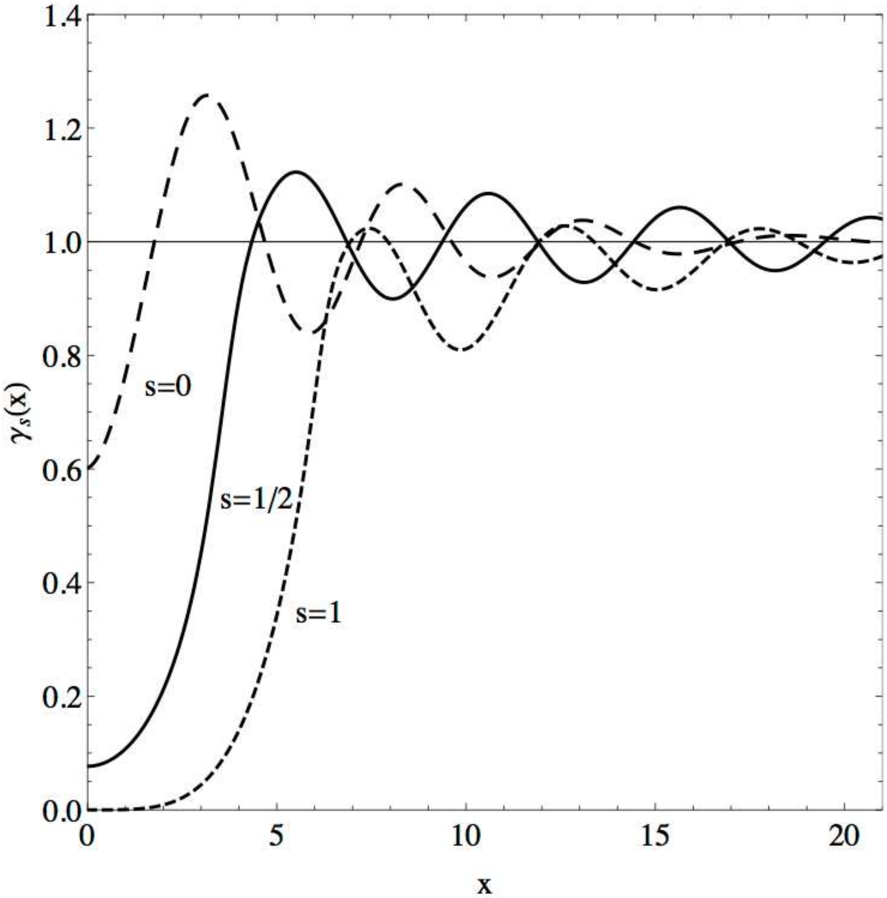

Figure 4–1: Function γ_s for spin-0, spin-1/2 and spin-1 particles. x is in units of $8\pi G M_{BH} E/\hbar c^3$. Figure from [63]

$$\frac{dM_{BH}c^2}{dt} = -\sum_i \int_0^\infty \frac{d^2N_i}{dEdt} EdE \tag{4.11}$$

where the summation over i is over all fundamental particle species, and N_i is the number of particles of species i. We can then rewrite Equation 4.11 as [63]:

$$\begin{aligned}
\frac{dM_{BH}c^2}{dt} &= -\int_0^\infty d_0(E)\frac{d^2N}{dEdt} \times EdE - \int_0^\infty d_{1/2}(E)\frac{d^2N}{dEdt} \times EdE \\
&\quad - \int_0^\infty d_1(E)\frac{d^2N}{dEdt} \times EdE \\
&= -\frac{\alpha(M)}{M^2}\text{gs}^{-1}\text{for constant } d_s(E \propto M^{-1})\text{above a certain energy}
\end{aligned} \tag{4.12}$$

where the summation has been developed, showing the particle species confirmed from the Standard Model, with d_s representing the number of degrees of freedom available to emitted particles of spin s at energy E. Degrees of freedom, in general, are the possible value of the quantum numbers of a given particle. In other words, they are the properties that distinguish one particle from another. For leptons, for example, the degrees of freedom come from the spin states as well as their antiparticles. For quarks, they are the spins, the colors and their antiparticles. Here, $d_s(E \propto M^{-1})$ is assumed constant above a certain energy. Each emitted particle reduces the mass of the black hole by an amount equivalent to E/c^2. Here, we only consider fermions of spin 1/2, and bosons of spin 1 and 0 (for the newly-discovered Higgs boson). The expression $\alpha(M)$ is given by [64] :

$$\alpha(M) = 5.34 \times 10^{25}(0.267d_0 + 0.147d_{1/2}^{q=\pm e} + 0.142d_{1/2}^{q=0} + 0.060d_1)\text{g}^3\text{s}^{-1} \tag{4.13}$$

Figure 4–2 shows the evolution of $\alpha(M)$ with the mass of the black hole. It increases in value as degrees of freedom become available with the diminishing mass and increasing temperature of the black hole during its evaporation.

In the case of the search for PBHs done here, when looking at the very end of the black hole evaporation, the mass will be low enough (or the temperature

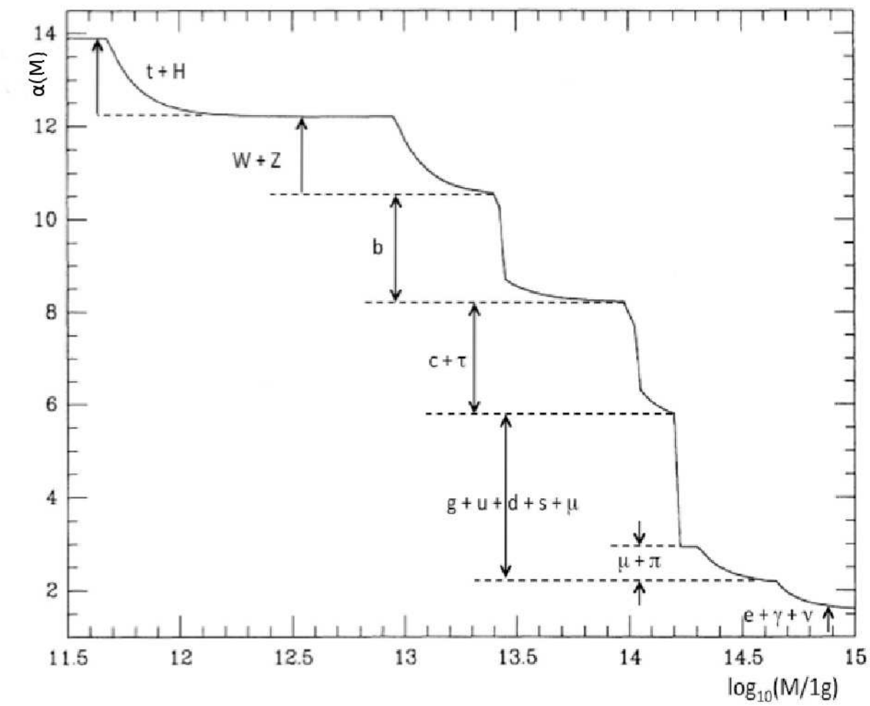

Figure 4–2: Evolution of $\alpha(M)$ with the mass of the PBH as it evaporates. As the black hole's mass diminishes, its temperature increases and new degrees of freedom become available and $\alpha(M)$ increases. Note that the term 5^25 has been taken out on the y-axis, explaining the difference in the values with that of Equation 4.13. Figure from [65].

high enough) to include all known Standard Model particles. The considered particle degrees of freedom are from the three charged leptons (6 when including antileptons $\times$ 2 spins states gives $d_{1/2} = 12$), the 3 neutrinos (6 $\times$ 2 spin gives $d_{1/2} = 12$), the six quark flavors (12 $\times$ 2 spin $\times$ 3 colors $d_{1/2} = 72$), the photon (spin 1, $d_1 = 2$), the gluons (8 gluons of spin 1, $d_1 = 16$), the $W^{\pm}$ and Z^0 (3 particles of spin 1, so $d_1 = 9$) and the Higgs boson (spin 0, $d_0 = 1$). This gives a total of $d_{1/2} = 96$, $d_1 = 27$ and $d_0 = 1$, resulting in $\alpha(M) \approx 8.5 \times 10^{26} \mathrm{g}^3\mathrm{s}^{-1}$, towards the last few moments of a PBH's lifetime.

Integrating Equation 4.12, the leftover mass of a black hole after a time t is:

$$M(t) \; = \; (M_i^3 - 3\alpha t)^{1/3} \tag{4.14}$$

with M_i being the initial mass of the black hole. The lifetime τ of a black hole is then expressed as:

$$\tau \; = \; \frac{M_i^3}{3\alpha} \tag{4.15}$$

Calculations from MacGibbon in [64] give:

$$\tau \; \approx \; 0.33 M_i^3 \alpha(M_i)^{-1} s \tag{4.16}$$

where $\alpha(M_i)$ is the average value of $\alpha(M)$ over the lifetime of a PBH of initial mass M_i.

This gives interesting information about the remaining lifetime of a black hole. For instance, for a solar-mass black hole ($1M_\odot = 2 \times 10^{33}$g), it will take about 10^{66} years to evaporate, much longer than the age of the universe (13.8×10^9 years); a black hole of 4×10^{11}g will take about a year, whereas a PBH of $\sim 5 \times 10^{14}$g will take about the current age of the universe to evaporate.

4.2 Evaporation and Phenomenology

As mentioned previously, emission of particles from an evaporating black hole follows Hawking radiation as described by Equation 4.4. This equation describes the spectrum of any of the particles emitted by the black hole. For what concerns us here, we want to take into account emissions that result in gamma rays. This will occur through two products, one being from direct photon emission, and the other through fragmentation products of other particles (here the contribution from the Higgs boson will be ignored, as its contribution will be negligible to the resulting spectrum [63]). This section will explain the dominant emission model from the Standard Model of particles, which will give the expected spectrum from evaporating PBHs, itself necessary when calculating limits on the local rate-density of their evaporation. Another, more extreme and largely disfavored model will also be explained.

4.2.1 Standard Model

In order to get the photon emission spectrum, the first step is to integrate the Hawking radiation spectrum from Equation 4.6 with respect to the time of evaporation Δt left:

$$\begin{aligned} \frac{dN}{dE} &= \int_{\Delta t}^{0} \frac{d^2N}{dtdE}dt \\ &= \frac{1}{2\pi\hbar\alpha}E^{-3}\int_{0}^{M(\Delta t)E} dx\ f_s(x) \end{aligned} \tag{4.17}$$

where α is the expression $\alpha(M)$ from Equation 4.12 and given in Equation 4.13. $f_s(x)$ is a rewriting of Hawking radiation from Equation 4.6, taking the dimensionless quantity $x = E/8\pi k_B T_{BH} = GM_{BH}E/\hbar c^3$ for integration purposes, and is expressed as:

$$f_s(x) \;=\; x^2\Gamma_s(x)\left[\exp(8\pi x) - (-1)^{2s}\right]^{-1} \tag{4.18}$$

and s is the spin of the emitted particles. That function is shown in Figure 4–3 for particles of spin 1 and 1/2 (recall from Equation 4.7 and Figure 4–1 that the behavior is spin-dependent).

To solve Equation 4.17 analytically, $f_s(x)$ is approximated as a delta function :

$$f_s(x) \;\approx\; \delta(x - x_{max,s}) \tag{4.19}$$

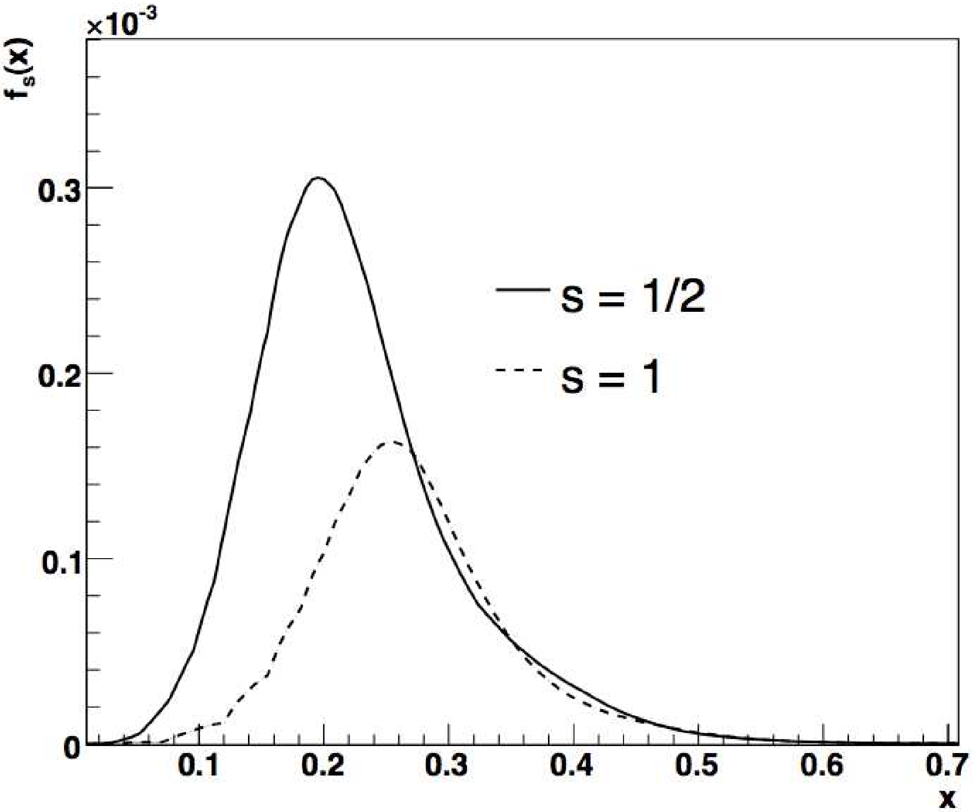

Figure 4–3: Function $f_s(x)$, from Equation 4.17. The behavior of particles of spin 1 and 1/2 are shown. x is expressed in units of $8\pi G M_{BH} E/\hbar c^3$. Figure from [65]

where $x_{max,s}$ is where $f_s(x)$ is maximal; $x_{max,1/2} = 0.195$ and $x_{max,1} = 0.252$. This corresponds to an energy of:

$$Q_s = \frac{x_{max,s}}{(3\alpha\Delta t)^{1/3}} \tag{4.20}$$

where Δt is the time left before the complete evaporation, in seconds.

From this point on, we will use $Q_s = Q_{1/2} = Q$ for particles of both spins 1/2 and 1, and will be approximated as $Q \approx 4 \times 10^4 (\Delta t)^{-1/3}$ GeV. Using this approximation for integrating Equation 4.17, one gets:

$$\frac{dN}{dE} = \frac{C_s}{2\pi\hbar\alpha} E^{-3} \Theta(E - Q) \tag{4.21}$$

where $\Theta(x)$ is the Heaviside "step" function and C_s is a normalization constant equal to the integral of $f_s(x)$ without approximation:

$$C_s \;=\; \int_0^\infty f_s(x)\; dx \tag{4.22}$$

It depends on the absorption coefficient $\Gamma_s(x)$ and has been numerically evaluated in [62] to give $C_{1/2} = 4.9 \times 10^{-5}$ and $C_1 = 2.6 \times 10^{-5}$.

The photon spectrum from PBH emissions then follows Hawking radiation. However, it will not just emit photons directly, but quarks and gluons as well. The quarks and gluons will then fragment into hadrons. For the photon emissions, we only care about the hadrons that decay into photons, and as discussed in Section 2.1.4, this decay generally comes from neutral pions (other hadrons, such as kaons, are much rarer products and are negligible). The resulting spectrum will then include the emissions from those decaying neutral pions as well as the direct photon emissions.

The direct photon contribution to the spectrum is simply given by Equation 4.21, multiplied by 2 for the different helicity states of the photon. The indirect contribution is a little more challenging, but it can be done in two steps.

First, we use Equation 4.21 to get the spectrum of emitted quarks and gluons (dN_{qg}/dE_{qg}), without forgetting to take into account the degrees of freedom of each. For the quarks, there are 72 degrees of freedom (6 flavor of quarks, times 2 spin states, times 3 colors, times 2 for the antiquarks) and 16 for the gluons (8 gluons times 2 spin states):

$$\frac{dN_{qg}}{dE_{qg}} \;=\; \frac{72C_{1/2} + 16C_1}{2\pi\hbar\alpha} E^{-3}\Theta(E - Q) \tag{4.23}$$

Those quarks and gluons will hadronize into pions which will then decay into photons. The fragmentation function this follows has been determined empirically in [66] in 1983, using results from the PETRA particle accelerator at DESY, and is:

$$\frac{dN_\pi}{dz} = \frac{15}{16} z^{-3/2}(1-z)^2 \tag{4.24}$$

where $z = E_\pi / E_{jet}$ is the fraction of the energy taken by the pion (E_π) from the jet energy (E_{jet}), a jet being a cone of hadrons from the hadronization of quarks and gluons. It is used to give the resulting pion spectrum from the emitted quarks and gluons. So, the new integral becomes:

$$\begin{aligned} \frac{dN_\pi}{dE_\pi} &= \frac{72C_{1/2} + 16C_1}{2\pi\hbar\alpha} \frac{15}{16} E_\pi^{-3/2} \\ &\times \begin{cases} \int_Q^\infty E_{jet}^{-5/2} \left(1 - \frac{E_\pi}{E_{jet}}\right)^2 dE_{jet} & \text{for } E_\pi < Q \\ \int_{E_\pi}^\infty E_{jet}^{-5/2} \left(1 - \frac{E_\pi}{E_{jet}}\right)^2 dE_{jet} & \text{for } E_\pi \geq Q \end{cases} \end{aligned} \tag{4.25}$$

Since this equation is time-integrated, it means that this is the total spectrum over the remaining lifetime of the PBH. From a single quark or gluon, the pion energy E_π will always be less than the jet energy E_{jet}, but E_{jet} can only have a minimum energy of Q. This leads to the first part of the equation, with the lower integral bound of Q. If E_π is above Q, then the minimum E_{jet} will be $E_\pi > Q$, leading to the second term in Equation 4.25.

The next step is to get the photon spectrum from the resulting pions. This is expressed as:

$$\frac{dN_\gamma}{dE_\gamma} = \frac{2}{3} \begin{cases} \int_{E_\gamma}^{Q} \frac{1}{E_\pi} \frac{dN_\pi}{dE_\pi} dE_\pi & \text{for } E_\gamma < Q \text{ and } E_\pi > Q \\ \int_Q^\infty \frac{1}{E_\pi} \frac{dN_\pi}{dE_\pi} dE_\pi & \text{for } E_\gamma < Q \text{ and } E_\pi < Q \\ \int_{E_\gamma}^\infty \frac{1}{E_\pi} \frac{dN_\pi}{dE_\pi} dE_\pi & \text{for } E_\gamma > Q \end{cases} \tag{4.26}$$

where E_γ is the energy of the gamma ray, and dN_π/dE_π comes from Equation 4.25. The 2/3 factor comes from the need to multiply by 2 for the 2 photons that come from the pion decay ($\pi \to 2\gamma$), and divide by 3 since only one of the 3 pions is a π^0 and only the neutral pion decays to gamma rays.

The different parts of the equation are defined by the energy of the pion E_π. The photons will be generated by pions with a minimum energy at E_γ. For photons with energy larger than Q, any pions with energies from E_γ will be used, hence the integral starts at E_γ. For a photon energy of less than Q, both the pion contribution below and above Q contribute, and need to be summed together. This leads to (shown in Figure 4–4):

$$\begin{aligned} \frac{dN_\gamma}{dE_\gamma} &= 2.4\times 10^{37}\left(\frac{\mathrm{GeV}}{Q}\right)^3 \\ &\times \begin{cases} \left[\frac{5}{12}\left(\frac{E_\gamma}{Q}\right)^{-3/2} - \frac{3}{2}\left(\frac{E_\gamma}{Q}\right)^{-1/2} - \frac{15}{28}\left(\frac{E_\gamma}{Q}\right)^{1/2} + \frac{5}{3}\right]\ \mathrm{GeV}^{-1} & \text{for} E_\gamma < Q \\ \left(\frac{Q}{E}\right)^3\left[\frac{1}{21}\right]\ \mathrm{GeV}^{-1} & \text{for} E_\gamma \geq Q \end{cases} \end{aligned} \tag{4.27}$$

Integrating one step further over dE_γ starting from a threshold energy E_{th}, one gets (see Figure 4–5):

$$\begin{aligned} N_\gamma(\geq E_{th}) &= 2.4\times 10^{37}\left(\frac{\mathrm{GeV}}{Q}\right)^2 \\ &\times \begin{cases} \left[\frac{5}{14}\left(\frac{E_{th}}{Q}\right)^{3/2} + 3\left(\frac{E_{th}}{Q}\right)^{1/2} + \frac{5}{6}\left(\frac{E_{th}}{Q}\right)^{-1/2} - \frac{5}{3}\left(\frac{E_{th}}{Q}\right) - \frac{5}{2}\right] & \text{for } E_{th} < Q \\ \left(\frac{Q}{E_{th}}\right)^2\left[\frac{1}{42}\right] & \text{for } E_{th} \geq Q \end{cases} \end{aligned} \tag{4.28}$$

The one last step is to include the direct photon contribution to the spectrum, which results in (also plotted in 4–4):

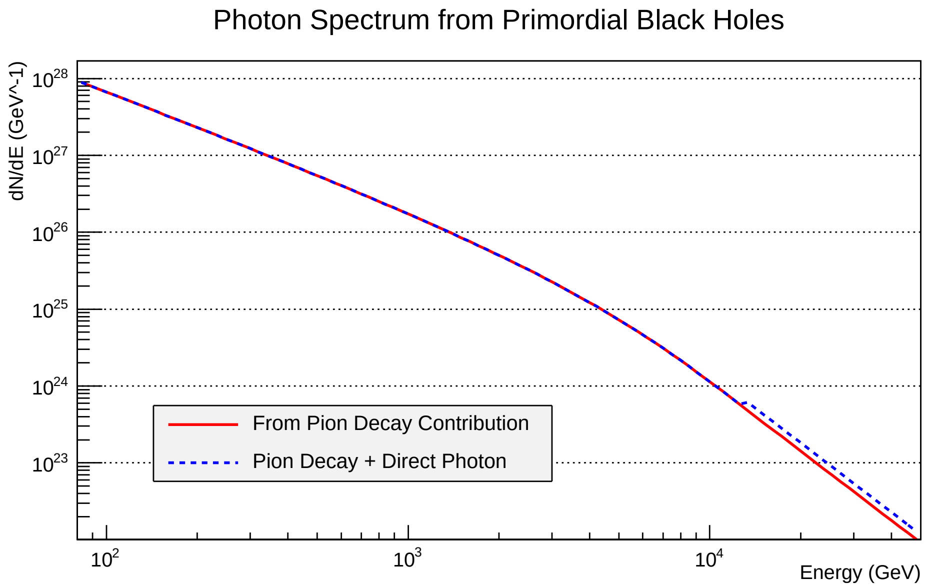

Figure 4–4: Gamma-ray spectrum of PBH from jet fragmentation and subsequent pion decay (red line), and spectrum with the direct photon emission added (blue dashed line). The spectrum shown is for PBHs with less than 30 seconds before their evaporation ends.

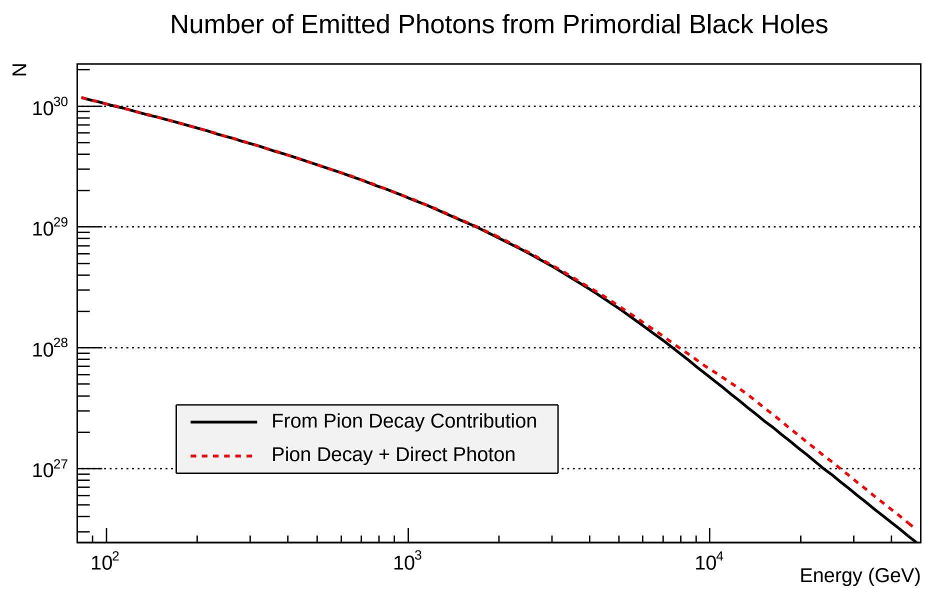

Figure 4–5: Number of gamma rays above an energy threshold E_{th} from jet fragmentation and subsequent pion decay (red line), as well as the curve with the direct photon emission added (blue dashed line). The curves shown are for PBHs with less than 30 seconds before their evaporation ends.

$$\frac{dN_\gamma}{dE_\gamma} = 2.4\times 10^{37}\left(\frac{\text{GeV}}{Q}\right)^3 \times \begin{cases} \left[\frac{5}{12}\left(\frac{E_\gamma}{Q}\right)^{-3/2} - \frac{3}{2}\left(\frac{E_\gamma}{Q}\right)^{-1/2} - \frac{15}{28}\left(\frac{E_\gamma}{Q}\right)^{1/2} + \frac{5}{3}\right] \text{GeV}^{-1} & \text{for} E_\gamma < Q \\ \left(\frac{Q}{E}\right)^3 \left[\frac{1}{21}+\frac{1}{75}\right] \text{GeV}^{-1} & \text{for} E_\gamma \geq Q \end{cases} \tag{4.29}$$

which is simply the last term in the $E_\gamma \geq Q$ range. The photon contribution is calculated directly from Equation 4.21. Recall that Q comes from Equation 4.20, and depends on the spin of the particle. The approximation made here is that Q is the same for spin 1/2 and spin 1 particles, hence, for the purposes of this work, the direct photon emission is assumed to start at the same time and follow the same spectrum as the quark emissions. This means that the direct photons will only contribute to the spectrum at an energy above Q, as shown in Equation 4.29, and illustrated in Figure 4–4 with the step at energy Q.

The total number will be (see Figure 4–5):

$$N_\gamma(\geq E_{th}) = 2.4\times 10^{37}\left(\frac{\text{GeV}}{Q}\right)^2 \times \begin{cases} \left[\frac{5}{14}\left(\frac{E_{th}}{Q}\right)^{3/2} + 3\left(\frac{E_{th}}{Q}\right)^{1/2} + \frac{5}{6}\left(\frac{E_{th}}{Q}\right)^{-1/2} - \frac{5}{3}\left(\frac{E_{th}}{Q}\right) - \frac{5}{2} + \frac{1}{150}\right] & \text{for } E_{th} < Q \\ \left(\frac{Q}{E_{th}}\right)^2 \left[\frac{1}{42}+\frac{1}{150}\right] & \text{for } E_{th} \geq Q \end{cases} \tag{4.30}$$

This is the result that was used in the past by [65] and [67][1] .

Even with the approximation that the scaled energy distribution of quark flux $f_s(x)$ in Equation 4.18 is described by a delta function, the analytical solution

[1] After correction of typographical errors, in the $E_{th} \geq Q$ conditions, confirmed by [65] and the author of this work.

derived here is reasonably accurate at low energies, as noted in [63]. However, the authors of [63] have also noted that, when $E_\gamma > 0.1Q$, errors of up to 30% appear, and the power-law fall-off at the highest energy is strongly overestimated.

Still in [63], the authors note that [68] was able to get its parameterization using a HERWIG-based[2] Monte Carlo simulations of the photon flux from 1 GeV $\leq T_{BH} \leq$ 100 GeV black holes and gives:

$$\frac{dN_\gamma}{dE_\gamma} \approx 9 \times 10^{35} \times \begin{cases} \left(\frac{1\text{GeV}}{T_\tau}\right)^{3/2} \left(\frac{1\text{GeV}}{E_\gamma}\right)^{3/2} \text{GeV}^{-1} & \text{for } E_\gamma < kT_\tau \\ \left(\frac{1\text{GeV}}{E_\gamma}\right)^{3} \text{GeV}^{-1} & \text{for } E_\gamma \geq kT_\tau \end{cases} \tag{4.31}$$

where T_τ is the temperature of the black hole at the beginning of the final burst time interval, $T_\tau = T_{BH}(\tau)$:

$$kT_{BH}(\tau) = 7.8 \left(\frac{\tau}{1\text{s}}\right)^{-1/3} \text{TeV} \tag{4.32}$$

Figure 4–6 shows the behavior of that spectrum. This can be compared with Figure 4–7 which shows the result from the direct calculation. The authors of [63] note that this equation agrees well with their own direct calculations, and is good to use for comparing the different search methods from different gamma-ray observatories. This is the equation that was used by Milagro in their own searches, as well as when estimating the HAWC sensitivities [70] (more on that in section 4.4.8). The work in this thesis will use Equation 4.31 for computing the upper limits on the rate-density of PBH evaporation.

---

[2] HERWIG (Hadron Emission Reactions With Interfering Gluons) is a Monte Carlo event generator used in high-energy physics to simulate particle physics interactions [69].

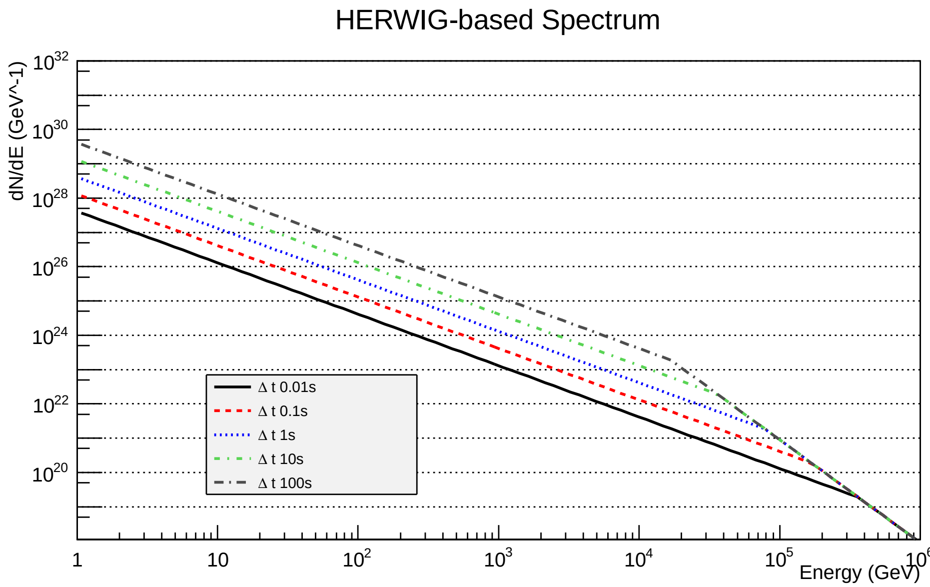

Figure 4–6: The photon spectrum, integrated over the final evaporation lifetime interval $\tau = 100, 10, 1, 0.1$ and 0.01s, from Equation 4.31. This can be compared with Figure 4–7, from the direct calculation in [63]. Note that the two plots show almost the same behavior, indicating agreement between Milagro's simulated spectrum and the calculated one.

It is interesting to note that, in general, the final stage of PBH evaporation is typically called a burst, because of the time evolution of the evaporation. One can calculate the PBH burst light curve:

$$\left[\frac{dN_\gamma}{dt}\right] = \int_{E_{min}}^{E_{max}} \frac{d^2 N_\gamma}{dE_\gamma dt} dE_\gamma \tag{4.33}$$

with E_{min} and E_{max} set by the energy range of the detector. Figure 4–8 shows the PBH burst time profile above an energy threshold of 100 GeV. One can see a rapid increase when the remaining PBH lifetime comes close to zero, indicative of a burst behavior. Note also that once the PBH has fully evaporated, no more emissions are expected, so the drop-off after the peak should be instantaneous.

4.2.2 Alternate Model

Another model that has been hypothesized for the behavior of the evaporation of primordial black holes, and used in some searches, is the Hagedorn Model [71, 72].

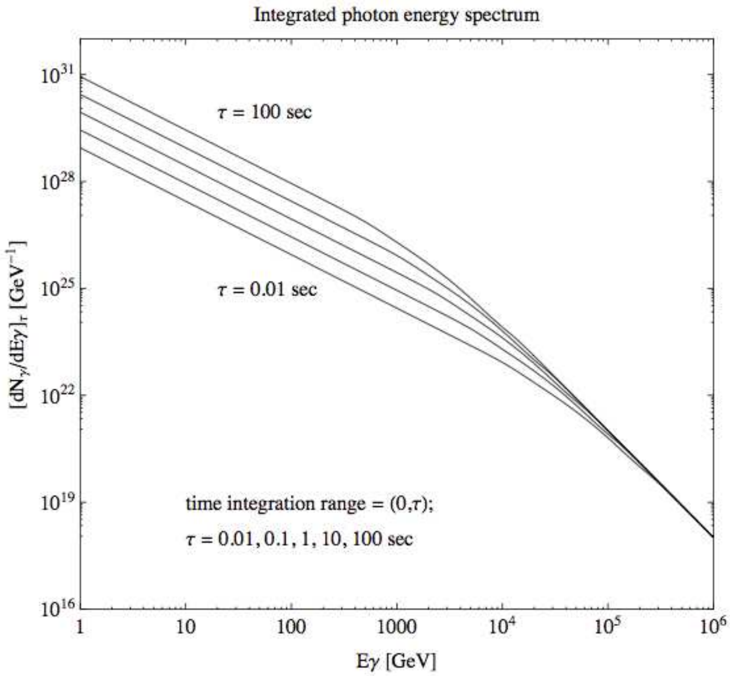

Figure 4–7: The photon spectrum from the parameterization done on the direct calculation from [63], shown for final evaporation lifetime interval $\tau = 100, 10, 1, 0.1$ and 0.01s.

The model predicts that the degrees of freedom will increase exponentially with energy:

$$d(E) \ \propto \ E^{-5/2} \exp\left(\frac{E}{\Lambda}\right) \tag{4.34}$$

where Λ is the energy scale. It was unknown at the time what the energy scale should be, the assumption being that it was above what the experiments at the time could measure. It was originally taken to be 160 MeV [67], however nowadays the value used would be the QCD confinement scale (~250 MeV). This means that the number of degrees of freedom will increase much faster than that of the standard model, resulting in much higher primordial black hole luminosity once the energy reaches $\sim 2.5\Lambda$. This will result in much stronger emissions during the final burst, confined to lower photon energies ($\lesssim$ 1 GeV) and a much shorter timescale ($\sim 10^{-7}$s).

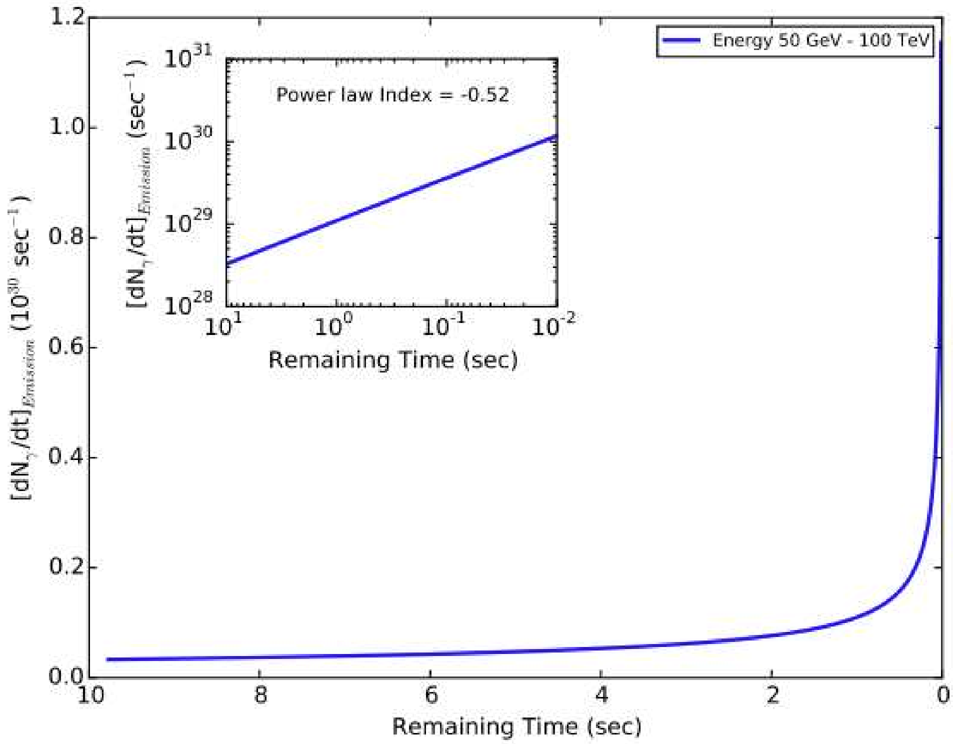

Figure 4–8: PBH burst light curve dN/dt. The rapid increase as the remaining PBH lifetime comes to zero is indicative of the burst. The inset shows the same light curve in a log-log plot. The shape is well-described by a power law with index ≈-0.5. Figure from [63].

This model was developed in the 1960's to explain strong interactions in particle physics, before accelerator collisions were able to produce data on that topic. It was based on thermodynamics, where Hagedorn noted that as the energy of a system increased, it would create new particles and increase the entropy of the system, as opposed to the temperature (as used in the standard model).

This model has been largely disfavored with the discovery of quark and gluon jets in accelerator collisions above the QCD scale Λ_{QCD}, which disproved the assertions from the Hagedorn model compared with the standard model.

4.3 Differentiating gamma-ray and primordial black hole bursts

The behavior of the final burst of PBH evaporation is essentially a burst of gamma rays over a short period of time. When searching for them, one has to wonder if they have not already been found when considering GRBs, which are commonly detected. A number of characteristics differentiating between the two types have been found, and are summarized in Table 4–1 and found in [63]. The main points are that a GRB typically shows an afterglow in the optical waveband, which is not expected from a PBH. GRBs have a cutoff in their spectra due to the interaction of gamma rays with the extragalactic background light (EBL), since GRBs are cosmological. Gamma rays interact with the EBL via pair production, leading to an attenuation of the gamma ray emissions at cosmological scales [73]. Since a PBH's spectrum extends well above 1 TeV, that component would not have been absorbed since the measured evaporation would likely be local. Finally, the spectra of GRBs show a hard-to-soft evolution whereas a PBH should show a soft-to-hard evolution.

In any case, the favored models explaining GRBs involve either supernovae or hypernovae[3] (for the long bursts), and compact object mergers, i.e. between neutron stars or black holes (for the short bursts) [74].

4.4 Previous Searches

The searches done thus far have not found any PBHs, setting upper limits on the rate-density of their final bursts. The different experiments have interpreted their data within the framework of the two models discussed in the previous section,

[3] Hypernovae are similar to supernovae, but with substantially higher energy. They are also known as superluminous supernovae.

Gamma-ray Bursts (GRB)	Primordial Black Hole Bursts
Detected at cosmological distances	Unlikely to be detected outside our Galaxy
Time duration can range from fraction of seconds to few hours	Time duration is most likely less than few seconds
May have multi-peak time profiles	Single-peak time profile
Typically a single peak shows Fast RiseExponential Decay (FRED) time profile	Power-law Rise Fast Fall (PRFF) time profile expected
X-ray, optical, radio afterglows are expected	No multi-wavelength afterglow is expected
Most GRBs show hard-to-soft evolution	Soft-to-hard evolution is expected from PBH bursts
Cosmic-rays are not expected to arrive from GRBs	Cosmic-ray bursts are expected from nearby PBH bursts
Gravitational wave signal is expected	No gravitational wave signal is expected
Neutrino burst may be seen	Simultaneous neutrino burst may be seen from nearby PBH
TeV radiation may be cut off either at the source or by the intergalactic medium	TeV signal is expected during the last seconds of the burst

Table 4–1: Main differences between signals from standard cosmological GRBs and primordial black hole bursts.

i.e. the standard and the Hagedorn model. A brief summary of the different searches will be given here.

4.4.1 SWIFT

Swift is a space telescope dedicated to mutli-wavelength studies of gamma-ray bursts, in gamma-ray, x-ray, ultraviolet and optical wavebands [75].

Swift was not built to search specifically for PBH evaporation, but it contributed to the discovery, along with other telescopes (such as BATSE, the Burst and Transient Source Experiment that was installed on the Compton Gamma Ray Observatory (CGRO)), of a new class of GRBs, called very short gamma-ray bursts (VSGRB) [76]. GRBs (detailed in section 4.3) typically come in 2 types: short (less than 2 seconds) and long (more than 2 seconds). VSGRBs are the new type that is proposed in [76], for GRBs of less than 100 ms. Isolating these VSGRBs has shown some behavior that fits with what is expected from PBH bursts. The authors of [76] find an anisotropy in the distribution of VSGRB, in opposition with regular GRBs. This anisotropy is clustered close to the Galactic anti-center region, suggesting that VSGRBs have a local origin.

The spectra of VSGRBs are harder than that of GRBs, suggesting again a difference in the population, and harder spectra are expected from PBH bursts. Finally, GRBs typically have an afterglow, but only 25% of the observed VSGRBs show any, which is a behavior expected from PBHs, that are not expected to show any afterglow. The one problem, however, as mentioned in [74], is the time profile of the gamma-ray burst. The PBH evaporation models do not predict variation in the time profile of the PBH emission from one PBH to the next. The VSGRB sample shows a variety of shapes, which would rule out the possibility of those to be from PBHs. The favored explanation for VSGRBs is the mergers of two neutron stars with low total mass.

4.4.2 Fermi

The Fermi Gamma-Ray Space Telescope [15] was placed in orbit in June 2008. It has two instruments aboard, the Large Area Telescope (LAT) and the Gamma-Ray Burst Monitor (GBM). The LAT is what was used by Fermi to look for PBHs [77]. The LAT covers an energy range from 20 MeV to 300 GeV, and is a successor to EGRET (Energetic Gamma Ray Experiment Telescope), which was in operation from 1991 to 2000 and was also used to look for PBHs, with less sensitivity. The LAT detects the gamma rays through pair production, where the gamma ray converts to an electron/positron pair, maintaining the ability to reconstruct the gamma-ray's energy as well as its arrival direction.

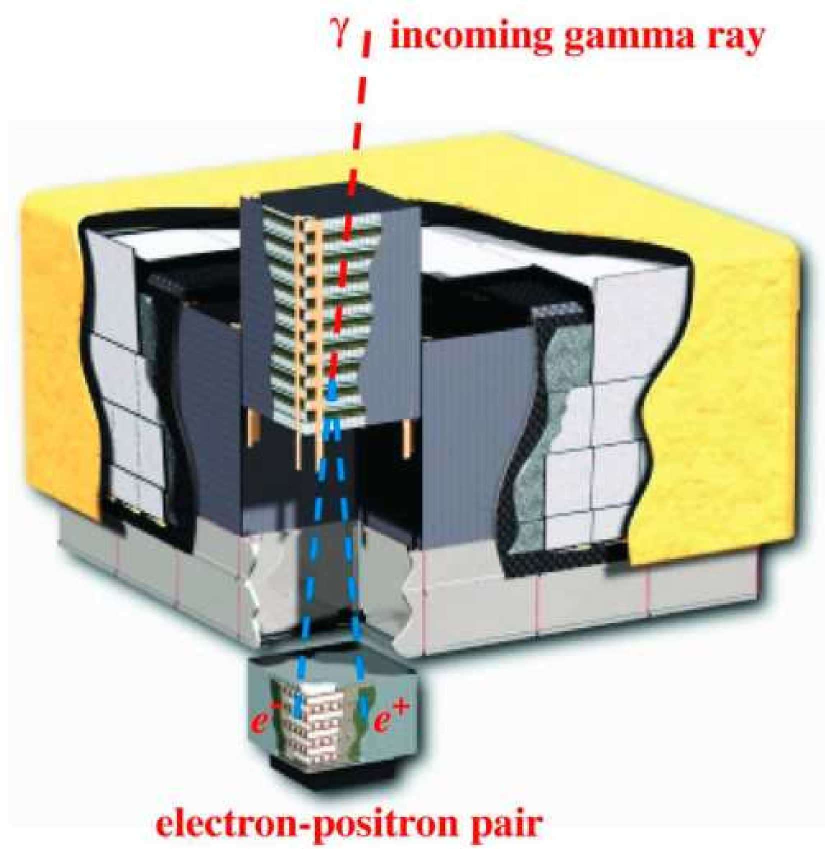

Figure 4–9: The Fermi-LAT Space Telescope showing a gamma ray coming through the conversion foils, forming an electron-positron pair, then going through the silicon strip detectors, to track the particles, and finally stopped in the cesium iodide calorimeter, to measure the final energy. Figure from [15].

One of the methods used to look for PBHs with Fermi was to look for short bursts. In the analysis, the sky was divided into 12288 pixels (any higher would have had pixels smaller than the detector's resolution, 3.5° for 100 MeV photons), and for each pixel, the time separation between each event was computed, and a distribution was drawn. The distribution for each pixel should follow:

$$D(t) = n_o e^{-t/t_0} \tag{4.35}$$

if the background photon events are Poisson-distributed. Here, $D(t)$ denotes the distribution function, n_o is a constant, t is the time and t_0 is the mean time between events. If a burst were to be found, one would then expect the time-difference distribution to be significantly different from that distribution (with an emphasis on the lower time-difference values when looking for bursts from PBH explosions). The Fermi group used a log-likelihood method to find pixels that deviated from the expected background distribution.

Most pixels that presented a significantly different distribution were clustered around the Galactic plane or were at the location of known sources; they were ignored. In the end, no interesting bursts were found with this search. This results in a 99%-confidence level rate-density upper limit of 7.8×10^{-8} pc^{-3}yr^{-1}. This limit is much better than any done by Cherenkov telescope experiments, however, the model used in this analysis assumed that the total emission from the PBH increases exponentially following the Hagedorn model. This would bring the limit down by orders of magnitude compared to the now-standard model, and the results from IACT experiments.

4.4.3 EGRET

Another search method is to calculate the amount of emission from PBHs in the Galactic gamma-ray background. EGRET did such a search [78]. EGRET was one of four instruments on NASA's Compton Gamma Ray Observatory (CGRO). It also used pair production to detect gamma rays, from 30 MeV to 30 GeV. Its angular resolution was worse than Fermi's (5.5° at 100 MeV as opposed to Fermi's 3°). EGRET used a different technology, a spark chamber for the direction measurement, as well as an NaI calorimeter to measure the energy.

The EGRET search focused on the emisson from PBHs which would be broadly distributed like the dark matter in our Galaxy, assuming that some, if not all, of the dark matter would be made of PBHs. They looked for emission from black holes of temperature of 20 MeV, with peak gamma-ray energies of 100 MeV, and with about 20 years left before full evaporation. They tested for diffuse emission from PBHs which would be dispersed in the Galaxy based on dark matter density profiles.

The analysis was done by taking all the data from the whole sky and testing two models, one with all known sources of emission as well as dark matter without PBH emission, and one including PBH emission following dark matter distribution, and tested if the two models were statistically different. No evidence of PBH evaporation was claimed to have been found.

With this result, they were able to draw limits for the different dark matter profiles, on the fraction of dark matter that is composed of PBHs, their cosmological density and the fraction of regions of the early universe that underwent collapse and formed them.

4.4.4 Whipple 10-meter

The Whipple 10-meter telescope Collaboration looked for PBHs under the assumption of the standard model of PBH evaporation discussed in the previous section. The analysis technique they developed is very similar to what is used in this work, and will be explained in Chapter 6.

The 10-meter Whipple telescope was built in 1968 and was the first major instrument purpose-built as an atmospheric Cherenkov telescope for gamma-ray astronomy[79]. The VERITAS telescopes follow a similar design and their functioning will be expanded upon in Chapter 5. The telescope had a 10-meter diameter reflector that reflected the Cherenkov light to its central camera placed at the focus.

The camera comprised an array of phototubes, the number of which has varied over the years.

In total, the Whipple Collaboration looked at 2191 hours of data to get their result. They looked for bursts of gamma rays, falling into a time window (1, 3 or 5 seconds), and within 0.13° of each other, a number motivated by the gamma-ray angular resolution of the telescope. They compared the number of bursts in the data with an estimated background, which they got by scrambling the arrival time of the gamma rays in the data, but keeping the arrival direction the same. In this way, they could get a random distribution of bursts while simultaneously taking into account the effects of the varying sensitivities across the camera. Figure 4–10 compares the number of bursts they found in the data with the estimated background.

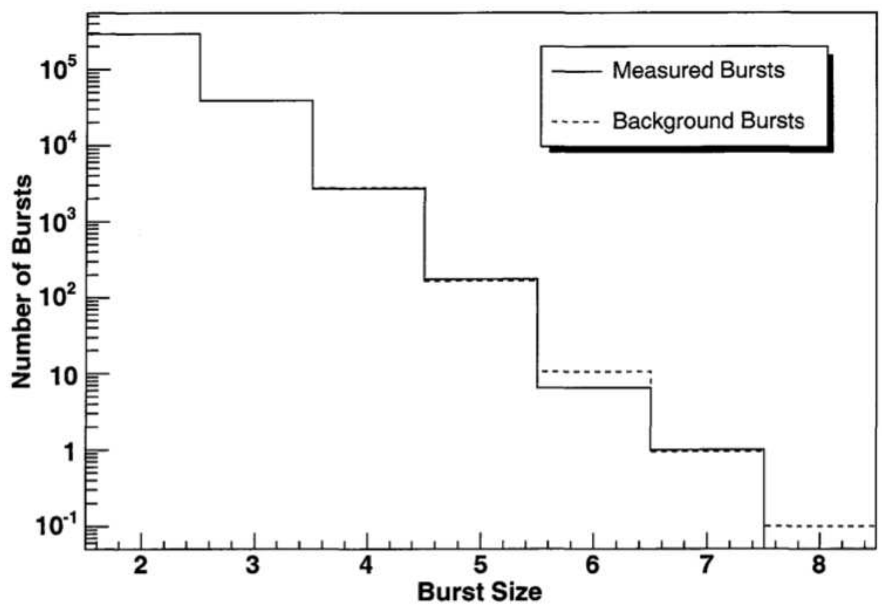

Figure 4–10: Number of bursts versus burst size (number of gamma rays in the burst) for the measured and background data. These data are from the third camera configuration of the Whipple telescope, from the fall of 2000 to spring of 2003, with only data from a zenith angle of less than 20° and using a time window of 5 seconds. Figure from [80].

No burst signal was found, and they were able to compute an upper limit on the rate-density of primordial black hole evaporation for the three different time windows, as shown in Figure 4–13. The three grey stars at 1, 3 and 5 seconds, corresponding to limits of 1.72×10^6, 1.59×10^6 and 1.08×10^6 pc^{-3} yr^{-1}, respectively, at a 99% CL.

4.4.5 SGARFACE

SGARFACE (for Short GAmma-Ray Front Air-Cherenkov Experiment) used the Whipple 10-m telescope to search for gamma-ray bursts in durations of a few ns to $\sim$20 μs, with gamma-ray energies above 100 MeV [81].

With the standard model of PBH evaporation, the final evaporation would burst in the last few seconds, with most of the energy emitted above 400 GeV; only 22% of the total energy would be emitted in gamma rays, with the spectrum peaking at 100 MeV and falling off as described in Equation 4.31.

In contrast, the Hagedorn model, discussed in Section 4.2.2, predicts a final burst lasting around 100 ns, with 10-30% of the black hole's mass resulting in photons with energies between 100 MeV and 1 GeV. SGARFACE then was particularly able to test the Hagedorn model of PBH evaporation.

To do this search, they implemented a system that was parasitic to the standard data acquisition of the Whipple 10-m telescope, by splitting the signal coming from the PMTs. One part went to the standard back-end, while the other went to the SGARFACE system.

The idea was to catch the Cherenkov showers from low-energy gamma rays. In the hundreds of MeV range, the Cherenkov light from one gamma ray is not detectable by typical Cherenkov telescopes, but the Cherenkov light from a multitude (or a wavefront) of near-simultaneous sub-GeV gamma rays will produce a detectable signal.

SGARFACE had a purpose-built trigger. Its first level was a multi-timescale discriminator, i.e. it looked for a threshold over 6 different timescales : 60, 180, 540, 1620, 4860 and 14580 ns.

The next level of trigger was a pattern-sensitive coincidence unit, designed to check if a sufficient number (in this case, seven, optimized to reduce accidental triggers from night-sky background fluctuations, while still being sensitive to the searched-for signal) of nearest-neighbor channels have been triggered by the multi-timescale discriminator. If that trigger was satisfied, the data were recorded.

No other events than background were found, so no detection of PBH evaporation were claimed. This resulted in a 99% confidence level upper limit shown in Figure 4–11.

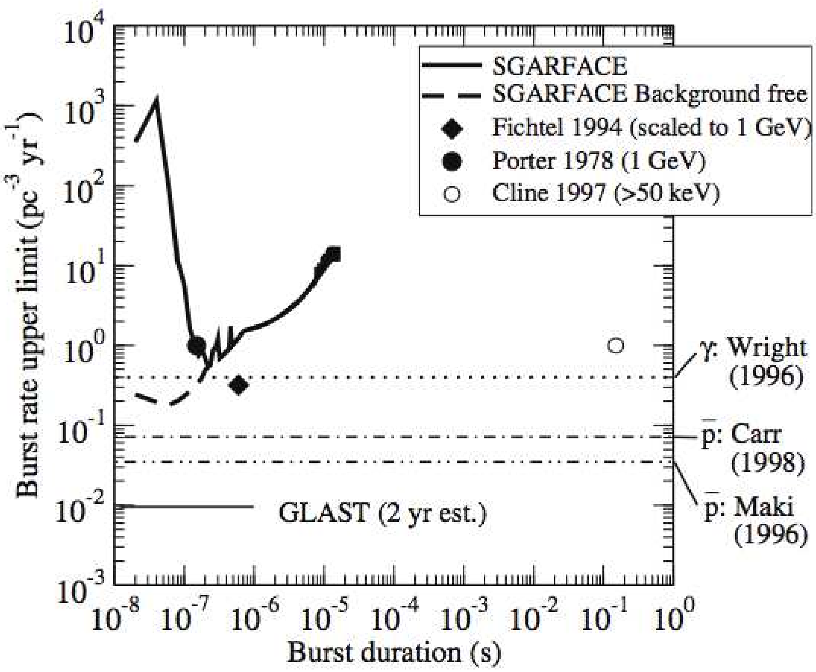

Figure 4–11: 99% upper limits on the rate-density of PBH explosions from SGARFACE. Due to the presence of background, the thick line represents the limits, and the thick dashed lines are what they would have reached if background-free. The thin full line is the estimate of the expected limits after 2 years of observations with GLAST (now known as the Fermi Gamma-Ray Space Telescope), which was launched after the SGARFACE results were published. Also visible on the plots are results from EGRET (Fichtel, 1994) [82], from Cherenkov experiments (Porter, 1978) [83] and from gamma-ray bursts observations (Cline, 1997)[84]. The dash-dotted and dash-double-dotted lines give limits from cosmic ray measurements [85, 86] while the dotted line comes from measurements of anisotropies in the galactic halo emissions [87]. Figure from [81]

4.4.6 VERITAS

VERITAS also did a search for PBHs prior to this work [88]. The analysis was very similar to the one done by the Whipple 10-m from Section 4.4.4, with the difference that this time, it was done using an array of 4 12-meter telescopes. The angular resolution of VERITAS being 0.1° (the 68% containment radius at 1 TeV), this was the new maximum separation between events used in this analysis. The time window was fixed at 1 second. The data used was from January 2008 to December 2009, for a total of 700 hours. A maximum-likelihood method was used to determine the upper limit, and Figure 4–12 shows its behavior for the different zenith angle bins, as well as for all of the data runs combined. The 99% confidence level upper limits on the rate-density of PBH evaporation with the maximum-likelihood method is found when $\Delta(-2\ln L)$ is 6.63, which here is 1.29×10^5 pc^{-3}yr^{-1}. This is the result reported by VERITAS, which is also shown in Figure 4–13 as the blue square. Scaling the limit for the total available data at the time ($\sim$ 2200h), the result would have been 6×10^4 pc^{-3}yr^{-1}.

4.4.7 HESS

The H.E.S.S. (the High Energy Stereoscopic System) experiment [89], an array of 4 12-m Cherenkov telescopes based in Namibia, also looked for PBHs. Their cameras each have a field of view of 5°, comprising of 960 PMTs. A search for PBHs was done in 2009 [65]. The search method was essentially the same as was used by VERITAS. They used 2794 hours of data, and quoted results for the 1 second time window. The resulting limit is 7.1×10^4 pc^{-3}yr^{-1} at the 99% CL.

More recently, however, H.E.S.S. released new limits, with a variation on the analysis [90]. They used 2600 hours of data, and did the analysis with different time windows (1, 5, 10, 30, 45, 60 and 120 seconds). This allowed them to test at which time window they were the most sensitive. With a narrower time window, less signal can be seen in the data, whereas with a wider time window, the data are dominated by background. Looking at different time windows allows one to

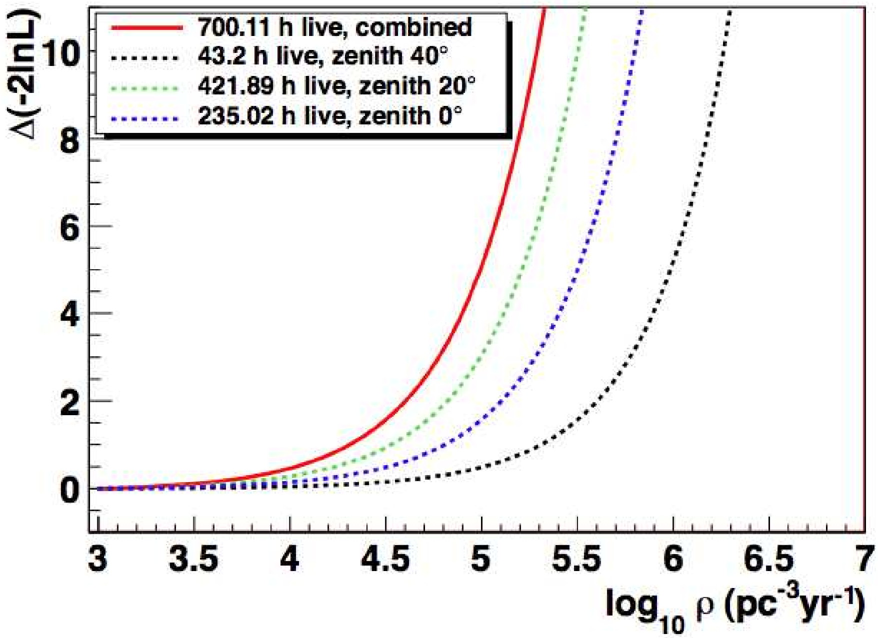

Figure 4–12: Maximum-Likelihood method to compute the 99% confidence level upper limit with VERITAS. The curves shown here correspond to the different zenith angle bins of the data, as well as with all the data runs combined. The upper limits are found when $\Delta(-2\ln L)$ is 6.63. Figure from [88].

optimize the balance between the two. H.E.S.S. found a broad minimum in the sensitivity limit at a time window of 30 seconds.

When doing gamma-hadron separation in the analysis, instead of using a set of fixed cuts (so-called"box cuts", see Section 6.5.1), they used what they called the 'model' technique, Model++ [91]. This technique consists of comparing the raw Cherenkov camera images with predictions from a semi-analytical model, using a log-likelihood minimisation. This method allows one to get a more precise direction and energy reconstruction of the photon-induced shower compared to the box cuts, as well as a better gamma efficiency and improved background rejection. All together, this gives them a factor of ∼2 better sensitivity compared to the standard reconstruction techniques.

Using that, they got upper limits at the 95% confidence level of 4.9×10^4 $\mathrm{pc}^{-3}\mathrm{yr}^{-1}$ for the 1-second time window, and 1.4×10^4 $\mathrm{pc}^{-3}\mathrm{yr}^{-1}$ for the 30-second time window. These results are shown in Figure 4–13 (the green diamonds), where the rate-density was rescaled to a 99% confidence level in [70] to better compare with other experiments.

4.4.8 Milagro

Milagro was an air shower detection experiment, sensitive to gamma rays of 10 to 100 TeV. It was located near Los Alamos, New Mexico at an altitude of 2630 m, and was used from 2000 to 2008. It consisted of a large covered reservoir of water (60 by 80 by 8 meters) with two layers of PMTs designed to detect the Cherenkov light from the charged particles from the particle shower interacting in the water. 175 smaller outrigger tanks were spread around the reservoir, each mounted with a single PMT at the top of the tank, observing downward into the water. The outrigger tanks served to increase the detector's angular resolution and background-rejection capabilities [92].

The Milagro collaboration looked for bursts over a range of time windows, from 250 μs to 6 minutes [70]. They created skymaps for overlapping time intervals, each offset by 10% of the desired burst duration (i.e. for each time window). For each time interval, they searched the skymap for an excess of signal over background, and found no significant excess. They then calculated their upper limits, using the equation:

$$\mu(r, \theta, \tau) \; = \; \frac{1-f}{4\pi r^2} \int_{E1}^{E2} \frac{dN_\tau}{dE} A(E, \theta) dE \tag{4.36}$$

where f is the dead time fraction of the detector, and dN_τ/dE is the black hole gamma-ray spectrum integrated from times τ to 0 from Equation 4.31. E_1 and E_2 represent the lower and upper bounds of the energy range searched, and $A(E, \theta)$ is the effective area of the detector as a function of energy and zenith angle.

The results can be seen in Figure 4–13, with the red circles. Their limits are most sensitive with a time window of 1 second, giving an upper limit of 3.6×10^4 pc^{-3} yr^{-1}.

4.4.9 HAWC

HAWC is a successor to Milagro, located at an altitude of 4100 m, on the Sierra Negra volcano, near Puebla, Mexico. It looks at the resulting particles from a shower using the same method as Milagro. It consists of an array of 300 water Cherenkov detectors, covering an area of 22000 m^3 [93]. This gives HAWC an order of magnitude more in sensitivity over Milagro. It was formally inaugurated on March 20, 2015.

Using simulations to estimate the expected background rate of HAWC, the collaboration was able to estimate its sensitivity to PBH evaporation over certain lifetimes [70], as is shown in Figure 4–13 using the same analysis technique as Milagro's analysis. This resulted in an expected upper limit, at the 99% confidence level, after 5 years of observation, of 4059 $\mathrm{pc}^{-3}\mathrm{yr}^{-1}$ with a 10-second time window, their most sensitive.

4.5 Conclusion

PBHs physical behavior is now understood thanks to the standard model detailed in this chapter. Using this information, different experiments have looked for them, and their results have been summarized. This information will also be used in the work of this thesis, using the VERITAS telescopes. Before getting to that, however, details of the VERITAS experiment need to be explored, which is done in the next chapter.

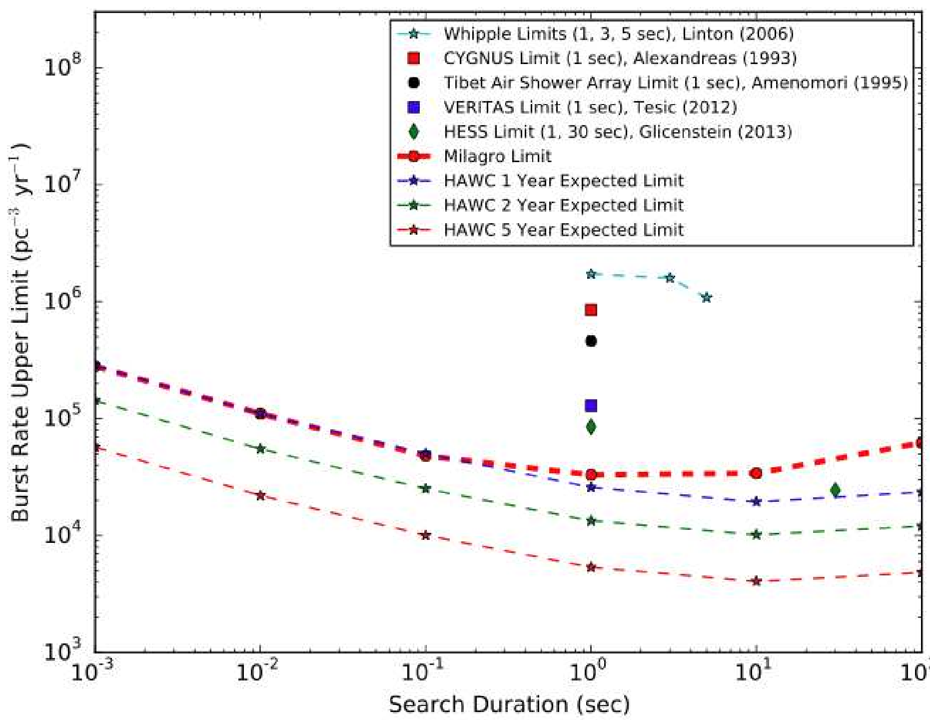

Figure 4–13: 99% CL Upper limits on the rate-density of PBH evaporation of different experiments. Of note are the results from the Whipple 10-meter in 2006 (see Section 4.4.4), the latest VERITAS and HESS limits (Section 4.4.6), the Milagro and expected HAWC limits (Section 4.4.8). Figure from [63].

CHAPTER 5

VERITAS Experiment

The search for Primordial Black Holes (PBHs) done in this thesis uses the VERITAS Telescopes. Hence, this chapter will outline the experimental design of the VERITAS telescopes.

As explained in Chapter 2, Very-High-Energy (VHE) gamma rays generate particle showers that in turn produce Cherenkov light. It is this Cherenkov light that is detected by the telescopes, and used to reconstruct the original gamma ray's properties (more on that in Chapter 6).

The VERITAS array consists of four Cherenkov telescopes, located at the Fred Lawrence Whipple Observatory (FLWO) in southern Arizona, USA (approximately one hour south of Tucson), at an altitude of 1300 m. The first telescope was completed in February 2005, with the full array completed in April 2007. Due to political difficulties with regards to the original VERITAS site, the configuration used was not optimal. Over the summer of 2009, one of the telescopes was moved to provide a more symmetrical array, with improved sensitivity. Figure 5–1 shows the most recent VERITAS array configuration, and Figure 5–2 shows a schematic of the array layout.

5.1 Telescope Design and Optics

The VERITAS telescopes are based on 12 m diameter f-1.0 Davies-Cotton reflectors [94], composed of 345 spherical mirror facets, with radius of curvature of 24 m, installed on a spherical optical support structure (OSS) with radius of curvature of 12 m.

Figure 5–1: Picture of the current VERITAS array. The VERITAS control building can be seen in between the telescopes (with the white roof), next to the administration building of the FLWO, also housing support technicians for the experiment. Image credit: Larry Ciupik.

It is easier and cheaper to manufacture many individual smaller facets than one large one. The facets are all identical to one another, so they can be used in any part of the dish, as opposed to a parabolic reflector, which requires its mirror facets to correspond to the part of the parabolic structure they will be mounted on. On-axis and off-axis aberrations are also much smaller than in the parabolic counterpart. The main disadvantage of the Davies-Cotton design is that the surface is not isochronous, introducing a spread of approximately 4 ns to the incoming Cherenkov front [95]. Each facet is attached to the OSS using a 3-point mount (Figure 5–4), each screw being used to adjust its orientation.

Each mirror facet is made of slumped, polished glass, aluminized and anodised at an on-site optical coating laboratory. This laboratory contains

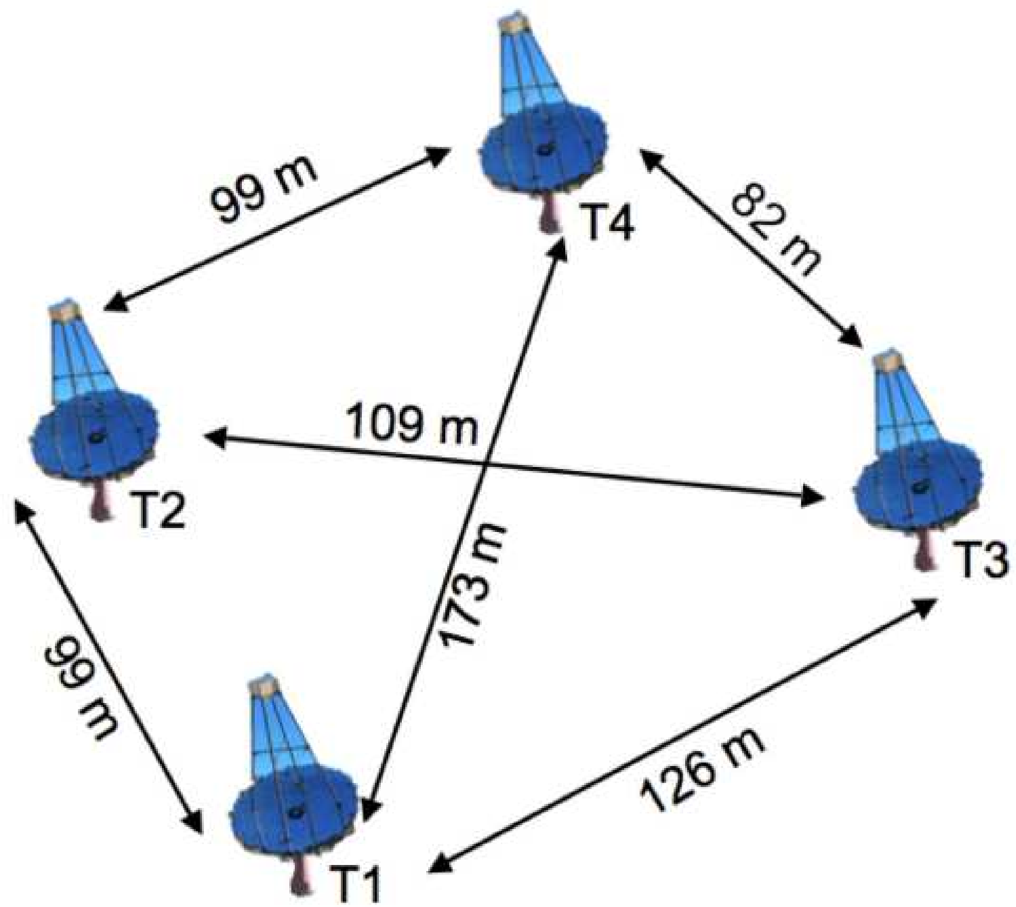

Figure 5–2: Schematic of the current VERITAS array. Image credit: Roxanne Guenette.

120 spare facets that are used to replace groups of mirrors on the telescopes on a rotating basis. The mirrors degrade with time as they are exposed to dust, so they need to be realuminized on a regular basis.

The OSS is mounted on an altitude-azimuth positioner, which can slew at a speed of 1°/s, with pointing accuracy of approximately 50-100 arcseconds. Four quad arms connect the OSS with the camera, and the reflector and camera are balanced by a set of counter weights. An electronics building, where the electronics for the camera readout and monitoring systems are housed, is located next to the positioner. Figure 5–5 shows a detailed picture of a VERITAS telescope.

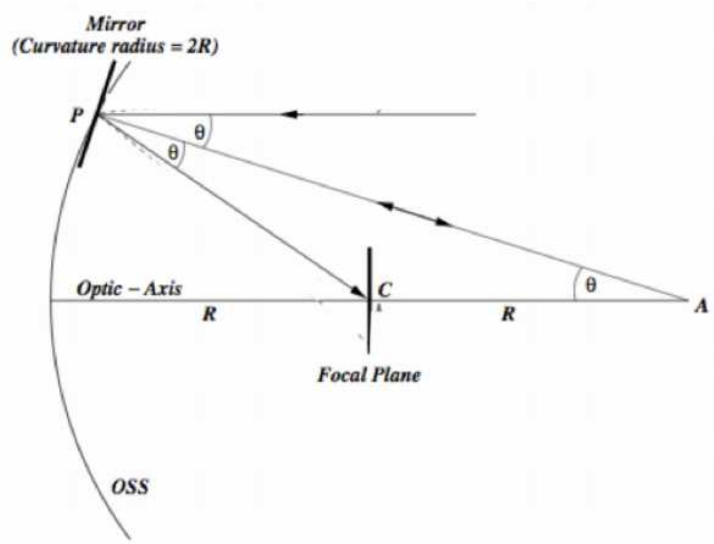

Figure 5–3: Diagram of the Davies-Cotton reflector design. Figure from [79]

5.2 Camera

The VERITAS cameras are located at the focal points of the telescopes (12 m away from the dish). Each camera is pixelated, being composed of a total of 499 photomultiplier tubes (PMTs). Figure 5–6 shows one such camera, with the PMTs installed.

The PMTs were changed in the summer of 2012 as part of a detector upgrade. The first ones were Photonis XP 2970/02, and were replaced with Hammamatsu R.10560-100-20MOD. The Photonis PMTs have a peak quantum efficiency (PQE) of ∼25% at 320 nm, while the new PMTs have PQE of ∼35% at 350 nm. This upgrade was done so that the telescopes will be more sensitive to a lower amount of Cherenkov light, thereby reducing the energy threshold of the experiment. This is useful in the search for pulsed emissions from pulsars, or in the search for lower-mass dark matter particles, or in reaching down to the higher energy range of the Fermi Gamma Ray Space Telescope.

Figure 5–4: A VERITAS mirror mount. Each of the three points of the mount is a combination of a mounting bolt, a fine-alignment screw and a gimbal so that the facet's orientation can be adjusted. Image credit: Andrew McCann

Both models of PMTs are operated at a gain $G = 2 \times 10^5$, at a typical voltage of ~ 850 V, so a photoelectron will generate approximately $2 \times 10^5 \times q_e$ C ≈ 0.03 pC of charge at the anode of the PMT. Preamplifiers are connected to the PMTs to provide an amplification factor of 6.6. This is used to increase the size of the signal before it travels down the 45 m of signal cable from the camera to the electronics building, thus minimizing the effects of ambient electronics noise.

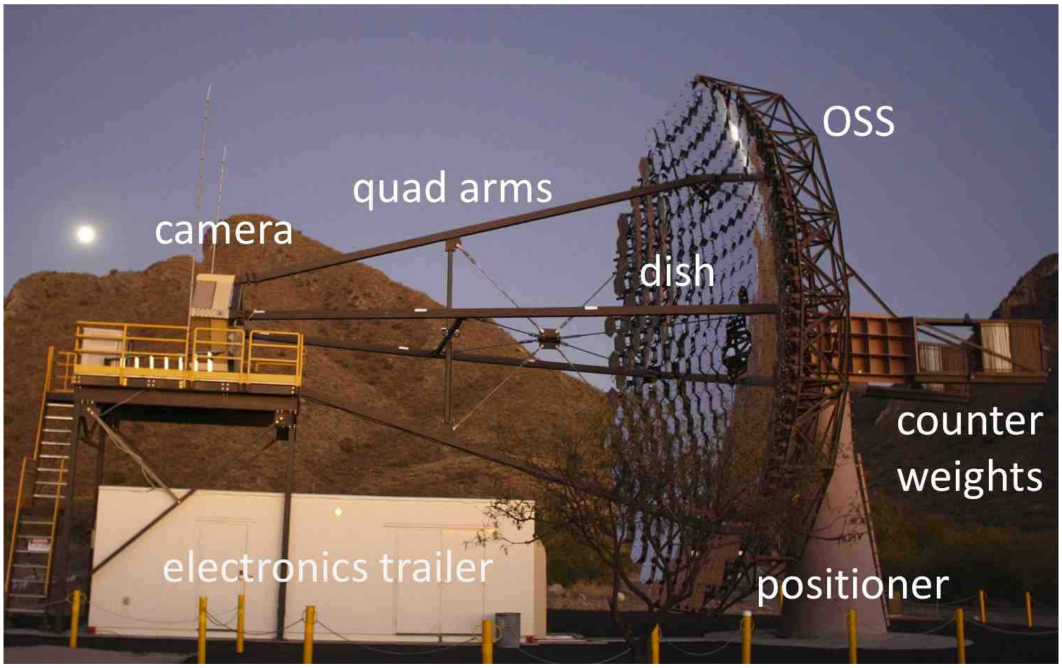

Figure 5–5: View of one of the VERITAS Telescopes, called T1. The different components of the telescopes are named here (see text for a description). Image credit: Sean Griffin

A light cone plate is placed in front of the camera, made of 499 modified Winston cones [96] (see Figure 5–7). It is used to reject stray light not coming from the dish, and to reduce the dead space between the PMTs. The light cone plate increases the light collection by $\sim 65\%$. The VERITAS cones have a hexagonal entry aperture, and eventually morph into the standard cylindrical shape, as opposed to being cylindrically symmetric throughout, like in the case of "true" Winston cones. The front of the light cone plate is located at the focal plane of the telescope.

The distance of adjacent PMTs, from center to center, is 31.4 mm, and the optical plate scale (the relation between the physical distance in the focal plane and angular size on the sky) of the VERITAS telescopes is $0.148°$/PMT, for a field of view diameter of $3.5°$ for the camera.

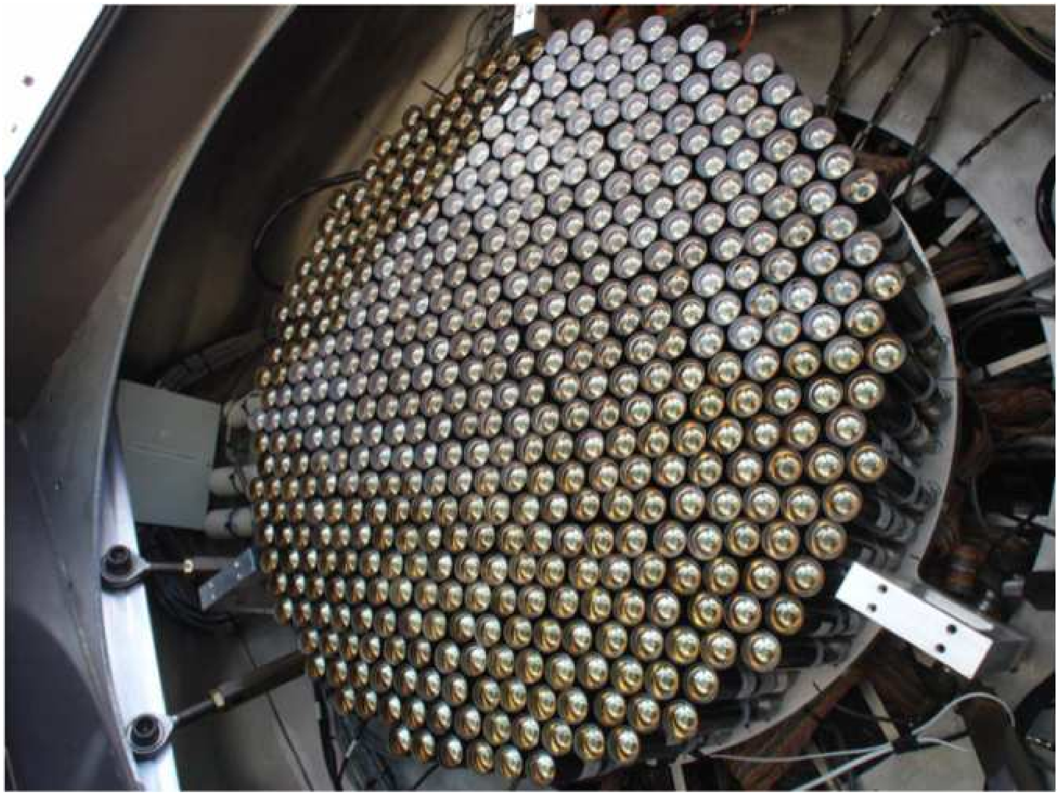

Figure 5–6: A VERITAS camera, with the 499 PMTs installed.
Image credit: Luis Valcarcel

5.3 Data Acquisition

The PMTs receive the Cherenkov emission from a particle shower that needs to be recorded. The resultant electrical signals are sent directly to custom-built 8-bit, 500 MSamples/s flash analog-to-digital converters (FADCs), installed in the electronics building at the base of their respective telescopes. Each FADC continuously digitizes the signal from each PMT and stores the information in a 65 μs buffer. A copy of each signal is sent to the trigger system, to determine if it is likely to be from a particle shower, as opposed to sources of background noise, like starlight, moonlight, terrestrial lights, or other sources of night sky background (NSB). If the signals result in a trigger, they are all recorded as an event. The trigger system is split into three levels, explained in the next subsection.

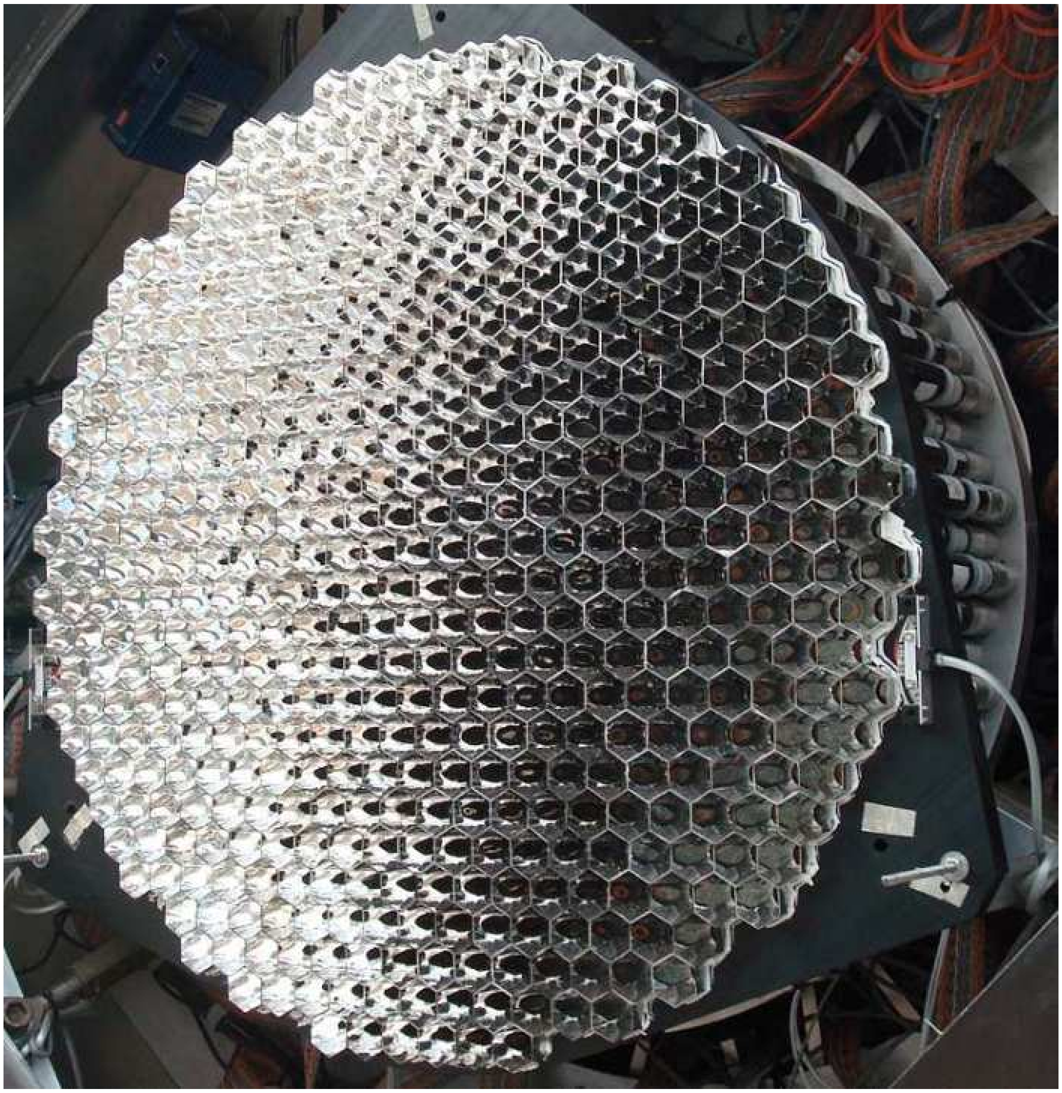

Figure 5–7: A group of light cones installed on top of the PMTs on a VERITAS camera. Image credit: S. Griffin.

5.3.1 Triggers

Pixel: L1 Trigger

This trigger works at the pixel level. In simple terms, it looks at how high the pulse is, and if it reaches a certain threshold (in voltage), will send a signal for the next trigger level (the L2). This is achieved using a charge fraction discriminator (CFD).

The CFD fires if the pulse goes over a threshold, and sends out a pulse with timing information independent of the pulse size. This ensures that the timing information matches for all pulses, useful for the tight coincidences involved. The CFD output pulses are used at the next trigger level.

Telescope: L2 Trigger

The L2 trigger is at the telescope level, and looks for a pattern in the L1 triggers. Since a particle shower's Cherenkov light is expected to hit multiple neighboring PMTs, it looks for a coincidence of L1 triggers between three neighboring pixels within a 5 ns window. This ensures the minimization of the amount of triggers from random fluctuations in the NSB, which would appear on random pixels anywhere in the camera. This is done using field programmable gate array (FPGA) technology [97], with the main advantage of having the ability to program the length of the coincidence window, installed on VERITAS in 2010. Before that system, the pattern trigger was based on hard-wired combinations. This system worked appropriately enough for the purposes of the experiment, but was not programmable, and had a fixed coincidence window of 8 ns.

Array: L3 Trigger

The L3 trigger is at the array level, and looks for a coincidence of L2 triggers from a minimum of two telescopes, within 50 ns of each other. Cherenkov light generated by muons, from hadronic showers, passing close to a telescope will often produce a very similar pattern to gamma-ray-induced showers, with the difference that the muons will only be seen by one telescope at a time. These events are mostly filtered out by requiring a minimum of two telescopes to see a shower image at the same time.

The L2 triggers need to be delayed based on the amount of cable length the signal has to be sent through as well as on the different arrival times of the Cherenkov light at each telescope. The first delay is fixed and easily calculated, while the second one depends on the telescope's pointing direction and is provided by programmable delay modules. More details on the L3 system can be found in [98].

5.3.2 Readout

Once the L3 trigger is satisfied, the event's information is saved. The L3 computer (located in the VERITAS control building) tells the telescope computers to store the events on disk. Each telescope uses an Event Builder software to save the data that produced the trigger, i.e. the FADC traces of each pixel, as well as the timing information. Then, the individual telescopes' data products are sent to the Harvester computer, that combines it into a final data product. The product is then compressed into a custom file format, the compressed VERITAS bank format (cvbf) file. This file is sent to the data archive and is made available for download and use by collaborators for analysis purposes.

5.4 Telescope Calibration

Calibration measurements are necessary to maintain the telescopes' performance. The main calibration runs regularly carried out by VERITAS use LED flashers, to measure the relative gain, absolute gain and relative timing of each PMT.

The flashers are systems of Light-Emitting-Diodes (LEDs) attached to the telescopes' quad arms, 6 m away from the camera, facing the PMTs [99]. Seven UV LEDs are installed inside a flasher unit, peaking at a wavelength of 375 nm. They flash in an eight-step cycle, the first using no LEDs, then one LED, two, three, and so on. A 50 mm opal diffuser is placed in front, to diffuse the light from the LEDs so that it shines uniformly on the PMTs. A picture of a flasher and its LEDs is shown on Figure 5–8.

Figure 5–8: *Left:* An LED flasher. Each telescope has one such device installed. *Right:* The seven LEDs inside the flasher. The diffuser normally sits in front of the LEDs, but is removed here. Image from [99].

The flashers are used for measuring the gains of the PMTs. To measure the absolute gain on a monthly basis, the PMT camera is covered with a neutral density filter that will let in a tiny fraction of photons from the flashers. The absolute gain is then determined by measuring the peak of the resulting single photoelectron (spe) distribution.

PMT gains are also measured nightly by dedicated "flasher runs". The eight different LED light levels sent by the flashers each produce different distributions, each with its own average μ and spread σ. Relating the average of each distribution with their spread, one can find the gain G:

$$\sigma^2 = \sigma_0^2 + G\mu \tag{5.1}$$

where σ_0 is the light-independent noise (e.g. from electronics) and G is the gain of the PMT. This assumes that all fluctuations in the anode pulse are due to photostatistics at the first dynode, so that:

$$\mu = GN_{pe} \tag{5.2}$$

and

$$\sigma = G\sqrt{N_{pe}} \tag{5.3}$$

where N_{pe} is the average number of photoelectrons at a given light level.

5.5 Conclusion

The VERITAS array has been completed since 2007, and has been working successfully since then. It underwent two major upgrades, making the array reach higher sensitivities. The hardware of the experiment has been described, outlining the way it detects the gamma rays. Next is a description of the analysis step, to make sense of the large amount of data being produced by VERITAS.

CHAPTER 6
Analysis Technique

The VERITAS experiment has been described in the previous chapter. In this chapter, the focus will be on the analysis chain of VERITAS data, following these steps:

1. Calibrate the data from the PMTs, taking into account their gains and pedestal values.
2. Clean the images, keeping only the pixels that are relevant for the purposes of finding gamma rays.
3. Parameterize the shower images, which are then used to reconstruct the point of origin of the particle that induced the shower, as well as its energy.
4. Use these reconstructed parameters to discriminate between the gamma-ray and cosmic-ray showers.

Traditionally, a simple method called "box cuts" has been used by VERITAS to do step four, but the analysis described in this work applies a method developed recently by members of the collaboration: boosted decision trees. The differences between the two methods, as well as their performances, will be shown here. One last step, required in the standard VERITAS analysis but not done in the case of the Primordial Black Hole (PBH) analysis, is to compare the event-rate in a given potential signal region with a number of selected background regions, to look for a possible excess in the signal region. A null hypothesis test can be performed to determine the significance of that excess. An equivalent analysis is used in the case of PBHs, which will be explained further in Chapter 8.

6.1 Data Calibration

The data recorded by VERITAS consist mostly of FADC traces, digitized traces of the photomultiplier tubes' (PMTs) pulses, as well as the timestamps of the events and L2 trigger information (see Section 5.3.1 for an explanation of the triggers).

The integrated traces are a measure of the Cherenkov light received by the PMTs.

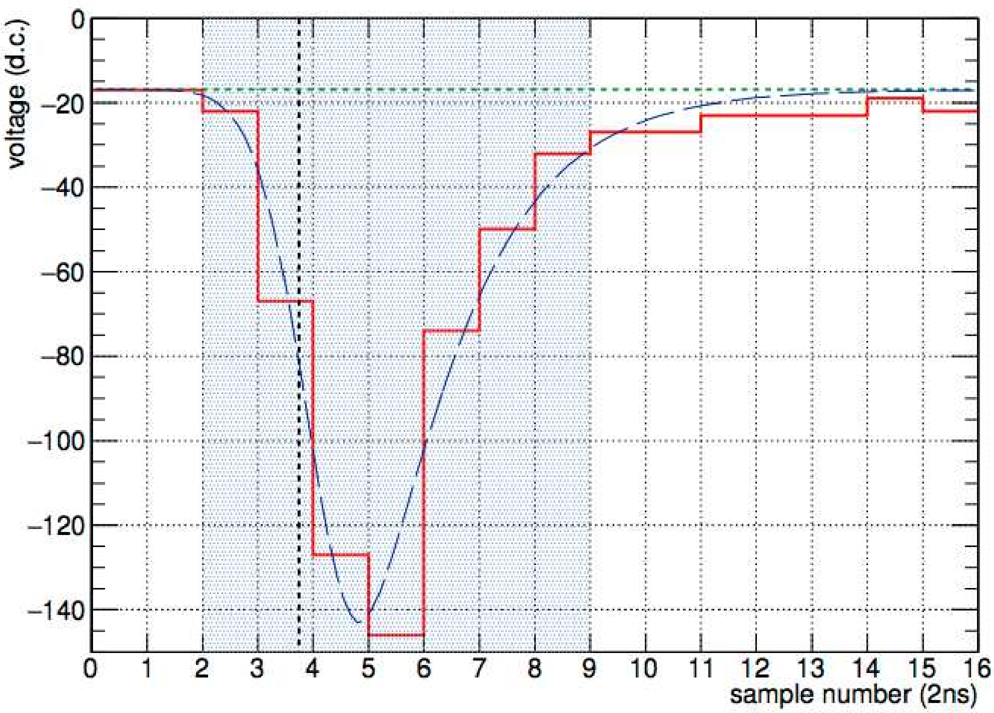

Figure 6–1: Example of a PMT trace. The traces are 16 samples in length (2 ns per sample), with the dashed vertical line indicating the T_{zero}. The shaded region is the integration window used, The dashed horizontal line indicates the pedestal value, and the dashed curve is the fit of the trace. See text for more details. Image Credit : Sean Griffin.

Pedestal events are recorded every second by the telescopes. These events provide a baseline for the traces when no Cherenkov light is measured. In the analysis, for each channel, the pedestal events are grouped in 3-minute time slices. The average traces of each event in the time slices are used to find the pedestal value, as well as its standard deviation, which gives a measure of the amount of background light in the sky. Since the amount of background light from the NSB can vary with time and the pointing direction during a data-taking run, this technique is used for every three-minute time slice. Each trace in the run will then be pedestal-subtracted, using the pedestal determined from the 3-minute time slice the event is in.

The next step of the data reconstruction process is to look at the event traces themselves. For this, a double-pass method is used. The first pass consists of summing the pedestal-subtracted trace, to get the charge for each pixel for each event, over a wide summation window (16 samples), as well as calculating the T_{zero} point of the event, where the trace reaches half of its maximum value. This gives a measurement of the beginning of the signal, and is useful for getting the time gradient across the camera; the arrival time of the Cherenkov pulse will vary systematically from one pixel to another due to geometric effects. The second pass uses a smaller summation window of seven samples, placed using the calculated T_{zero} so as to capture the rising pulse, and maximize the signal-to-noise ratio by removing contamination from background samples outside the main pulse region. Figure 6–1 shows a PMT trace, with the pedestal, and the integration window as described here.

Nightly flasher runs (see Section 5.4) are taken to measure the relative gain of each PMT, as well as its timing parameters. Since the light sent by the flasher is identical for each PMT, the relative responses that are measured are used to adjust the data traces, ensuring equal response of the PMTs to the light source. Due to differences in cable length and electronic delays, it is important to correct any timing differences, so that all channels have the same relative timing.

6.2 Image Cleaning

Once all the information in each pixel has been processed, one needs to determine which of them have relevant information about the Cherenkov emission from a particle shower. An individual pixel-of-interest is identified by the signal-to-noise ratio (S/N) of that channel:

$$(S/N)_k = \frac{Q_k}{\sigma_k} \tag{6.1}$$

where Q_k is the charge of that channel and σ_k is the RMS of the pedestal for that channel at that time. A pixel is considered interesting when (S/N) is greater than 5; it then becomes an "image" pixel. If a pixel next to an image pixel has (S/N) greater than 2.5, it is considered a "border" pixel. This ensures that the strict criteria for the image pixels does not remove relevant information from weaker signals in the camera.

6.3 Hillas Parametrisation

The comparison of the propagation of gamma-ray and cosmic-ray showers was shown in Figure 2–2. The resulting image on the camera will also be different between the two; the gamma-ray image will be elliptical, whereas the cosmic-ray one will be broader and less uniform (see Figure 6–2).

By parameterizing these images, it becomes possible to discriminate between the two. In 1985, A.M. Hillas used Monte Carlo simulations of such electromagnetic showers and developed quantities derived from image properties to parametrize them based on elliptical parameters [100]. These are

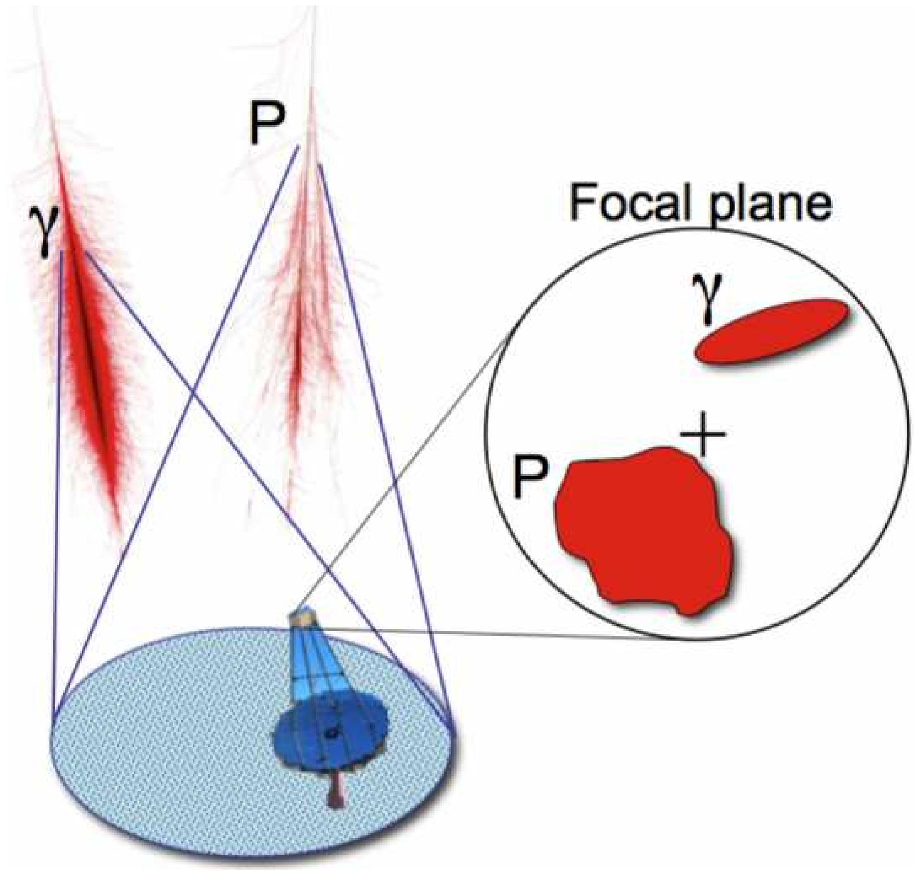

Figure 6–2: Difference in appearances between a gamma-ray and a cosmic-ray-induced (from a proton) shower in the camera. The gamma-ray one is elliptical whereas the cosmic-ray one is more chaotic. Image credit: Roxanne Guenette

historically known as Hillas parameters (see Figure 6–3), and are defined as follows:

- WIDTH: The RMS spread of light along the image's semi-minor axis, to measure the shape of the image
- LENGTH: The RMS spread of light along the image's semi-major axis, to measure the shape of the image
- DISTANCE: The distance between the image centroid and the center of the field-of-view, to measure the impact parameter of the particle shower

- AZWIDTH: The RMS spread of light along a line perpendicular to the line connecting the image centroid to the center of the field-of-view, to measure the shape and orientation of the image
- MISS: The perpendicular distance between the major axis of the image and the center of the field-of-view, to measure the orientation of the image
- FRAC2: The fraction of the total charge contained in the 2 brightest PMTs, to measure the concentration of the image brightness

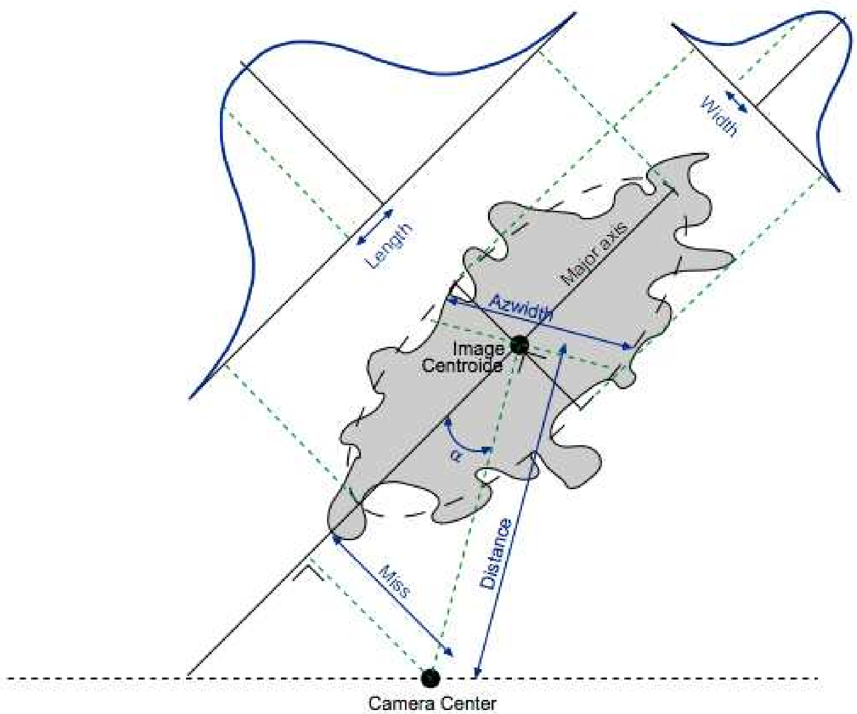

Figure 6–3: Schematic of the Hillas Parameters derived from the image analysis. Image credit: Andrew McCann.

These quantities are all calculated from the moment analysis of the images. Over the years, new parameters were found to be useful and were added to the standard analyses of IACT data:

- SIZE: The integrated charge of all the relevant pixels surviving after the image cleaning step, to measure the brightness of the image
- LOSS: The fraction of the size that is contained in the outermost pixels in the camera, to measure the image containment
- ALPHA: The angle between the major axis of the image and a line joining the centroid of the image and the center of the field-of-view, to measure the orientation of the image

6.4 Event Reconstruction

Using these calculated parameters, the incident gamma ray's properties can now be determined. The desired properties are:

- The arrival direction of the gamma ray, to determine its emission source
- The energy of the gamma ray
- The core location, where the gamma ray would have hit the ground had it not been absorbed by the atmosphere

6.4.1 Arrival Direction Reconstruction

To reconstruct the direction of the gamma ray, the images from all telescopes are overlaid and the ellipses' major axes are drawn (see Figure 6–4). The weighted average of the intersection points between the major axes will give the arrival direction of the photon.

The weight W_{ij}, of a pair of telescopes i and j, is calculated so as to minimize the perpendicular distances between each major axis. The weight is calculated here:

$$W_{ij} = \left(\frac{1}{s_i} + \frac{1}{s_j}\right)^{-1} \times \left(\frac{w_i}{l_i} + \frac{w_j}{l_j}\right)^{-1} \times \sin\theta_{ij} \tag{6.2}$$

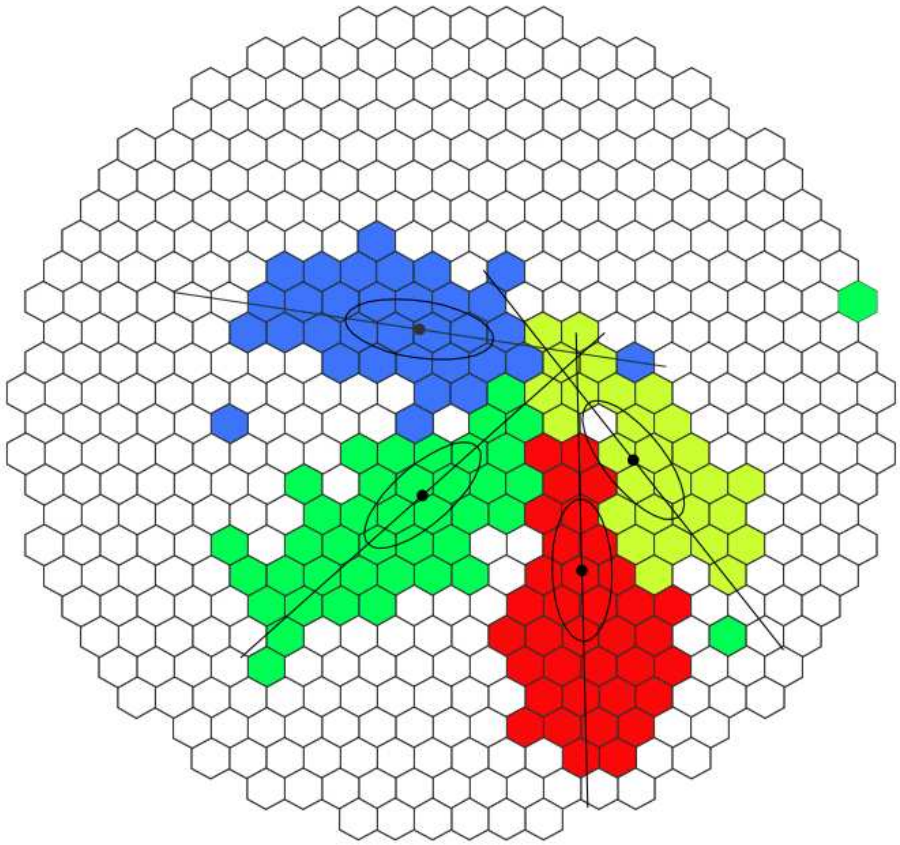

Figure 6–4: Schematic of the incident gamma ray's arrival direction reconstruction. The four camera images are overlaid, and the intersection between the four major axes gives the arrival direction. Image credit: Andrew McCann.

where i and j are two telescopes of a pair, θ_{ij} is the angle between the images' major axes, w_i and w_j are the width of the respective ellipses, l_i and l_j are their lengths, and s_i and s_j are the image sizes, as defined in the previous section. This means that if the size of one or both of the images are low, the weight will be lower, giving that pair of telescopes less importance in the direction reconstruction. The same idea is at work for the ratio of width and length, where a large ratio indicates an elongated ellipse, for which the direction reconstruction will be more accurate.

Once the position is found in the camera, it is then a matter of converting the coordinates to standard astronomical coordinates (in general using equatorial coordinates J2000, consisting of right ascension (RA) and declination (DEC)). J2000 refers to the epoch used as the reference point for the coordinates, as they vary in time.

6.4.2 Shower Core Reconstruction

Another useful property to reconstruct is the position of the shower core, i.e. where the gamma ray would have hit the ground had it not been absorbed by the atmosphere. It will be used to help in determining the location of the shower relative to the telescopes. The method to find it is similar to the arrival direction reconstruction, only the analysis is done in spatial coordinates as opposed to angular coordinates in the camera plane. The telescope images are placed at the physical location of the telescopes, the image major axes are drawn, and the weighted intersection point is used as the reconstructed shower core. This can be seen in Figure 6–5. The core position reconstruction can be used to derive the *impact parameter* r, the distance between a telescope and the shower core in a plane perpendicular to the shower arrival direction.

This will be useful for the next calculated parameter: the height of the shower maximum.

6.4.3 Height of the Shower Maximum

The shower maximum is the point where the most particles are produced in the shower, above threshold for the medium to emit Cherenkov light, making it the brightest part. The height of the shower maximum H_i for a telescope i is given by this equation:

$$H_i = \frac{r_i}{\tan \theta_i} \tag{6.3}$$

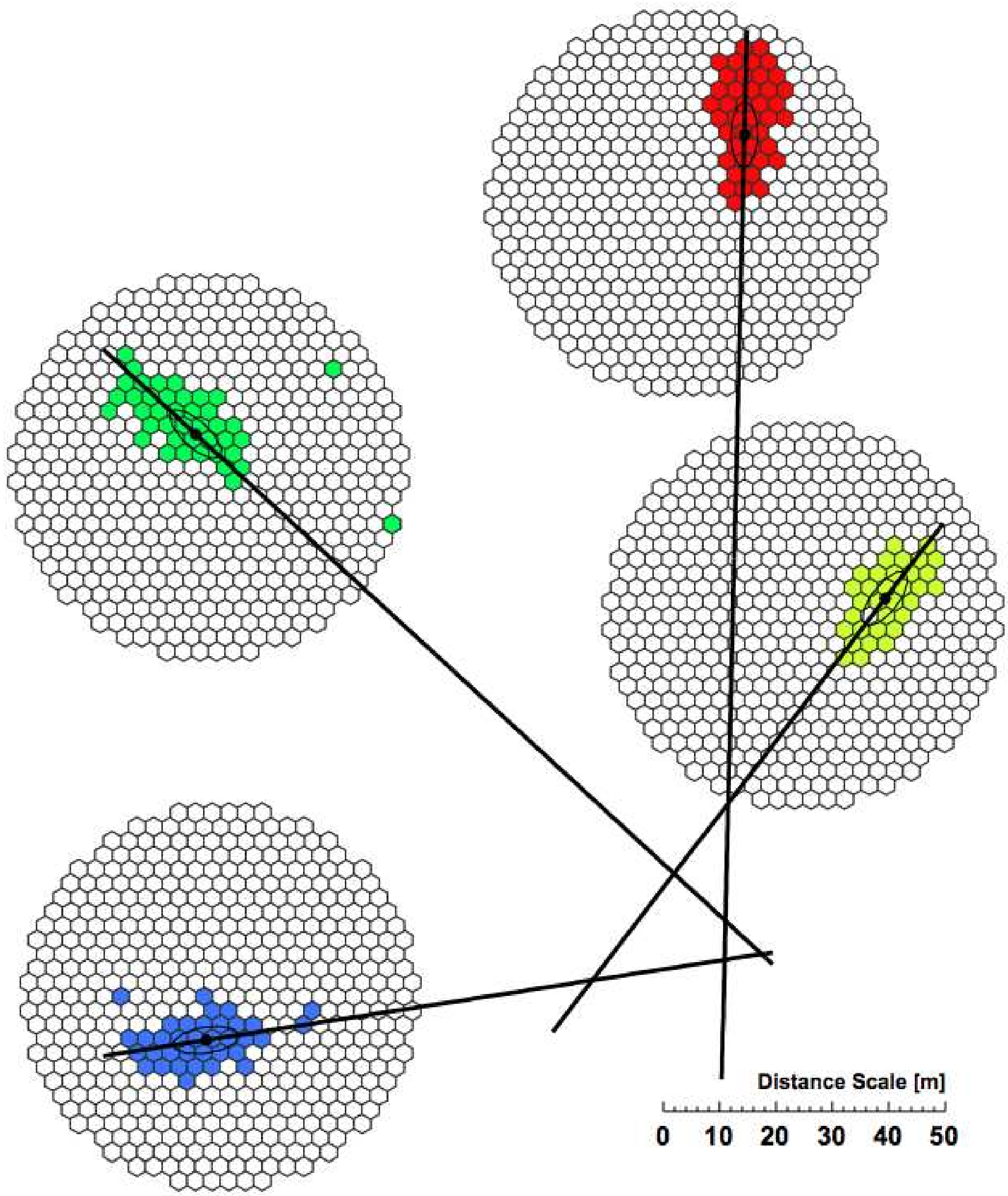

Figure 6–5: Schematic of the incident gamma ray's shower core reconstruction. The four camera images are placed at the ground location of the telescopes, and each image's major axis is drawn and the weighted intersection point will be the shower core position, where the primary gamma ray would have hit the ground. Image credit: Andrew McCann.

where r_i is the impact parameter calculated in the previous section, and θ_i is the angle between the image centroid and the reconstructed arrival direction for telescope i. This relation can be derived geometrically, from the schematic in Figure 6–6.

As cosmic ray showers and single muons penetrate deeper into the atmosphere than gamma ray showers, the reconstructed height of shower maximum becomes a useful tool for background discrimination.

6.4.4 Energy Reconstruction

The last parameter that is reconstructed is the energy of the incident gamma ray. A higher-energy gamma ray will result in more Cherenkov light, which will then be detected by the PMTs. Hence, the image brightness is a good proxy for the gamma ray's energy. However, the amount of Cherenkov light collected also depends on the distance to the shower core and on the arrival angle of the shower. The effects of these parameters need to be understood so that one can reconstruct a reliable energy estimate. To do this, the use of Monte Carlo simulations to simulate gamma-ray showers is necessary, so that the influence on the different parameters can be directly tested.

The simulations consist of generating millions of gamma-ray-induced showers, and calculating the resulting parameters. These parameters are then compiled into multidimensional reference tables (called look-up tables), categorized by pointing direction, shower size, and other useful information. When reconstructing the energy of an actual gamma ray, these parameters are used as "coordinates" in the table to find the corresponding energy. The reconstructed energy is weighted as follows:

$$E = \frac{\sum_{i=1}^{N_{Tel}} E_i/\sigma_i^2}{\sum_{i=1}^{N_{Tel}} 1/\sigma_i^2} \tag{6.4}$$

where E_i is the energy estimate of the specific telescope, and σ_i is the standard deviation of the energy distribution, also found from a reference table. Figure 6–7 shows examples of such tables.

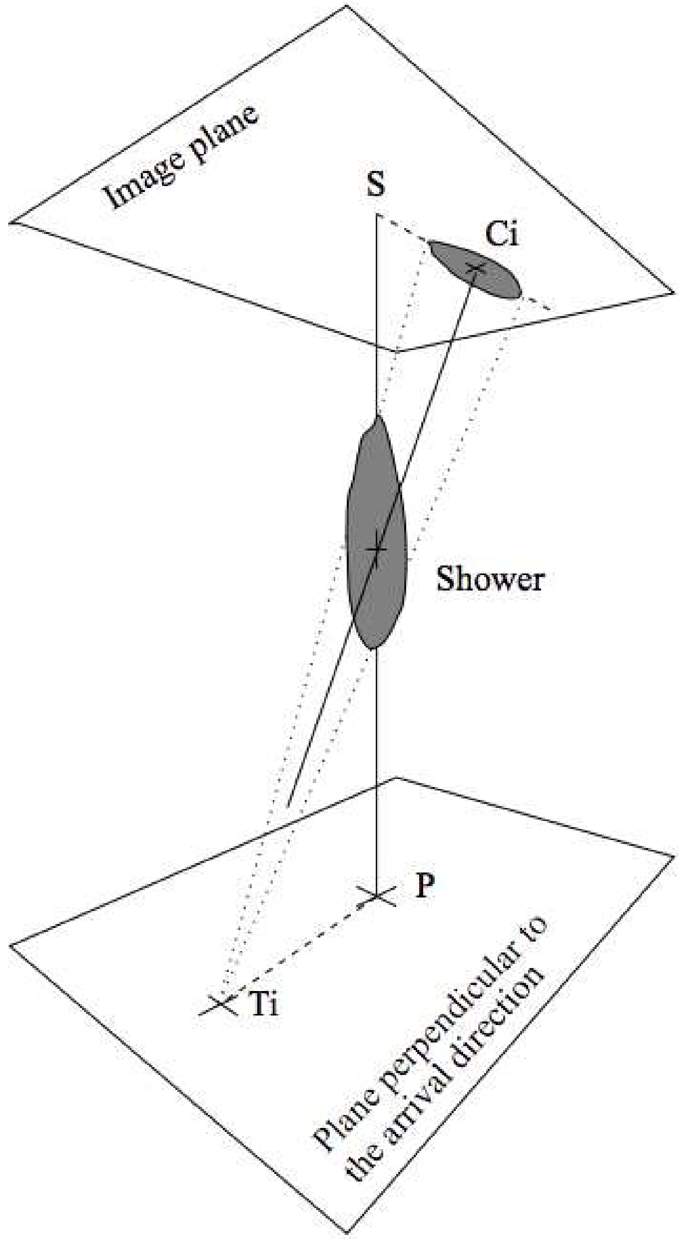

Figure 6–6: Schematic of the projection of the shower into the image plane. P is the core position, found in Section 6.4.2, S is the source location, found in Section 6.4.1, Ti is the telescope's position on the ground, and Ci is the location of the image centroid in the image plane, the focal plane of the telescopes. The height of the shower maximum can be calculated using these derived properties, resulting in Equation 6.3. Figure from [101].

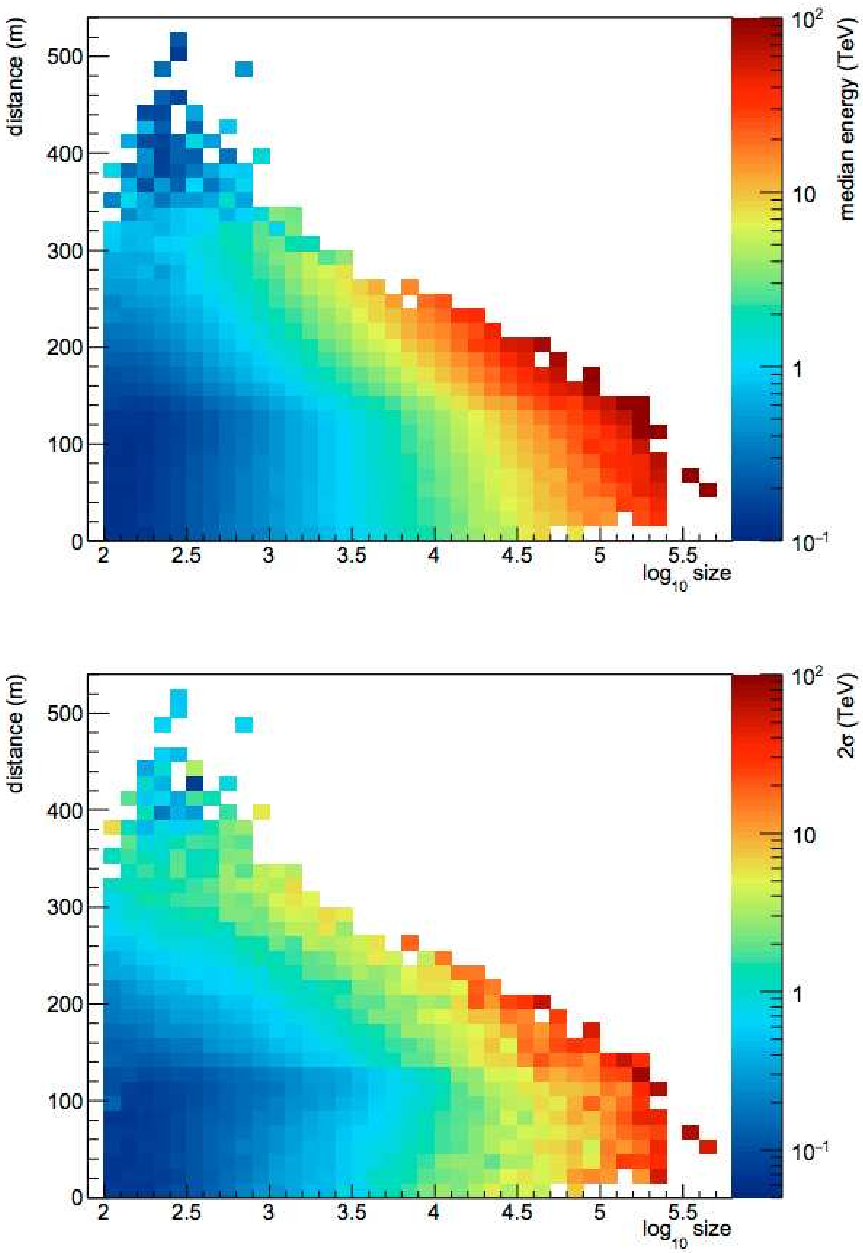

Figure 6–7: *Top:* Example of a gamma ray energy reconstruction table. The x-axis is the image size for the telescope, with the y-axis being the impact parameter. These are used to get the median energy of the event, identified by the z-axis. *Bottom:* Distribution of the standard deviations corresponding to the distribution of energies from the top table. The z-axis, in this case, represents twice the σ value of Equation 6.4.

6.5 Gamma-Hadron Separation

At this point, all the pertinent information about the shower-inducing particles have been found. Next, we need to determine which of the detected showers were caused by gamma rays and which by cosmic rays. A few more parameters, or discriminators, are used to do this, where the expected behavior will be different between the two types of showers. Traditionally, the analysis uses what are called "box cuts", i.e. cutting on individual parameters, to keep the gamma ray signal. However, a new, more advanced, analysis method has been developed recently, using Boosted Decision Trees (BDTs) for a more effective gamma-hadron separation.

6.5.1 Box Cuts

The discriminators used in this step are called mean scaled parameters (MSP), and are used as a measure of how similar the shower's image is to a simulated one. The scaled parameters are usually the mean scaled width (MSW) and the mean scaled length (MSL), and are computed in a similar manner as the energy reconstruction, as follows:

$$MSP = \frac{1}{N_{tel}} \sum_{i=1}^{N_{tel}} \frac{p_i}{\bar{p}_{sim}(z,s,r)} \tag{6.5}$$

where p_i is the calculated parameter value, in this case the width or length from Section 6.3, and $\bar{p}$ is the mean value of the parameter for a simulated gamma ray, observed at a zenith angle z, size s and impact parameter r.

A more robust calculation of the parameters that takes into consideration outlier events is the mean *reduced* scaled parameter (MSCP, if using the width parameter, MSCW, and MSCL if using the length), calculated as follows:

$$MSCP = \frac{1}{N_{tel}} \sum_{i=1}^{N_{tel}} \frac{p_i - \tilde{p}_{sim}(z, s, r)}{\sigma_p} \tag{6.6}$$

where $\tilde{p}$ is the median value of the parameter p in the simulations, and σ_p is the standard deviation of p. Figure 6–8 shows a plot of the mean reduced scaled width distributions for a signal and several background regions, assuming that the background region only contains cosmic rays.

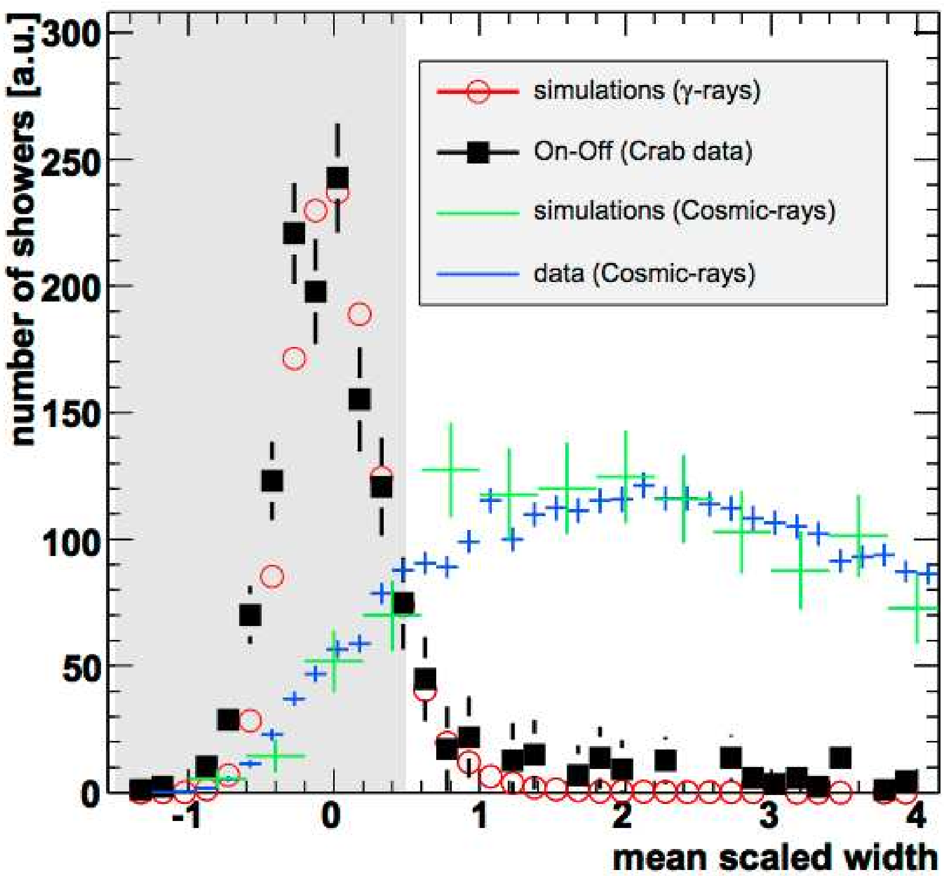

Figure 6–8: Distribution of MSCW for data and simulation of signal and background regions. The distribution of the gamma-ray signal is tighter and with a generally lower value than for the cosmic rays. The On-Off distribution is the background-subtracted counts from Crab data. Image taken from [102].

Cuts on MSCL and MSCW, combined with a cut on θ^2 (explained in Section 6.6) can reject up to approximately 99% of cosmic-ray events while retaining approximately 85% of all the gamma-ray events [103].

6.5.2 Advanced Analysis Method: Boosted Decision Trees

Boosted decision trees (BDTs) is a machine learning method classifier, using multivariate analysis for discriminating between different type of events. A more complex relationship can be found between different discriminator variables to improve event classification, as opposed to "boxing in" the desired events using each variable at a time, independently of each other. The typical way a VERITAS analysis is handled is using these "box cuts", but a new analysis has recently been developed, using BDTs. This section will explain how BDTs work, and how they work as opposed to other machine learning tools like artificial neural networks (ANN) and random forests (RFs). Their use and performance with VERITAS will be explored in Section 6.8, and the results from the analysis of the data with BDT will be used for the search for primordial black holes, as described in Chapter 7.

BDT Example

Boosted Decision Trees start with the making of the first Decision Tree, a two-dimensional structure, with nodes and branches. Figure 6–9 shows an example of a decision tree, as a classifier whether or not any animals in a group is a cat. It is structured as a flowchart, with a parent node; the one that contains all the events, in the case of Figure 6–9, all the animals. The list is then split in branches based on a question: is the animal four-legged? If it is not, it is not likely to be a cat, and all the animals for which the answer is no are then placed in a new list of animals, comprising a daughter node. Those that are four-legged comprise another list of animals that could potentially be cats. Since being four-legged is not enough to identify a cat, a new question is asked, for example whether or not the animal has a tail. The classification is done again on subsequent daughter nodes, and more questions are asked to further identify the animal.

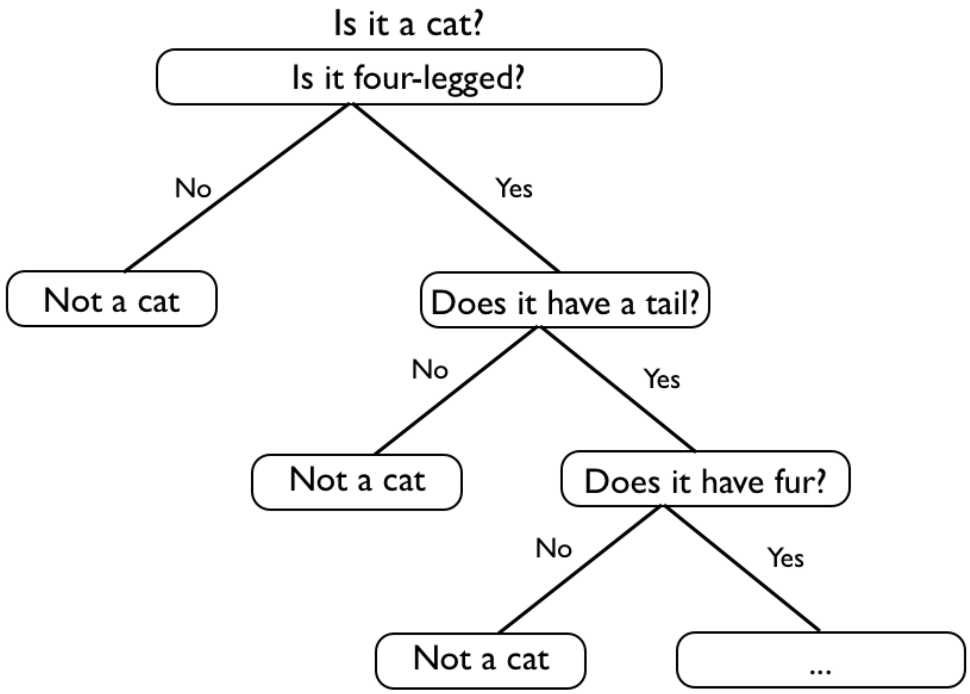

Figure 6–9: Example of a Decision Tree. In this example it is used to identify cats in a list of animals. The parent node is the node containing all the events, in this example asking the question: "is it four-legged?". That question is the discriminant of the mother-node, which has two branches, yes or no. The daughter nodes are the resultant from the answer to the questions. The list created when answering No means that it is not a cat, but the list, if the answer is Yes, leads to more questions, to further assess the features of the animals.

Now, imagine that all the information that we have is the answer to those questions; we do not know ahead of time if the animal is a cat. It is then likely that some of the animals will be misidentified as cats when they are not, or vice-versa. For instance, Manx cats do not have tails, and would be misidentified according to the decision tree of Figure 6–9. Sphynx cats, who do not have fur, would also be misidentified. BDTs is a technique that can help with making an improved classification.

For the purpose of the explanation, let us now imagine that the animals could either be cats or dogs (to follow as an analogy with the VERITAS analysis, where the information being sought is whether or not an event is a gamma ray or a cosmic ray). All the information we have been given is a set of answers to a few simple questions, like if it has fur, its size, the length of its nose, the presence of a tail, what the sound it makes is like, etc... One can then make a simple decision tree much like in figure 6–9 to classify each animal. Much of it will be wrong, especially if limiting oneself to questions like if it has fur, or the presence of a tail. This outlines the first step with BDTs. It starts by making a first tree, and optimizing the classification of that tree. This means figuring out which question is better at correctly identifying the animals. For instance, the sound it makes is a much more powerful indicator. The presence of a tail, or of fur, on the other hand, does not help too much. Figure 6–10 shows what a first decision tree might look like, when using the best discriminators first. Note that there might still be misidentified animals at the end. More questions could be asked in the hopes of improving the discrimination. In fact, when making BDTs, the questions are asked up to the point when the discrimination doesn't improve anymore. However, even then, misidentification can happen, and BDTs use yet another step to improve classification.

As seen in Figure 6–10, some animals have been misidentified. What is done, then, is to give more weight to the misidentified events, and create a new decision tree. This new decision tree will be optimized in much the same way as for the first, but this time the best questions to ask may not be the same. For the purposes of this example, let us claim that the misidentified

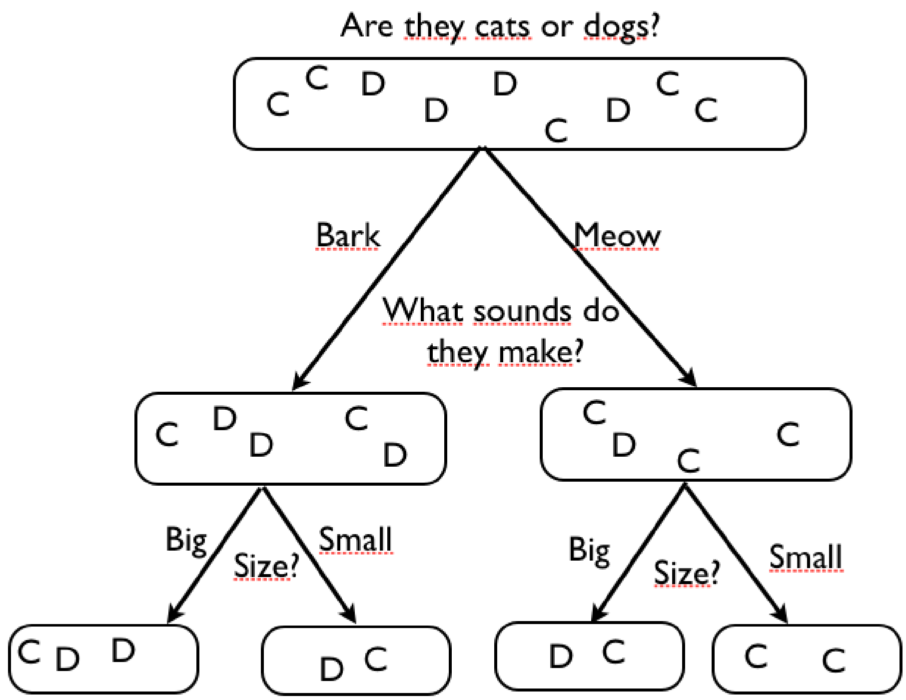

Figure 6–10: Example of the first decision trees built for BDTs. The parent node presents a list of animals, C for cats and D for dogs. The questions are optimized to give the best discrimination to the daughter nodes. In this case, "what does the sound the animal makes sound like?" is the best discriminant, and is asked first. Not all the animals are correctly identified, however, so the second best question is asked, relative to the size of the animal. The final nodes show a list, most with some misidentified animals, still.

cats and dogs will now each count as 2 animals. The left schematic of Figure 6–11 shows the results if the same decision tree was used. Note that the final daughter nodes do not have as good a purity anymore, the bottom left one consisting of 50% cats, as opposed to 1/3 in Figure 6–10. Hence the need to find new, better questions to improve the discrimination. The right schematic of Figure 6–11 shows what that tree would then look like.

The misidentified events of the new tree are again reweighted, and the process is repeated multiple times. This is done until the discrimination cannot

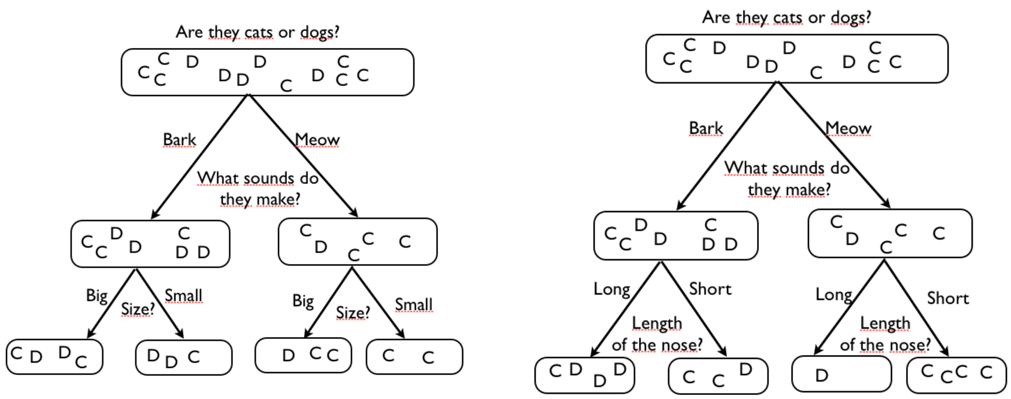

Figure 6–11: Example of the effect of reweighting misidentified animals. *Left:* Using the same decision tree as in Figure 6–10. Note that the purity has diminished in some daughter nodes. *Right:* Optimizing the choice of questions to maximize discrimination with the new weights. Note the improvement compared with the left plot.

be improved further. In the end, one finds a forest of decision trees, which are then used much like random forests, explained later in this section. To first create the tree, an original list of animals, where you know beforehand whether they are cats or dogs, would be used as a testing set. Once that first set has been used to optimize the trees, one can use BDTs to identify other animals not in the training set. With these new animals, one would then answer the questions of each one of the decision trees, and its likelihood to be a cat or a dog would be the average result of each tree.

VERITAS Application of BDTs

The same logic applies with VERITAS. In this instance, the goal of the BDTs is to discriminate between hadronic and electromagnetic showers, and provide a mathematical way of doing so. This will be described here, and compared to the equivalent logic from the cats and dogs example above.

In that case, the parent node will contain a number of signal and background events, N_S and N_B respectively, taken from a training sample. Each event has its set of parameters, and is also given a weight w_i. In the first tree in the BDTs, each event is given the same weight w_i, and is normalized to the total number of events $w_i = 1/(N_S + N_B)$ (in the case of cats and dogs, they each counted as one, for simplicity). Each event will be tested on a parameter, the discriminating variable, leading to the next layer of daughter nodes. The discriminating variable that will be used is the one that does the best discrimination ("what does the sound the animal make sound most like?"), i.e. that gives the best purity p in the daughter node. This is done by calculating the Gini index:

$$\text{Gini} = \left(\sum_{i=1}^{N} w_i\right) p(1-p) \tag{6.7}$$

where p is defined as the fraction of weight of the daughter node due to signal events, and w_i is the weight of event i.

Maximizing the difference of Gini indices between the parent and the two daughter nodes will determine the best splitting parameter:

$$\max(C) = \text{Gini}_{parent} - \text{Gini}_{rightnode} - \text{Gini}_{leftnode} \tag{6.8}$$

Once the splitting is maximized, the same is done for the next node, and again until there is no increase in event separation, and before overtraining sets in (overtraining will be explained further in Section 6.8). The final daughter nodes are labelled as signal nodes if more than 50% of the weights of the events in it are signal (cat nodes if more than 50% of the animals in it are cats, and vice-versa if they are dogs), and the others are the background leaves.

One decision tree will optimize the set of cuts for maximal signal purity, however it is subject to statistical fluctuations in the training sample, and some events that are "harder" to identify are misidentified as background (like some dogs or cats having been misidentified). Boosting, or re-weighting of the misidentified events, can help with both of those problems. As mentioned earlier, all the events have the same weight in the first tree, however, in the end, some events will be misidentified. Those misidentified events will be boosted with a higher weight for the next tree (the misidentified cats and dogs count as 2 for the next tree).

To do this, one needs to define the following:

$$Y_i = \begin{cases} +1 & \text{if events } i \text{ is signal} \\ -1 & \text{if background} \end{cases} \tag{6.9}$$

and

$$T_m(x_i) = \begin{cases} +1 & \text{if event } i \text{ is classified as a signal event in tree } m \\ -1 & \text{if event } i \text{ is classified as a background event} \end{cases} \tag{6.10}$$

A tree is optimal when $Y_i = T_m(x_i)$. If that equality is not respected, this means event i is misclassified, and its weight will be boosted by a factor α:

$$\alpha_m = \beta \ln\left(\frac{1-\epsilon_m}{\epsilon_m}\right) \tag{6.11}$$

with β being the learning rate, specified by the user, and ϵ_m is the fraction of misclassified events in tree m:

$$\epsilon_m = \frac{\sum\limits_{Y_i \neq T_m(x_i)} w_i}{\sum\limits_{i=1}^{N} w_i} \tag{6.12}$$

This will all be used to redefine the weight of the misclassified events as follows:

$$w_i \;=\; w'_i \exp \alpha_m \tag{6.13}$$

where w'_i is the event's weight from the previous tree. All the events' weights are then renormalized to ensure that $\sum_i w_i = 1$.

A second tree is generated in the same way as the first one, this time using the new weights on each events when maximizing the Gini-index difference in that new tree (choosing which questions are now best to get the decision tree like the right schematic of Figure 6–11). Once the last signal and background leaves are done, the same reweighting mechanism is done on the new tree output, used for the subsequent tree, and so on until the increase in separation is maximized, and before overtraining sets in. This results in a forest of m trees, trained and optimized using a training sample. When using a testing sample of data (or eventually real data), each event will be assigned a value $T_m(x_i)$ for each tree m as defined in Equation 6.10. The final "score" of the event will be determined as such:

$$T(x_i) \;=\; \sum_{m=1}^{N_{Tree}} \alpha_m T_m(x_i) \tag{6.14}$$

where $T(x_i)$ will tend towards -1 if the event is background, and $+1$ if it is signal (equivalently, in our example, $+1$ if a cat and -1 if a dog).

The BDT method used on VERITAS was developed using *ROOT* version 5.34.14, with the *TMVA* package version 4.2.0. It has been implemented in the *EventDisplay* analysis package version 480, one of the 2 analysis packages developed by VERITAS for data analysis. This version of *EventDisplay* is used in the analysis for the work reported in this thesis, in the search for Primordial Black Holes.

For the VERITAS BDT analysis, classifiers were chosen to maximize event discrimination. The Hillas parameters are good discriminators, but a few others were found to be useful, all already computed by the *EventDisplay* analysis package:

- Mean Reduced Scale Width (MSCW), see last Section
- Mean Reduced Scale Length (MSCL)
- χ^2 value of the estimated energy against the reconstructed energy. The χ^2 is calculated using the estimated energy of each individual telescope against the weighted average from the reconstruction.
- Height of the shower maximum
- χ^2 value of the height of shower emission. The emission height is calculated in pairs of 2 telescopes, and the χ^2 is taken from the emission height calculated with all possible pairs of telescopes. No χ^2 is used if only 2 telescopes can reconstruct the event.
- Amplitude of the second largest image
- Distance to the shower core, had it hit the ground.

The training sample was composed of simulated gamma-ray events. The background events were taken from actual data, homogeneously distributed across the field-of-view, at varying zenith angles and night-sky background levels, with four telescopes and good weather conditions. It is important for the gamma-ray simulation to follow the same characteristics, so that all data-taking conditions are represented, and to minimize the amount of bias when training the decision trees. The training is done in energy range and zenith angle bins, to optimize performance across the different conditions. The binning was chosen so as to allow high statistics, because a higher energy range as well as a higher zenith angle will significantly reduce the number of events. Figure 6–12 shows the parameters' behavior for an example energy and zenith angle bin.

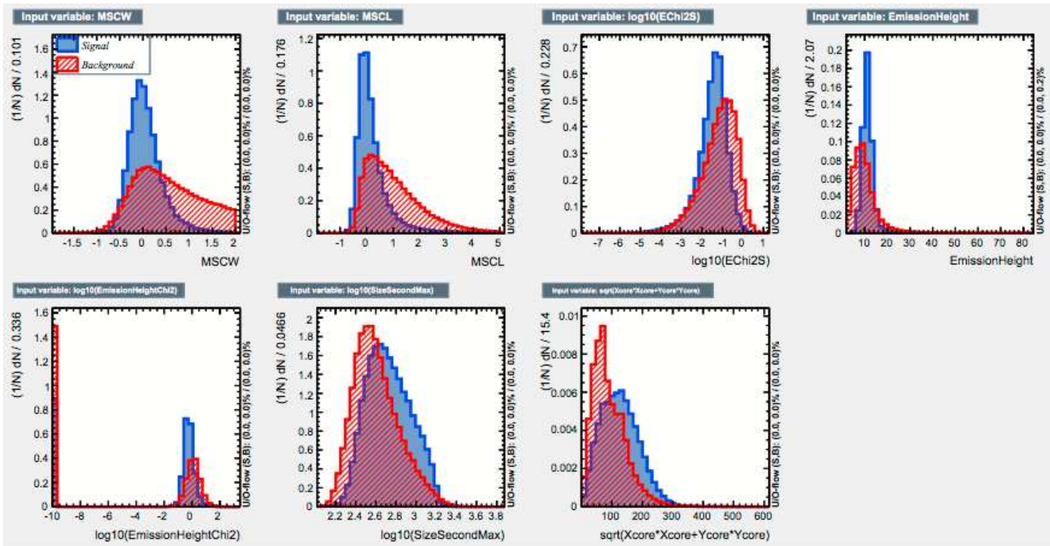

Figure 6–12: Distribution of the different parameters used in the BDT analysis. The entries at a value of -10 for "Emission-HeightChi2" come from events that were only reconstructed using two telescopes (see text). Image credit: Elisa Pueschel.

A common problem in machine learning is the risk of overtraining. Overtraining occurs when the training was too insistent, and the decision trees become too finely-tuned with the sample. Because of this, the newly-trained BDTs are oversensitive to their own statistical fluctuations, and so becomes less performant when presented with a different sample with a different set of statistical fluctutations. This is avoided by using a test sample of data. If the trees were trained successfully, the test samples should follow the same probability density function. A Kolmogorov-Smirnov test does that by comparing the largest difference in the cumulative density function between the testing and training samples. If that difference is larger than what would be expected at a desired confidence level, then it is not considered as coming from the same probability density function. In the VERITAS implementation, if the result of the test gives a number between 0 and 1, it means that the two samples' results come from the same distribution. If the test gives 0, it indicates overtraining. Figure 6–13 shows the difference between proper training and overtraining on

VERITAS training and testing data sample. Overtraining can be mitigated by using either more training events, or limiting the depth (the number of node layers) a decision tree can have.

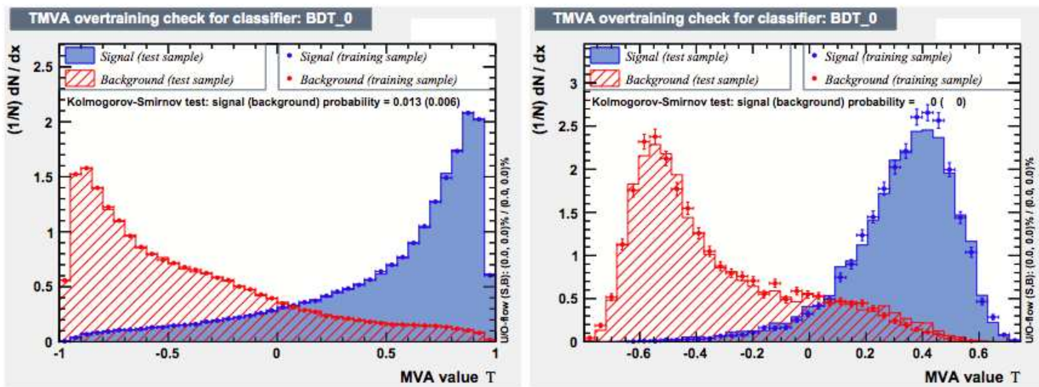

Figure 6–13: Example of proper training (*left*) and overtraining (*right*) of BDTs. In the right plot, the testing sample shows some points that do not agree as well as on the left plot. with the training sample's distribution, indicating overtraining. Image credit: Elisa Pueschel.

Alternate Machine Learning Methods

Other machine learning methods that could be used are Artificial Neural Networks (ANNs) and Random Forests (RFs). RFs are very similar to BDTs. They also consist of a forest of Decision Trees. In this case, a large number of Decision Trees are generated, each with a random sample of the training data and a random sample of discriminating parameters. Each tree is subject to random fluctuations, which should be cancelled by the fluctuations of other trees. In the end, the event identification is the average of its classifications by all the trees. The major differences between RFs and BDTs is that the former uses a parallel set of decision trees with random sets of the sample and random sets of parameters for each tree while keeping the events weights the same. The latter uses a set of serialized decision trees with the same set of parameters on all the events, but each subsequent tree gives more weight to misclassified events in an effort to recuperate them. RFs are less subject to overtraining than BDTs, however well-tuned BDTs can potentially outperform RFs. BDTs tend to require less trees and each tree to be less deep, making them faster to train and use as well.

ANNs, on the other hand, study the relationship between the parameters and the output. The input nodes are composed of parameters, whereas the output nodes classify the event. In between, hidden layers of nodes would be used to determine the relationships between the parameters. One of those hidden nodes would receive a weighted average between different parameters, and then send that to a node in the next hidden layer (see Figure 6–14 for a schematic using the cat example). The training here is in the weights between nodes of neighboring layers. This is powerful when one doesn't know what the influence of different parameters is on the classification. However, trained ANNs eventually become black boxes, since the weights are known but become difficult to interpret, and the training and use takes significantly longer than either RFs or BDTs.

6.6 Signal, Background and Significance

6.6.1 Signal and Background Regions

As good as the gamma-hadron separation can get, there will always be some irreducible background left, either from electron or positron-induced showers, or from hadronic showers that happen to look like gamma-ray ones, e.g. from production of a π^0 early in the shower process. A background-subtraction technique is then necessary to extract a purer signal.

One of the easiest ways to do this analysis is to select a region of interest, usually a region with a known or potential gamma-ray source (ON region), and compare the number of events that pass the cuts with those of another region

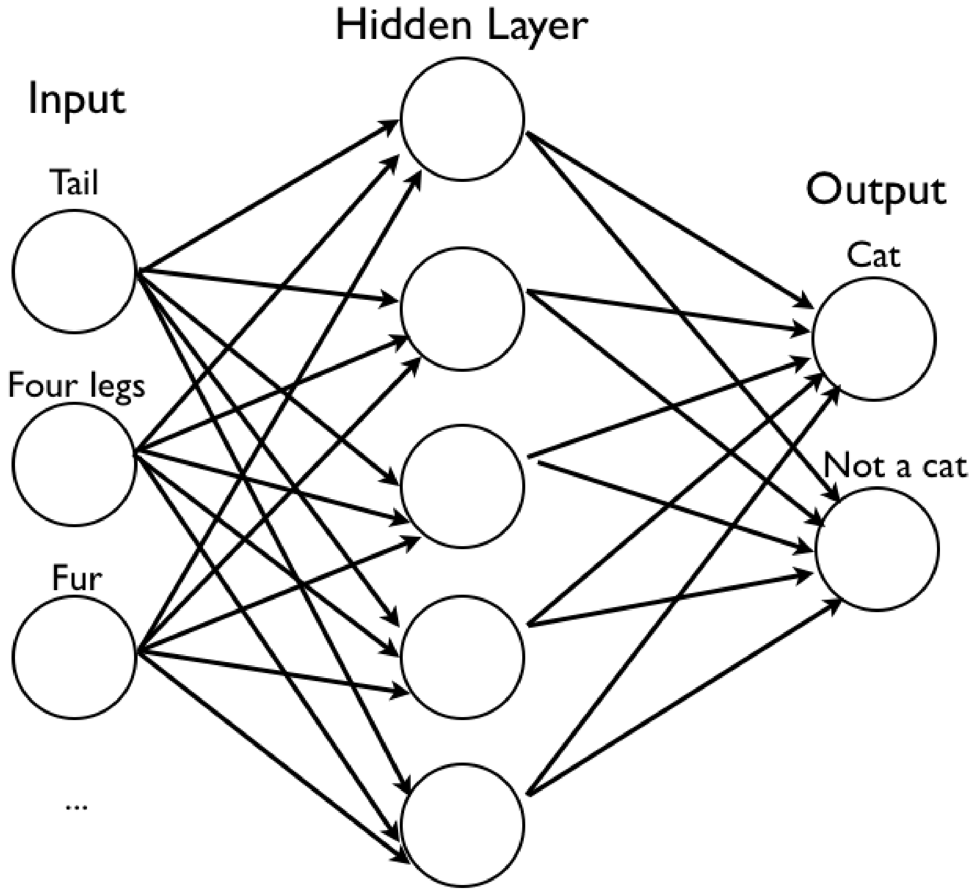

Figure 6–14: Schematic of ANNs decision scheme. Following on the example of identifying a cat, the input nodes are a set of parameters used for identification for a given object, going through hidden layers meant to test the relationships between the parameters and the output. The output nodes will classify each object as a cat or not.

assumed to be signal-free (OFF region). The size of the ON region is defined by θ, the angle between the candidate source direction and the reconstructed direction of the gamma-ray-like events. This is the same θ used in the θ^2 cut mentioned in the last Section. A typical θ^2 plot is shown in Figure 6–15. A cut on the square root of θ^2 defines the size of the ON regions, its radius is the square root of its value. The definition of the OFF region is more complicated and will be discussed next.

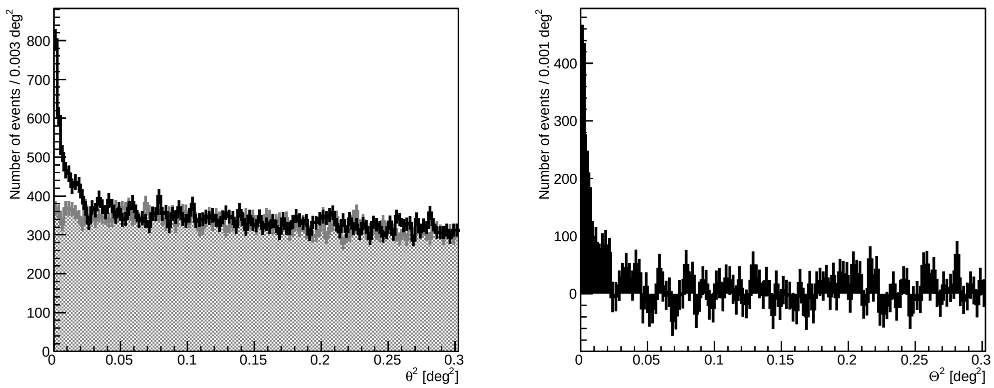

Figure 6–15: Distribution of θ^2 for data taken on the Crab Nebula. *Left:* θ^2-distribution where the black curve is the count from the ON region (the position of the Crab Nebula), and the grey-shaded region comes from the OFF regions (the positions used as background). *Right:* Residuals of the plot on the left, after background-subtraction. The peak below 0.03° is the excess due to the Crab Nebula.

Note that θ^2 can also be used to determine the angular resolution of the telescopes, or the gamma-ray point spread function (PSF). The behavior of the PSF as a function of the gamma ray's energy and incoming zenith angle is an important quantity to understand in the analysis involved in the search for primordial black hole evaporation. This will be explored further in Section 7.3.

There are two main ways of selecting the OFF regions for the analysis. The simplest one is simply to point the telescope directly at the source and use the center of the field-of-view as the ON region, and then point to a background region right next to it (for example at 30 minutes away in right ascension for 30 minute runs) for the OFF region. While this method works well, it has the main problem of having to spend 50% of observing time on background.

The other method provides a solution to this problem. By pointing the telescope with a slight offset from the ON region (typically 0.5°), the ON and OFF regions are taken simultaneously. This method is called *wobble-mode* observation. Typically, the wobble offsets are taken in four directions (north, south, east and west), so that the background can be sampled around the source and averaged. This reduces systematic errors.

Two analysis methods are used in wobble-mode to estimate the background. One is called the ring background method [104], where a ring around the source region is used. The other one is called the reflected region method [104], using a series of OFF regions of identical shapes (and sizes, as defined by the θ^2 cut used in the analysis) to the ON region. For this last method, the OFF regions have to be in the same offset from the pointing direction as the ON regions.

6.6.2 Excess and Significance

Using the ON and OFF regions determined in the last section, one can derive the number of excess events in the source region, compared to the number of events in the background regions:

$$N_{EXCESS} = N_{ON} - \alpha N_{OFF} \tag{6.15}$$

where N_{ON} and N_{OFF} are the number of events in the ON and OFF regions respectively, and α is a normalisation parameter.

In the case of the method with different pointings for ON and OFF methods, α will simply be the ratio of time spent on the ON region to the time spent on the OFF region. For the ring background method, it will be the ratio of the solid angles subtended by the ON and OFF regions. In the case of the reflected region method, it will be the inverse of the number of OFF regions used (another way of looking at it is that it is the ratio between the number of ON regions (in this case, one) and the number of OFF regions).

The uncertainty on N_{EXCESS} can be derived through error propagation:

$$\Delta N_{EXCESS} = \sqrt{\Delta N_{ON}^2 + \alpha^2 \Delta N_{OFF}^2} \tag{6.16}$$

where ΔN_{ON} and ΔN_{OFF} are the errors on the number of counts on the ON and OFF regions respectively.

Assuming that the counts follow Poisson fluctuations, then the error on the excess can be rewritten as:

$$\Delta N_{EXCESS} = \sqrt{N_{ON} + \alpha^2 N_{OFF}} \tag{6.17}$$

The significance S on the excess counts then becomes:

$$S = \frac{N_{EXCESS}}{\Delta N_{EXCESS}} = \frac{N_{ON} - \alpha N_{OFF}}{\sqrt{N_{ON} + \alpha^2 N_{OFF}}} \tag{6.18}$$

It has been shown that the above formula is an approximation of the significance, and does not properly account for the uncertainty in the number of background counts [105]. An alternative was proposed following a log-likelihood test of a null hypothesis, where all the counts are assumed to be background:

$$\sigma = \sqrt{2}\left[N_{ON}\ln\left(\frac{1+\alpha}{\alpha}\frac{N_{ON}}{N_{ON}+N_{OFF}}\right) + N_{OFF}\ln\left((1+\alpha)\frac{N_{OFF}}{N_{ON}+N_{OFF}}\right)\right]^{1/2} \tag{6.19}$$

Typically, the excess is considered significant for a new detection if N_{EXCESS} is large enough to lead to a Significance $\geq 5\sigma$ as determined by Equation 6.19.

6.7 Instrument Response Functions

One last bit of information that is needed for an analysis are instrument response functions (IRFs). This is generally needed for calculation of a source's spectrum, and to determine its flux. These functions are also needed in the analysis for the search for PBHs, when it comes time to calculate the upper limit on the rate-density of PBHs (more on that in Chapter 8).

IRFs are needed to convert results from an experiment to physical units. There are three that are necessary in the VERITAS analysis:

- Lookup Tables: Mentioned in Section 6.4.4. These tables convert the shower image's parameters (noise, impact distance, pointing direction, height of shower maximum) into an energy. See Figure 6–7
- Effective Areas: Mentioned in Section 6.5.2. They are used to convert a number of gamma-ray counts into a physical flux. They are a measure of the effective collection areas of the telescopes as a function of the energy.They can be thought of as a measure of the efficiency of reconstructing a gamma ray of a given energy, as well as the different types of cuts used in the analysis, the gamma ray's arrival zenith angle, as well as the wobble direction and offset, and the optical efficiency. This is calculated via simulations, from how many simulated gamma rays are properly reconstructed at a given energy. See Figure 6–16
- Radial Acceptance: Mentioned in Section 6.6, they are used to adjust the number of gamma rays seen as a function of the camera position. The reconstruction of a gamma ray is more likely at the center of the camera than at the edges. See Figure 6–17

6.8 Performance of Boosted Decision Trees

The information calculated in the last section can be done using results from the gamma-hadron separation from either box cuts or BDTs. Both of these work as long as the behavior of the two remains similar with regards to the calibration or when reconstructing a standard source spectrum. The

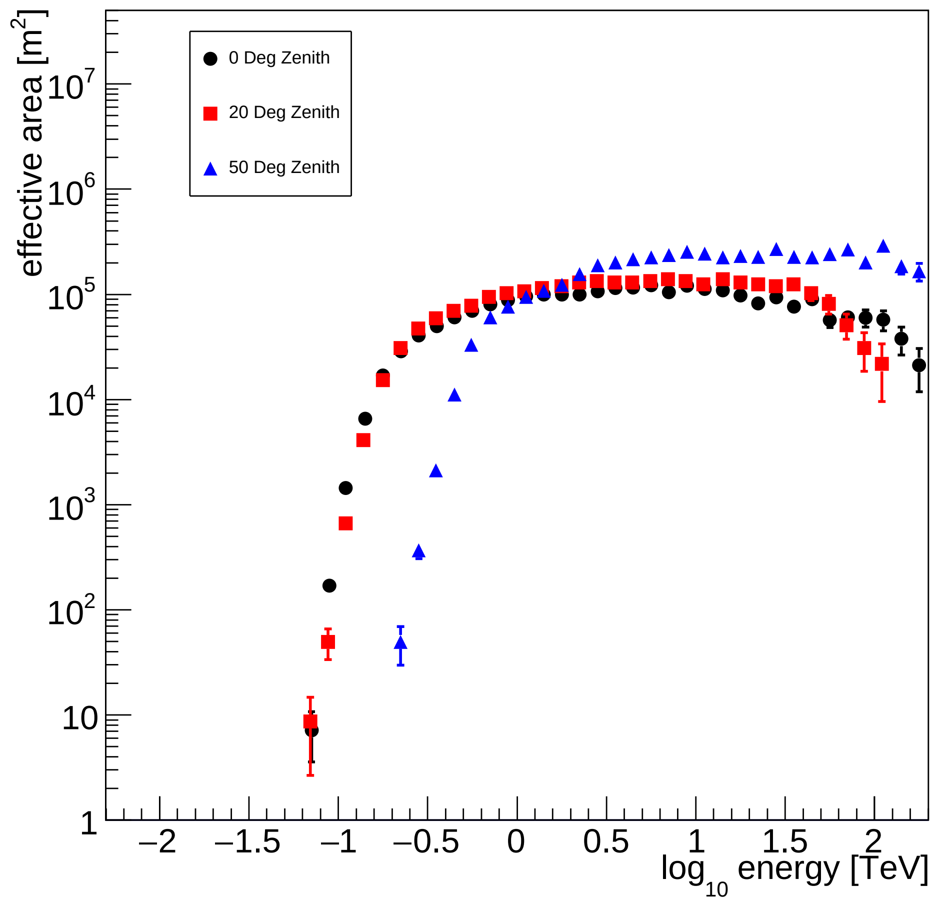

Figure 6–16: Example of effective area curves. The effective areas when pointing at a zenith angle of 0, 20 and 50° are shown. The larger the zenith angle, the higher the energy threshold, but also the higher the sensitivity at high energies.

ultimate goal is to obtain a better significance using BDTs compared to Box Cuts for an identical dataset.

The first test is a measure of the efficiency of the cuts, as shown in Figure 6–18. The idea is to use a cut that maximizes how much signal is seen over the background, and how it affects the overall detection significance.

This is useful for the selection of the cuts. Typically, box cuts are separated into three "classes": soft, moderate and hard. They are defined according to the spectrum of the source being looked at, and have different energy

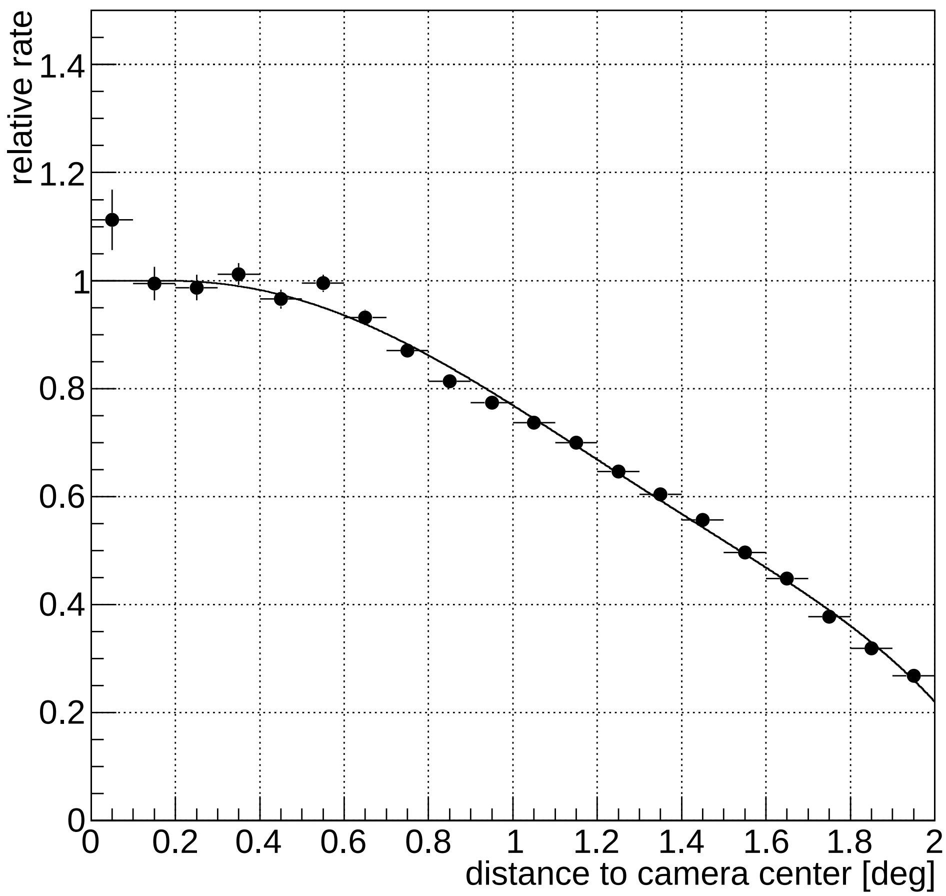

Figure 6–17: Example of a radial acceptance curve. The points come from data, and the line is a fit, using a 5^{th} order polynomial, used in the VERITAS analysis. This indicates that the probability of reconstructing an image is higher if it is closer to the center of the camera.

thresholds. In general, soft cuts are used for sources with a soft spectral index (a power-law of index -3), moderate cuts are used for Crab-like spectra (index of -2.5) and hard cuts are used for sources with harder spectra. This does have an effect on the energy threshold of the analysis, soft cuts having a lower one, at 150 GeV, as opposed to hard cuts having an energy threshold of ∼500 GeV, whereas moderate cuts have a threshold in between, at ∼250 GeV. The

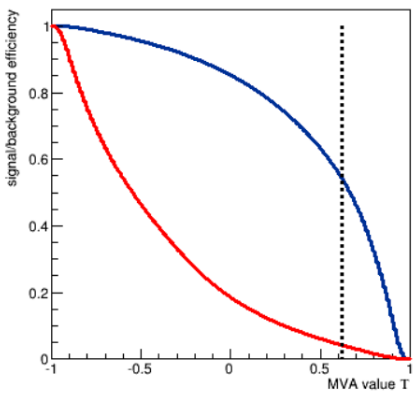

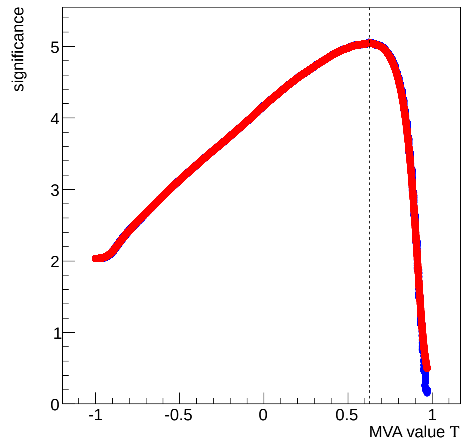

Figure 6–18: *Left:* Efficiencies of signal (blue) and background (red) as a function of the BDT cut value (MVA value T, where MVA stands for multivariate analysis). *Right:* Significance (in units of standard deviation) calculated from the left plot, as a function of the cut value T. The dashed line shows the maximum of significance (determined for a Crab-strength source), and is shown on the plot on the left as well. Image credit: Elisa Pueschel.

cut optimization done with BDT was chosen to match the behavior of the box cuts as close as possible, with respect to the source spectrum.

In the analysis presented in this work, BDT moderate cuts were used since, as seen in Chapter 4 with Equation 4.31, the spectrum behaves as a power-law of index -1.5 up until ∼5-10 TeV (depending on how much evaporation time is left for the primordial black hole), where it switches to an index of -3. Given that the spectrum will be hard from the moderate cuts' energy threshold up until 5-10 TeV, and then soft, BDT moderate cuts are a good compromise (as well as friendlier to the CPU during the final analysis). The performance of BDT moderate cuts will be compared here with the equivalent box cuts.

One of the tests to compare the performance between the two cutting methods, is to compare the effective areas (discussed in Section 6.7). Effective areas are a measure of the efficiency of the event reconstruction, and are defined as such:

$$EffA(E) \;=\; \left(\frac{N_{rec}(E)}{N_{throw}(E)}\right) \times A \tag{6.20}$$

where EffA(E) is the effective area at energy E, $N_{rec}(E)$ is the number of events having been reconstructed at energy E, $N_{throw}(E)$ is the number of simulated events at energy E, and A is the area over which the gamma rays were simulated.

In essence, it is a representation of how efficient the set of cuts really is, as box cuts will reconstruct less of the simulated gamma rays than BDTs. This is visible in Figure 6–19, that shows the comparison of the effective areas between the two. BDTs have better reconstruction efficiency at higher energies (about 10% at 5 TeV), while losing $\sim$ 10% below 200 GeV.

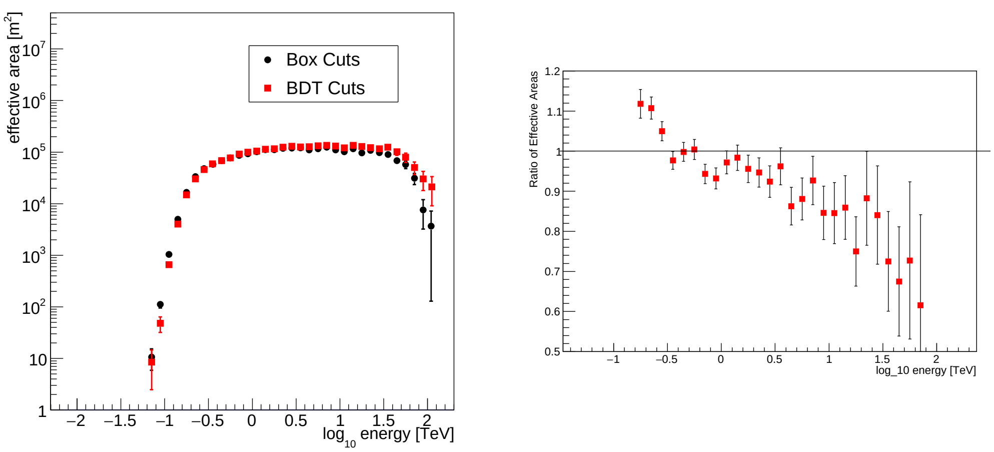

Figure 6–19: Comparison of Effective Areas between box cuts (black circles) and Boosted Decision Trees (red squares). *Left:* The 2 effective areas plotted on top of each other. *Right:* The ratio of the effective area of box cuts to BDT cuts.

BDTs were also tested on their performance when analyzing actual data. In VHE astrophysics, the Crab Nebula is considered to be a "standard candle", as it is a very strong and steady source of gamma rays in this energy range [106]. For that reason, it has been used for the performance analysis.

To show that BDTs work as they should, the analysis that uses it should then be able to reproduce the Crab spectrum. Figure 6–20 shows such a comparison. The spectrum is in very good agreement between BDTs and the box cuts.

Sensitivities can also be compared. Table 6–1 shows the difference in total significance between the two sets of cuts, showing an overall improvement. Figure 6–21 shows how much time is needed to get a detection (significance of 5σ) for each source strength.

Property	Box Cuts	BDT Cuts
N_{ON}	613	607
N_{OFF}	537	294
σ	45.9	49.8
γ-rate (1/min)	7.3 ± 0.3	7.4 ± 0.3
background rate (1/min)	0.36	0.2

Table 6–1: Comparison of results from the analysis of four Crab data runs (80 minutes). As can be seen, BDTs remove about 45% of the background, with little effect on the signal. This results in a net increase in the significance from the same data.

Finally, the performance can also be compared in terms of how many ON and OFF events are found with each set of cuts. Table 6–1 shows a slight loss of ON events of $\sim 1\%$, but cuts down $\sim 45\%$ of the OFF events. This results in a $\sim 8\%$ increase in significance for the Crab Nebula.

6.9 Conclusion

The standard VERITAS analysis has been described here, as well as a new analysis tool that has been recently developed by the Collaboration, using

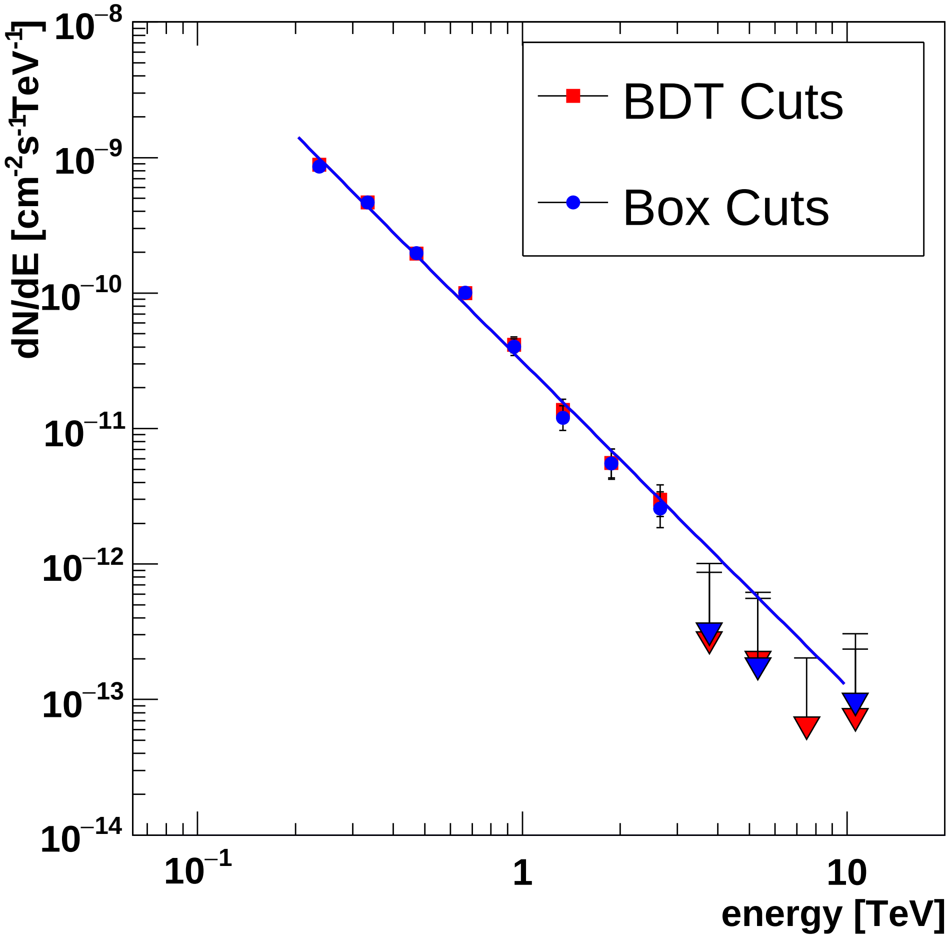

Figure 6–20: Comparing the spectrum of the Crab Nebula using box cuts (blue points) and Boosted Decision Trees (red squares). The minimum significance of a data point is set to 3σ. The arrows represent the 95% CL upper limit for that energy bin.The two curves are the best fit of the spectrum. Both fit agree very well, indicating that the BDT cuts work as they should. The same four Crab runs were used to produce both spectra.

boosted decision trees. This will output a list of events, recognized as gamma-like or not. This list is going to be useful for the PBH analysis, described in the next chapter.

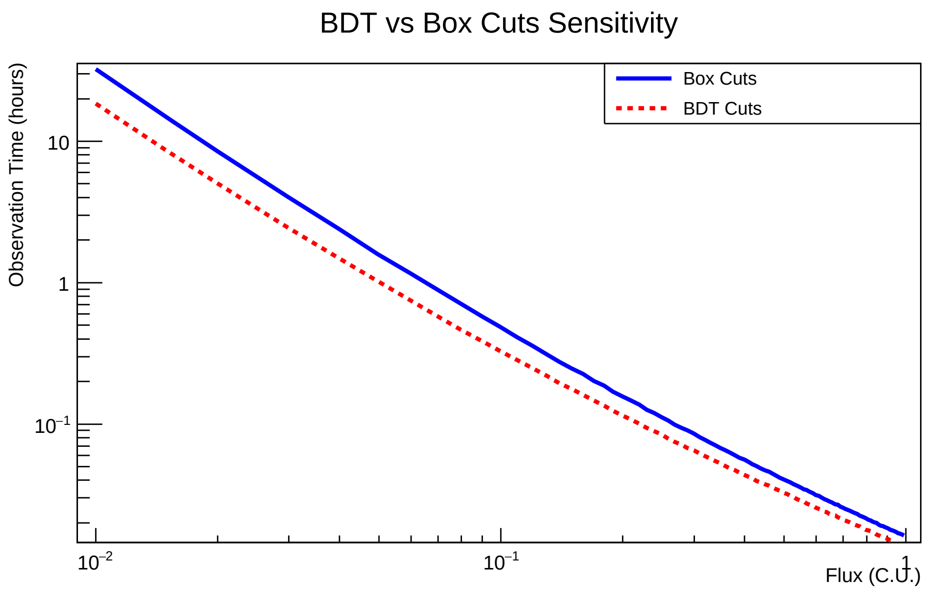

Figure 6–21: Comparison of the sensitivity between box cuts and Boosted Decision Trees. This was done using 4 V5 Crab runs, or 80 minutes of data. The y-axis gives the observation time required for the source of a given flux to reach a 5σ detection.

CHAPTER 7
Analysis for the Primordial Black Hole Search

The standard VERITAS analysis is an integral part of the search for primordial black holes (PBHs), however it is not enough. It will output a list of events that pass the boosted decision trees cut, meaning that they exhibit the characteristics of gamma rays. Since there will always be a subset of cosmic rays that look like gamma ray events, despite the best efforts of the analysis software, those events can only be said to be “gamma-like”. This chapter will describe the next step in the analysis that is needed, in order to detect bursts of gamma rays coming from PBHs.

7.1 Construction of the Run List

The way to look for PBHs is in archival data, in the hopes that the telescopes caught the final PBH evaporation at the right time and right direction, by chance. Since there is no preferred or expected time and direction for the final evaporation of a PBH, proceeding in this way incurs no penalty when looking for PBHs, as opposed to targeted observations. Looking at the maximum number of data runs would then increase the probability of a chance exposure.

However, not all of the data runs can be used. Bad weather, as well as occasional hardware problems, can severely impact the quality of the data. The VERITAS collaboration has developed an online tool for data quality monitoring (DQM) that will process the data and look for any potential problems with the runs, within a few hours of the data-taking. This is used in the run selection, removing any runs with hardware problems, those exhibiting pathological behavior caught by the DQM, and those where the weather was unstable and the skies were not clear. Also, VERITAS' sensitivity as well as the event reconstruction efficiency is reduced when pointing at lower elevation (closer to the horizon). Because of that, runs taken at an elevation lower than 50° will not be used in this analysis.

For the weather, far-infrared (FIR) cameras are used to measure the sky temperature. They operate in a spectral band from 8 to 15 μm. This band corresponds to a water vapor absorption line. If vapor is present in the atmosphere, like if there is a cloud in the field of view, the FIR will detect it, reading it as a variation in temperature. The runs selected require the sky temperature to be stable over their duration, within 0.3°C. Figure 7–1 shows the measured sky temperature for two runs, one where no clouds were present (an accepted run), and one with clouds (a rejected one). Note that the good one is not only more stable, it also presents an overall lower sky temperature.

As explained in Chapter 5, VERITAS has been operating with four telescopes since April 27^{th} 2007. The initial configuration is referred to as V4. In the summer of 2009, one of the telescopes (T1) was moved towards a more optimal position to enhance the array's sensitivity (V5). In the summer of 2012, the PMTs were replaced with higher quantum-efficiency PMTs, enabling the telescopes to reach yet higher sensitivity (V6). The data used in this work will be from the V5 period. In future work, all the data should be used, but for the scope of this work, using the V5 period allows for a more direct comparison with prior results from VERITAS, in [88].

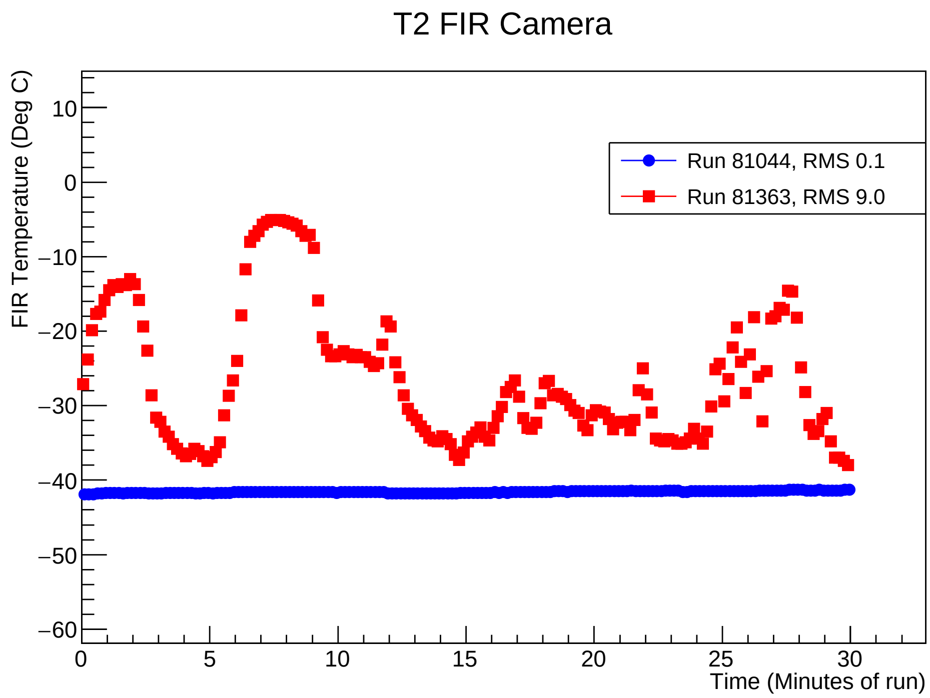

Figure 7–1: Evolution of the measured FIR sky temperature for two runs. The blue points show a stable FIR sky temperature, indicating good weather conditions and hence a good, usable run. The red points show a large variation of the FIR sky temperature, indicating bad weather and a run that will not be used in this analysis.

7.2 Effects of Varying Time Window

Previous searches for PBHs using imaging atmospheric Cherenkov telescopes (IACTs) [80, 65] looked for bursts of gamma rays of a duration of one second. While they were able to obtain interesting limits on the rate-density of PBH evaporation, it does not mean that this is where the respective telescopes were the most sensitive. More recently, H.E.S.S. looked into expanding time windows [90] to find which one would be the most optimal. In order to do that, they determined their optimal sensitivity limits using time windows of 1, 2, 5, 10, 30, 45, 60 and 120 seconds. They found a broad minimum at 30 seconds, and so showed their new limits for both 1 and 30-second time windows (limits of 4.9×10^4 and 1.4×10^4 pc^{-3} yr^{-1} respectively, at a 95% CL).

The searches with Milagro also explored different time windows [107], in their case, binning the sky in spatial coordinates and scanning each using different time windows. They found they were the most sensitive at a time window of 1 second, with a limit of 3.6×10^4 pc^{-3} yr^{-1}. The details of all the previous searches have been described in Chapter 4.

The analysis in this work also looks at different time windows. This chapter and the next will describe this search, computing the limits and showing how they behave as a function of the time window. The aim is to find which time window VERITAS is most sensitive to. With shorter time windows, the limits would be less constraining due to low probability of getting a signal, whereas with longer time windows, there will be more background events, so the $\sqrt{N}$ fluctuations will get larger and mask a small signal, which would also serve to make the limits less constraining. This search aims to find which time window balances those two effects optimally. Recall that Figure 4–8 showed the time profile of PBH emissions towards the end of its lifetime. The increase in emissions follows a power-law, leading to a steep rise the closer the PBH gets to its end.

7.3 Angular Window Search

The basic technique in the search for PBH evaporation is to look for bursts of gamma rays that come from the same part of the sky, in a given time window. This section explains how the gamma rays are said to be coming from the same point in the sky.

Since the PBHs being looked for by VERITAS would have a mass at formation of $\sim 10^{14}$g, or $\sim 10^{-20}$M$_\odot$, it follows that they had a Schwarzschild radius of 10^{-15}m. Gamma rays from a PBH evaporation would, from the point of view of the telescopes, be coming from a point source. This would suggest that the gamma rays' arrival directions would have to be identical. However, due to the spread of a given gamma ray Cherenkov shower, and uncertainties in the event position reconstruction, 2 gamma rays coming from the same point source will always show some level of separation. This will result in a point source appearing somewhat extended. The width of the resulting image is called the gamma-ray Point Spread Function (PSF).

7.3.1 PSF Dependence in Energy and Elevation

VERITAS is often quoted, based on Monte Carlo simulations, to have a gamma-ray PSF of less than $0.1°$ at 1 TeV at the 68% CL [108], so previous searches with VERITAS simply asked for the events of a burst to all arrive within $0.1°$ of each other in order to be likely to be coming from the same point in the sky. H.E.S.S. used the same radius of $0.1°$, and Whipple used $0.13°$.

Since the sizes of gamma-ray Cherenkov showers vary with energy as well as with elevation, it is to be expected that the PSF will also vary with those. Monte Carlo simulations can be used to characterize the PSF as a function of energy and elevation, but prove inadequate due to the effects of systematic errors [109]. A more suitable option is to look at the distribution of the arrival directions of the Crab Nebula's very-high-energy (VHE) gamma rays.

The Crab Nebula, considered a standard candle in VHE astrophysics (as explained in Section 6.8), is ideal for such a study. Since the Crab Nebula is effectively a point source for VERITAS, all its gamma rays should come from the same location in the sky. As Cherenkov showers have an inherent spread, the resulting image of the Crab Nebula will look somewhat extended. By analyzing Crab runs, one can get θ^2 distributions (see Section 6.6.1) for different zenith angle and energy bins, which can then be used to estimate the PSF of the experiment under those conditions.

Note that the PSF is taken to be constant as a function of the reconstructed position in the camera. In other words, the error on the position reconstruction will remain the same at any position in the camera. This could be investigated, but requires dedicated calibration runs with the Crab being positioned in various parts of the camera. This becomes difficult to do as valuable observing time would be needed in order to gather the necessary statistics. Another method to get this information would be through Monte Carlo studies, taking into account the resulting uncertainties. For this work, the assumption of a constant PSF is taken.

For this analysis, all the good-quality Crab runs during V5 are used, determined from the same criteria that were used to select the run list for the PBH search analysis. This corresponds to 314 runs, for a total time of 105 hours. The same cuts as in the PBH search analysis were used here, that is Boosted Decision Trees (moderate cuts). Every reconstructed event is used, and the angular difference θ between the event's position and the position of the Crab Nebula is used to make a θ^2 distribution. The θ^2 plot for all the Crab runs, with all events from each energy and elevation (above 50°), is shown in Figure 7–2. A fit to the distribution is used, where the signal is modeled with a modified hyperbolic secant distribution:

$$S(\theta^2, w) = \frac{1.71N}{2\pi w^2}\mathrm{sech}(\sqrt{\theta^2}/w) \tag{7.1}$$

where w is the width of the distribution and N is the number of signal events. This model was determined empirically and describes the signal distribution well, taking into account the leptokurtic aspect of the distribution [109].

If looking only at events within 1° of the Crab Nebula position, the background is well described by a linear function. Using a linear combination of

Equation 7.1 for the signal with a polynomial of degree one for the background gives the resulting fit that can be seen in Figure 7–2.

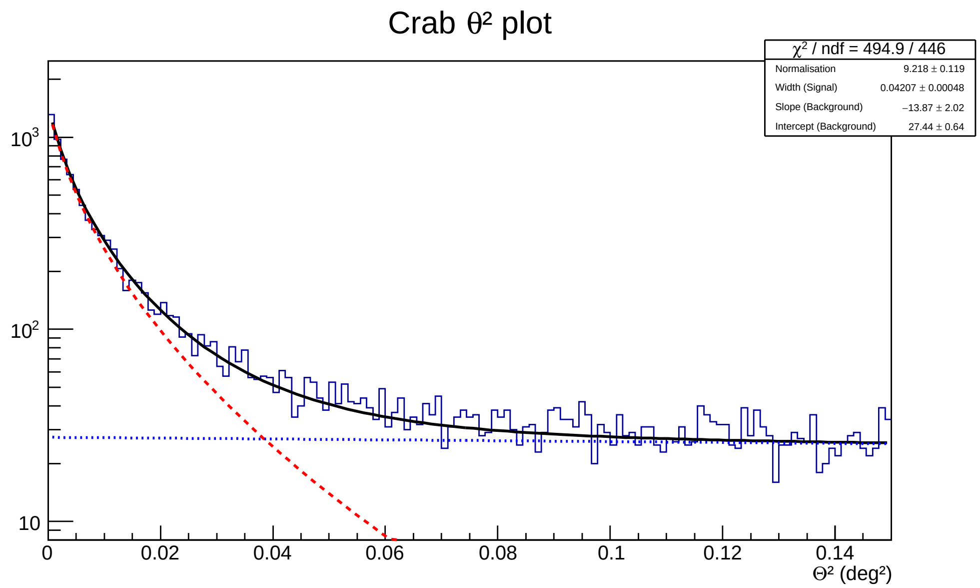

Figure 7–2: θ^2-distribution of all the events from all the V5 Crab runs, from all zenith angles. The black line is the best fit to the data, while the red dashed line is the signal component of the fit, and the blue dotted line is the background component.

The parameter w is what is related to the PSF. In order to get its dependence as a function of energy and elevation, the Crab data set is separated in energy and elevation binning. Because the Crab spectrum is a power-law of index ~ -2.5, the amount of gamma rays at high energies are much lower than at lower energies, so the binning has to be wider at high energies in order to get enough statistics. The energy binning chosen is the same one as the one used for the development of BDTs (see Section 6.5.2), i.e. 0.08 to 0.32 TeV, 0.32 to 0.5 TeV, 0.5 to 1 TeV and 1 to 50 TeV. The last bin is as big by design because of the low statistics at these energies. Similarly, the data will be biased towards higher elevations, so the binning will have to be representative of that as well (50 to 70 degrees in elevation, 70 to 80 degrees, and 80 to 90 degrees).

Figure 7–3 shows the θ^2-distribution for the different binnings. Already, simply by eye, it can be seen that the width of the distribution is getting smaller, the PSF becoming tighter. This is expected as a Cherenkov shower is tighter at higher energies.

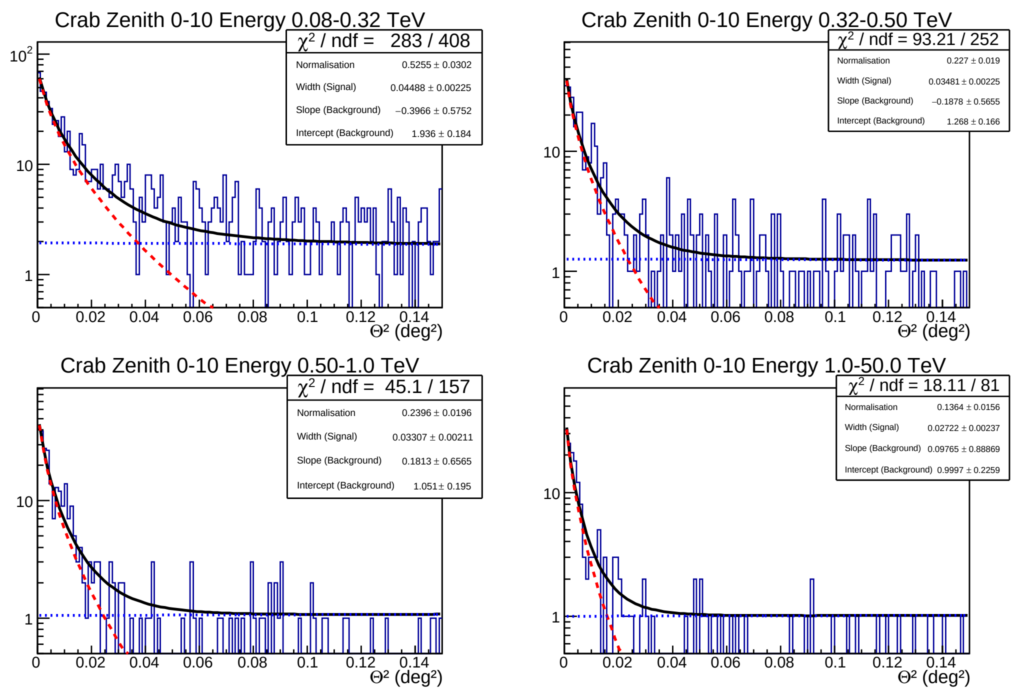

Figure 7–3: θ^2 distribution at different gamma-ray energies (*top left*: 0.08-0.32 GeV, *top right*: 0.32-0.5 GeV, *bottom left*: 0.5-1.0 GeV, *bottom right*: 1.0-50.0 GeV), for the elevation range 80-90 degrees.

Figure 7–4 shows the 68, 80 and 90% containment radii of the PSF from the distributions in Figure 7–3, as a function of energy. The different plots show this for different energies. The evolution in elevation is shown in each plot, and the curve is a fit to the 90% containment radius points, using a linear function. The PSF decreases with increasing elevation. At lower elevation, a shower has more atmosphere to go through, causing increased lateral expansion, resulting in a wider shower when reaching the camera, explaining the behavior seen here.

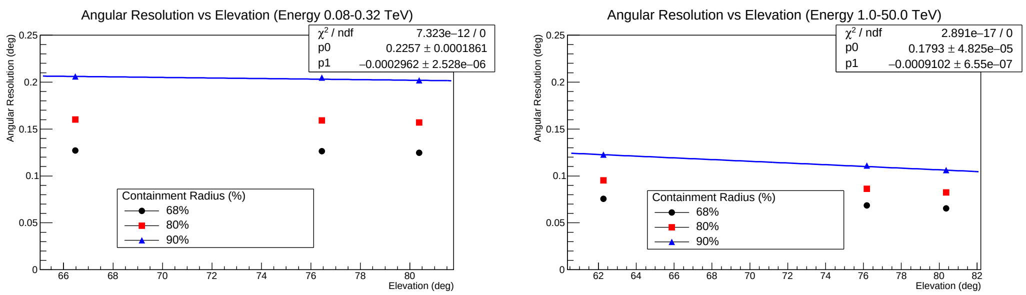

Figure 7–4: Angular resolution as a function of energy and elevation. *Left*: Energy from 8 to 32 GeV *Right*: Energy from 1 TeV to 50 TeV. Each plot shows the angular resolution as a function of elevation. The dependence in elevation is small, but the PSF does decrease with increasing elevation.

7.3.2 Likelihood Method for Angular Cut

Understanding the PSF as a function of energy and elevation is the first step in a cut on localization. The basic idea is to find out what the likelihood is that those events could be coming from the same point in the sky, given a list of events arriving within a given time window, with their respective energy and elevation known.

To do this, a likelihood maximization technique is used. Using Equation 7.1, the likelihood function would become:

$$L = \prod_i \frac{1.71}{\pi w_i^2} \mathrm{sech}(\sqrt{(\theta_i - \mu)^2}/w_i) \tag{7.2}$$

where w_i and θ_i are the angular resolution and direction of event i respectively, the width being given from the event's energy and elevation, determined from the study in the previous section. Since the expression $-2\ln(L)$ behaves like a χ^2 [14], minimizing that expression with respect to μ (which maximizes Equation 7.2) will give the centroid position, expressed by μ_{min}.

This minimization technique is used to find the centroid of any group of events. Figure 7–5 shows a group of 10 events taken randomly from a data run. The centroid position from the likelihood minimization is shown as a blue square.

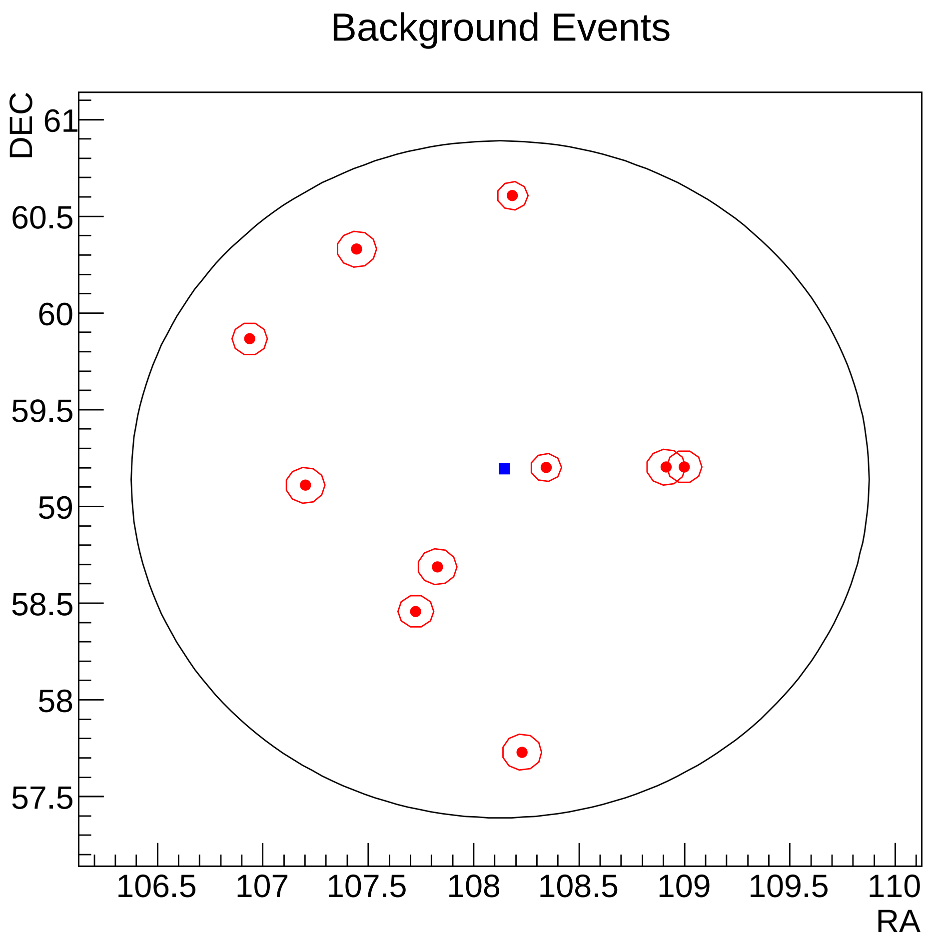

Figure 7–5: Centroid position of a group of random events. The red points show the position of the events, and the circles surrounding each of them correspond to the 68% error on their position. The centroid position is shown as a blue square. The large, black circle, represents the field of view of the array.

It is also important to know what a group of events that do come from the same point in the sky looks like. Since such a behavior occurring in real data is rare (but does happen, as will be shown in the next sections), it is easier to simulate them.

Using the centroid position calculated and shown in Figure 7–5, the 10 events can be repositioned across the field of view according to the hyperbolic secant distribution of Equation 7.1 by scattering them according to their uncertainties. For each event, its energy and arrival elevation are used to get the width parameter of the hyperbolic secant distribution, and that distribution is then used to generate a random radial position with respect to the centroid. A uniform probability distribution is used for the azimuthal angle position with respect to that same centroid. Those newly-distributed events are then used to calculate a new centroid, and this gives a distribution of events as seen in Figure 7–6. As can be seen, the event's positions are much more consistent with each other.

The likelihood-minimization method can then be used to determine what set of events are likely to be coming from the same point in the sky. By looking at random groups of events from data, a distribution of the minimized likelihood ($-2\ln(L)$) is computed for each group. The same is done for the simulated data as outlined previously. Comparing the two distributions shows the differences between random scattering of events (heretofore called "background bursts") and simulated data ("real") bursts. Figure 7–7 shows the two likelihood distributions for "bursts" of 2, 3, 5 and 10 events.

The distribution for the simulated bursts is systematically narrower than for the background bursts, and stays around the same value regardless of the number of events in the burst. This would be expected as the scatter between the events is small by construction, whereas the background events are much more spread out (as exemplified in Figure 7–5). This behavior gives the information about where to set the cut value.

The background distribution is separated from the simulated bursts. The average of the distribution stays constant with the number of events in the

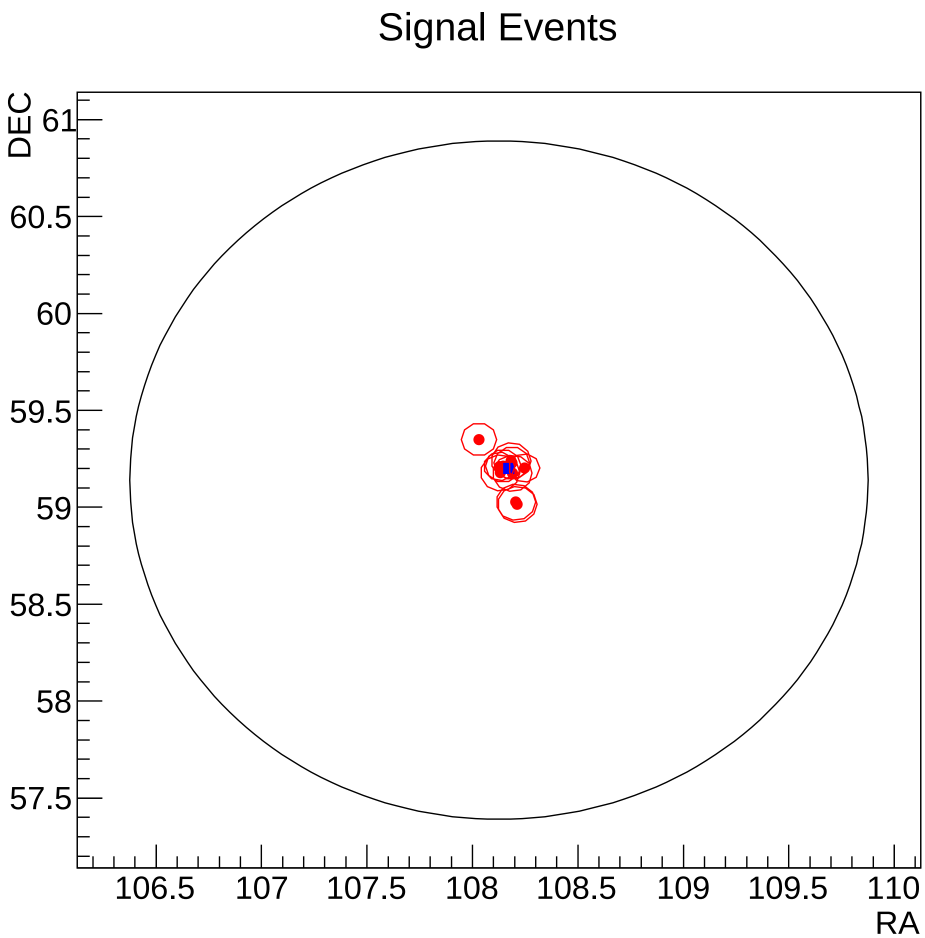

Figure 7–6: Centroid position of a group of events simulated to be coming from the same point in the sky following the probability distribution of a hyperbolic secant (Equation 7.1). The centroid is shown as the blue square. The events shown here have the same energies and elevations as the events in Figure 7–5. The events' new positions are much more consistent with each other.

bursts, but its width decreases. This means that for a burst of two events, more background will be accepted when applying the cut, but almost none for larger burst sizes. However, limiting oneself to the larger bursts will limit the sensitivity of the PBH measurement.

These distributions can be used to determine a proper cut value on the likelihood to discriminate real bursts from background ones. A cut which

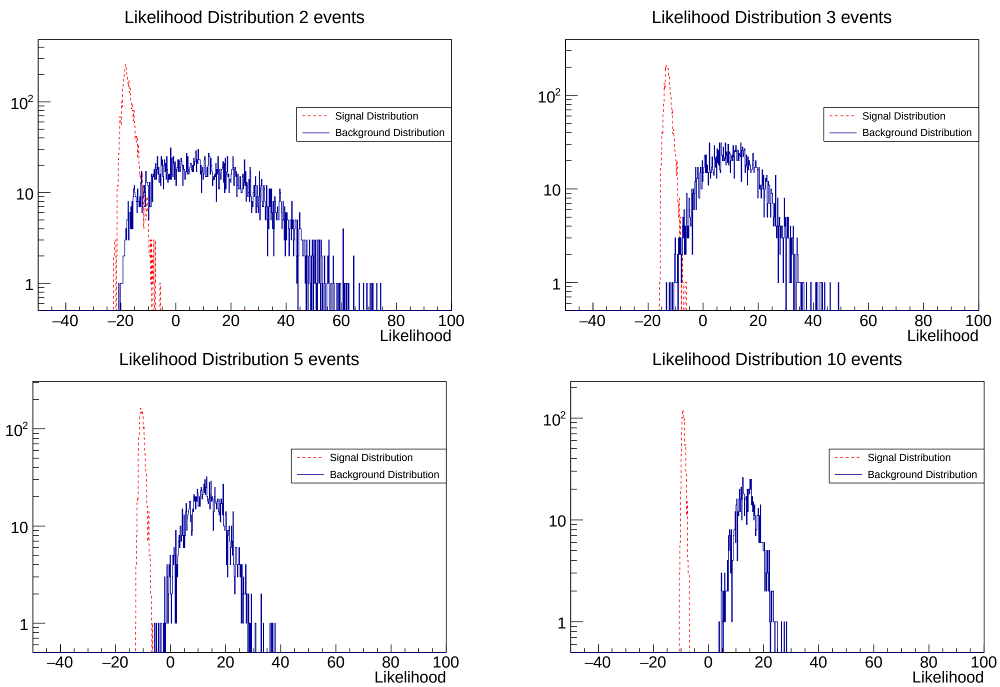

Figure 7–7: Likelihood distribution of random scattering of events (in blue) and of simulated bursts (in red). *Top left*: Likelihood distributions for groups of 2 events. *top right*: for groups of 3 events. *bottom left*: For groups of 5. *bottom right*: For groups of 10.

keeps 90% of the real bursts is used, in order to maximize the amount of real bursts seen and minimize the amount of background ones.

7.4 Burst-Finding Algorithm

The time window and the likelihood cut are integral parts in the search for bursts, but now these need to be used in an algorithm in order to find those bursts.

The following steps are done on individual runs, and the final limits will be computed when putting all those runs together (which will be explained in the next chapter). The individual runs are first analyzed using the standard

VERITAS analysis. In this case, it uses the Boosted Decision Trees (moderate cuts), to compile a list of events. This list is divided into 2 categories, the ones that passed the cuts (gamma-like), and those that did not. This feature is not strictly necessary, but will help when estimating the background, as will be explained in the next section. The selected events are accompanied with the information on their energy, arrival elevation and reconstructed position on the sky. Some ancillary information about the run itself is necessary, like the telescope pointing direction, the effective area curve for that run, and its radial acceptance (the last two are explained in Section 6.7).

For this part of the analysis, only the gamma-like events are necessary. For each event i arriving at a time t_i, a list is compiled with any subsequent event that happens within a window Δt of the first one, i.e. any events between times $[t_i, t_i + \Delta t]$, where Δt is the time window being used for the analysis. For each of these lists, any subgroup where the events are likely to come from the same point in the sky are kept.

The algorithm first looks at all of the events in the time-burst. At first, it removes events that are obviously alone, or singlets, i.e. that they have no neighbors in a radius equals to 5 times their respective 68 % containment radii. Once these are removed, the centroid of the remaining events is calculated, along with the corresponding likelihood. If the likelihood value is less than the cut value (determined in the previous section), then this is considered to be a burst, and the algorithm moves on to the next time-burst. However, if not, the algorithm, inspired by Chauvenet's criterion [110], adapted to the maximum-likelihood technique, will remove the furthest outlier from the list and try again with the remaining events. The furthest outlier is the event that has the maximum $-2\ln L$ value of all the events in the group.

The worst offender is the event that fits the least well with the centroid position. This outlier is then removed, and the algorithm will do the likelihood test with the remaining points.

This is done again with the subgroup, and each time an outlier is removed, it is kept in memory with the previous ones. Then, if the algorithm determines that one of the subgroup is a burst, or eliminates every event until there is only one left, it will proceed to reexamine the outliers. This needs to be done in case another subgroup formed a burst that was ignored in favor of a more obvious one. Figure 7–8 shows an illustration of this algorithm, starting with a time-burst, and eliminating events until a burst is found, and then moving on to the eliminated events to do the same.

To avoid double-counting, each event is assigned the size of a burst (the size of the burst being the number of events within it). Since an event may be present in more than one burst, it is assigned the size of the largest burst. Then, the number of bursts of size b, $N(b)$, is determined by counting the number of events of size b, $N_{ev}(b)$ and dividing by b:

$$N(b) = \frac{N_{ev}(b)}{b} \tag{7.3}$$

Table 7–1 shows a simple example of how the counting method works. That example shows the situation with six events counted in three bursts (1 and 2 being a pair, 3 and 4 another one, and 4, 5 and 6 a triplet). Four is found in two different bursts, and is therefore assigned a size of three, the largest burst in which it is found. Since event four's largest burst is of size three, its pair companion in the smaller burst of size two, three, is left alone. In that case, it becomes a single event, being no longer part of a burst. Table 7–2 gives the final count of bursts from Table 7–1.

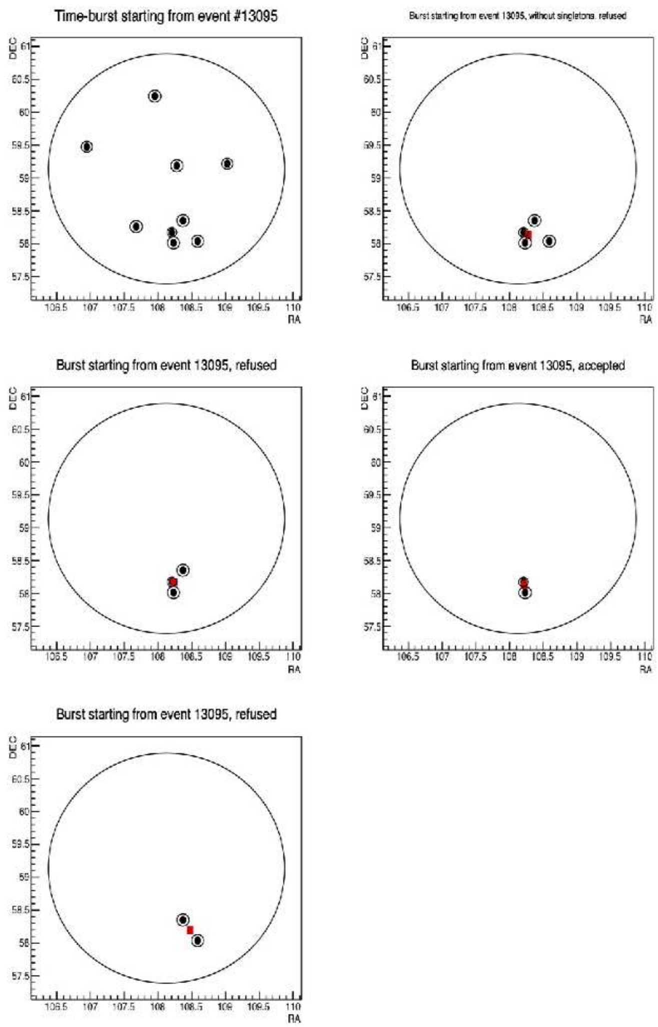

Figure 7–8: Illustration of the burst-finding algorithm. The first plot is the time-burst, showing the event positions as well as their uncertainties. The next one shows the events left after removing the isolated ones. The centroid position is also shown with the red square. This is not accepted as a burst, so the furthest outlier is removed, and the test is done again on the next plot, and eventually reaches a point where a burst is found. The final plot tests the other events that had been discarded along the way, ignoring the singlets that have been removed originally, to see if those could also be a burst.

7.5 Background Estimation Method

As is seen in Figure 7–10, bursts are indeed found in the data. However, it cannot be assumed that they are bursts of gamma rays from PBHs. In fact,

Burst Number	Event Number	Sizes	Final Size
1	1	2	2
1	2	2	2
2	3	2	1
2,3	4	2,3	3
3	5	3	3
3	6	3	3

Table 7–1: Example of the burst-counting methods to avoid double-counting. Imagine there are 6 events contained in multiple bursts. In this case, 1-2, 3-4, and 4-5-6. The Sizes column gives the sizes of the bursts each event is involved in. Event 4 is present in 2 bursts, one of 2 events, and one of 3. It is assigned the maximum size, 3. Since burst 3 is now alone, it is no longer considered as part of a burst.

Burst size	Number of bursts
1	1
2	1
3	1

Table 7–2: Results of the burst count from the example of Table 7–1. Note that a burst of size 1 is simply an isolated event (in this case, event 3 from our example).

most of the gamma-like events in a run are not gamma rays but misidentified cosmic rays. Statistical fluctuations on the background flux can and do lead to fake bursts. It then becomes important to find a way to estimate what the expected amount of background bursts will be.

One way to estimate the background is by scrambling the arrival time of the events and redoing the analysis. Each event will then keep its arrival direction, energy and other information, but its time of arrival will switch with another random event. This has the effect of removing any fake bursts and creating new ones, but also to break apart potential real bursts which will not be compensated for in the background estimation and will therefore stand out.

This will work if using the original list of gamma-like events that survived the cuts. It will find the same time-bursts, but not the same bursts in space. However, if one wants to get randomized time-bursts as well, it is also possible to scramble the times of all events that were reconstructed before the cuts were applied, and then select the gamma-like events. Figure 7–9 illustrates the time-scrambling background estimation method.

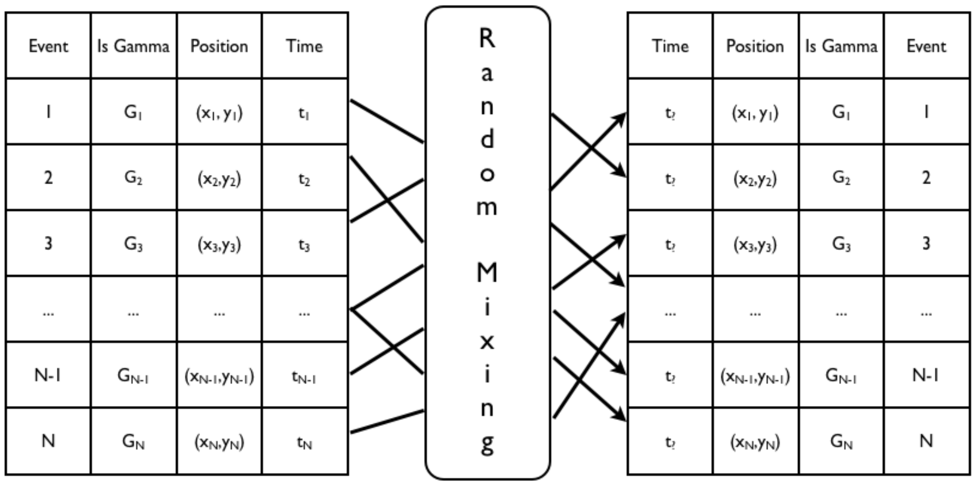

Figure 7–9: Illustration of the time-scrambling background estimation method, in order to reconstruct the amount of bursts due entirely to statistical fluctuations. From the leftmost column is the event number, followed by the flag that identifies the event as gamma-like or not, its position, and its time. The mixing results in the right table, where the times are scrambled, but everything else remains the same.

This method presents the advantage of already taking into account instrumental effects of the given run, like weather or instrumental situations specific to the run. For example, if the field that the telescopes were pointing at at the time had a bright star that required to shut down a given PMT for the duration of the run in order to protect it, this effect will carry over to the background estimation. Moreover, the anisotropies in the cosmic ray background would affect the amount of bursts seen, which will be reflected in both the data and the background. Finally, this method is also able to take into account the presence of a stable source, as its rate of gamma rays will also be seen in the background. For a given run, in the final analysis, this background estimation method is repeated 10 times and averaged. This is then compared with the analyzed data, in order to find whether or not there is a significant excess of bursts. Figure 7–10 shows an example for a given run, using scrambled data. In this instance, the background has been computed 30 times and averaged.

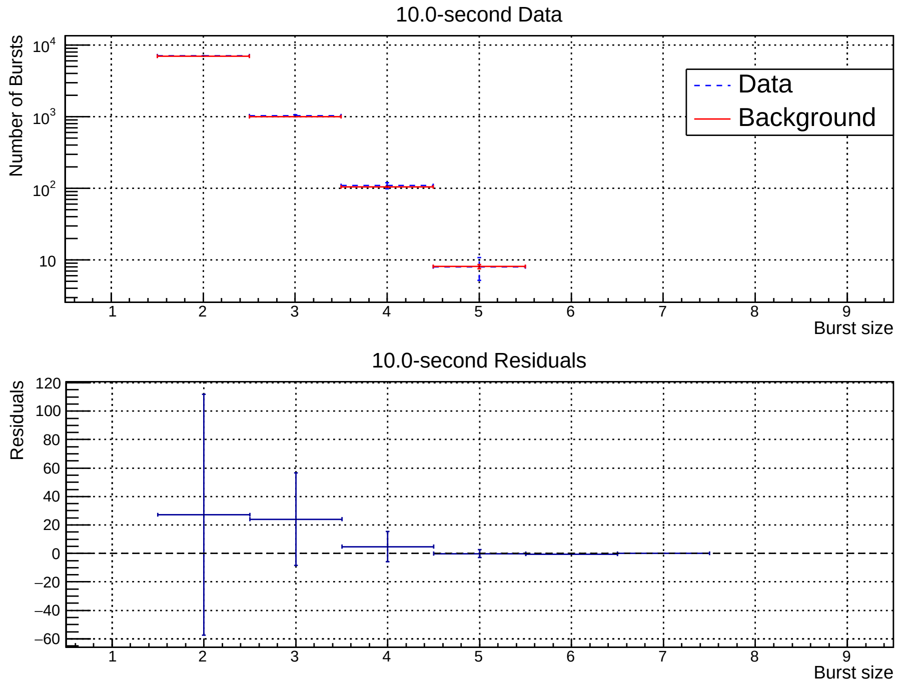

Figure 7–10: Distribution of gamma-like events' bursts as a function of burst size for a time window of 10 seconds. The blue dashed lines are from scrambled data, and black lines are the background from 30 other scrambles, averaged. The residuals between the two is shown in the bottom plot. The errors on the data come from Poisson statistics.

CHAPTER 8
Results and their Interpretation

Now that every step of the analysis has been explained in the previous chapters, the results of the analysis need to be looked at. The analysis will give a distribution of bursts as a function of the burst size (the number of events in a given burst), but that in itself does not necessarily reveal anything beyond an excess of bursts present in the data. However, is the burst coming from a Primordial Black Hole (PBH) evaporation, or some other phenomenon? Since this work concentrates on the search for PBHs, the results will be interpreted according to the PBH model. In other words, the burst of gamma rays found (or lack thereof) will be given a physical interpretation with regards to the rate-density of PBH evaporation.

8.1 Comparing Data and Background

The previous chapter focused on explaining the analysis to get a distribution of bursts. Since this analysis looked at different time windows, it is important to get a sense of the burst-distribution behavior with an increasing time window. In order to investigate this without incurring a trials factor in the final limit, the search is done on a subset of the data used, all time-scrambled. In that way, the real data is never looked at, and the analysis can be fine-tuned. Final results, using the real data will be shown in Section 8.2.

Figures 8–1 and 8–2 show the distribution of bursts for time windows of 10 and 100 seconds. The plots are much like what was shown in Figure 7–10, the blue dashed lines being the fake data, which is made using a random-scrambling of the data. The black lines represent an estimate of the background, using 30 random scrambles of data, averaged. For these plots, 60 runs were used, for a total time of 18 hours. This analysis was also performed for time windows of 1, 2, 5, 30, 45, 60 and 80 seconds.

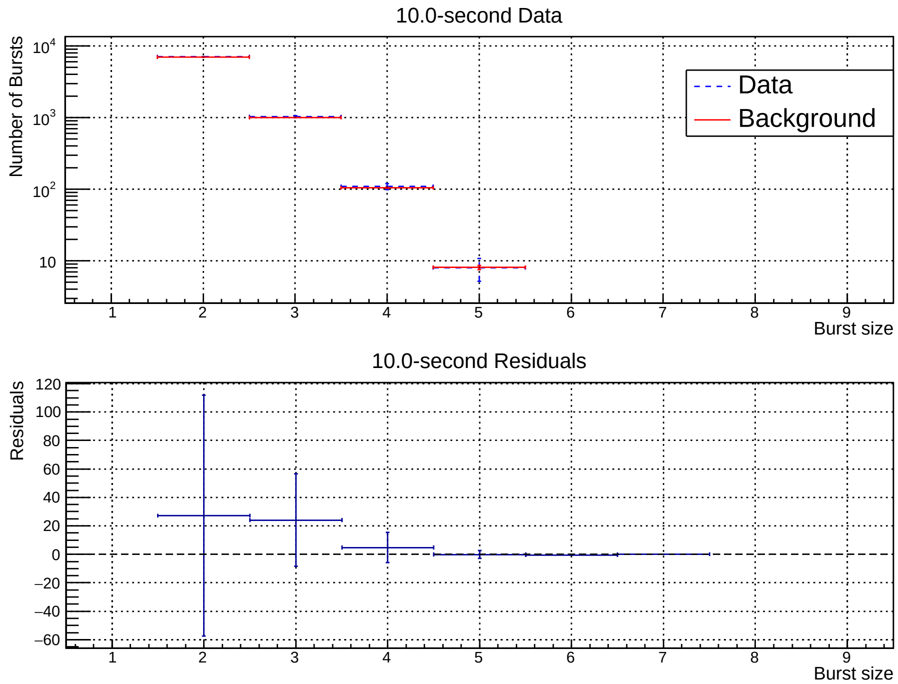

Figure 8–1: Burst distributions for random data using a time window of 10 seconds. The residuals plot shows the difference between the fake data count and the background.

It is interesting to note that as the time window is increased, the distributions evolve from an exponential behavior (as shown in Figure 8–1), to introducing a certain curvature in the low burst-sizes (with the distribution shown in Figure 8–2). This will be discussed further in Section 8.2.2.

8.2 Deriving Limits

8.2.1 Models of the Expected Number of Bursts

To get an upper limit on the rate-density of PBH evaporation, the expected number of gamma-ray bursts coming from PBHs' final evaporation

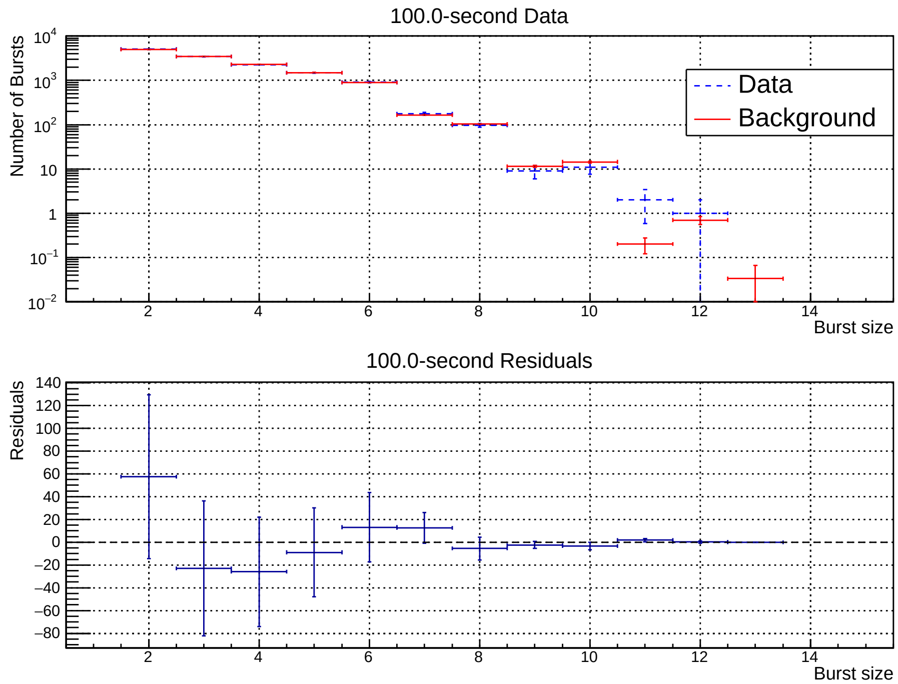

Figure 8–2: Burst distributions on random data for time windows of 100 seconds. The residuals plot shows the difference between the fake data count and the background.

must be calculated. This can be derived from the model used to predict the emissions from a PBH's final evaporation. This model was detailed in Section 4.2.1, with the resulting spectrum of VHE gamma ray expressed in Equation 4.31, shown again here for convenience:

$$\frac{dN_\gamma}{dE_\gamma} \approx 9 \times 10^{35} \times \begin{cases} \left(\frac{1\mathrm{GeV}}{T_\tau}\right)^{3/2} \left(\frac{1\mathrm{GeV}}{E_\gamma}\right)^{3/2} \ \mathrm{GeV}^{-1} & \text{for } E_\gamma < kT_\tau \\ \left(\frac{1\mathrm{GeV}}{E_\gamma}\right)^{3} \ \mathrm{GeV}^{-1} & \text{for } E_\gamma \geq kT_\tau \end{cases} \tag{8.1}$$

where T_τ is the temperature of the black hole at the beginning of the final burst interval, $T_\tau = T_{BH}(\tau)$:

$$kT_{BH}(\tau) = 7.8 \left(\frac{\tau}{1\mathrm{s}}\right)^{-1/3} \ \mathrm{TeV} \tag{8.2}$$

and τ is the remaining PBH lifetime. When the analysis is looking at bursts in a time window of 10 seconds, it is compared to the expected spectrum of Equation 8.1, using a remaining lifetime of 10 seconds. To get an idea of how many bursts would be seen by VERITAS, the amount of photons that can be detected from a PBH at a distance r from the telescopes is given by:

$$N_\gamma(r, \alpha, \delta, \Delta t) \;=\; \frac{1}{4\pi r^2} \int_0^\infty \frac{dN}{dE}(E_\gamma, \Delta t) A(E_\gamma, \theta_z, \theta_w, \mu, \alpha, \delta) dE_\gamma \tag{8.3}$$

where $dN/dE(E_\gamma, \Delta t)$ is given by Equation 8.1, and $A(E_\gamma, \theta_z, \theta_d, \mu, \alpha, \delta)$ is a combination of the Instrument Response Functions (IRFs) of VERITAS, as a function of the gamma-ray energy E_γ, the observation zenith angle θ_z, the wobble offset θ_w, the optical efficiency μ, and the event reconstruction position in camera coordinates (α, δ). This expression can be split onto two components, one depending only on the camera coordinates, and the other depending on $E_\gamma, \theta_z, \theta_w$, and μ:

$$A(E_\gamma, \alpha, \delta) \;=\; g(\alpha, \delta) \times a(E_\gamma, \theta_z, \theta_w, \mu) \tag{8.4}$$

$g(\alpha, \delta)$ corresponds to the radial acceptance of the camera, while the second term is the effective area of the telescopes. These IRFs are quickly described in Section 6.7.

The convolution of the expected spectrum from PBH evaporation and the IRFs gives the expected number of photons emitted by a PBH that should be seen by the detector at a distance r from the PBH, N_γ.

Since this analysis is interested in bursts of gamma rays from PBH evaporation, N_γ should be used to get a probability of catching a burst of size b given N_γ. This is expressed as a Poisson probability:

$$P(b, N_\gamma(r, \alpha, \delta, \Delta t)) \;=\; \exp(-N_\gamma)\frac{N_\gamma^b}{b!} \tag{8.5}$$

This expression can be used to determine an *effective* volume V_{eff}, describing a volume to which VERITAS is sensitive to the evaporation of a PBH:

$$V_{eff}(b, \Delta t) \;=\; \int_{\Delta\Omega} d\Omega \int_0^\infty dr r^2 P(b, N_\gamma(r, \alpha, \delta, \Delta t)) \tag{8.6}$$

where $\Delta\Omega$ is the solid angle covered by the VERITAS telescopes. This integral can be solved to give:

$$V_{eff}(b, \Delta t) \;=\; \frac{1}{8\sqrt{\pi}}\frac{\Gamma(b-3/2)}{b!}I^{3/2}\int_{-1}^{1}(g(\alpha, \delta))^{3/2} d\cos\theta \tag{8.7}$$

where I is the convolution integral of Equation 8.3, with the radial acceptance taken out and dealt with independently (the integral on $g(\alpha, \delta)$).

In a given data run, the expected number of bursts n_{exp} of size b for a time window Δt can then be expressed as:

$$n_{exp}(b, \Delta t) \;=\; \dot{\rho}_{PBH} \times T_{obs} \times V_{eff}(b, \Delta t) \tag{8.8}$$

where $\dot{\rho}_{PBH}$ is the rate-density of PBH evaporation, and T_{obs} is the deadtime-corrected duration of the run.

For the whole data set, the total expected number n_{exp}^{tot} is expressed as such:

$$n_{exp}^{tot}(b, \Delta t) \;=\; \dot{\rho}_{PBH} \times \sum_j T_{obs,j} \times V_{eff,j}(b, \Delta t) \tag{8.9}$$

where j goes over each run used in the analysis. Figure 8–3 shows the effective volume of an example run, as a function of burst size and time windows. As would be expected, the volume decreases as a function of burst size. Distant

PBHs will appear to be dimmer due to the $1/r^2$ fall-off, so requiring fewer gamma rays in a burst means one can see PBHs that are further away.

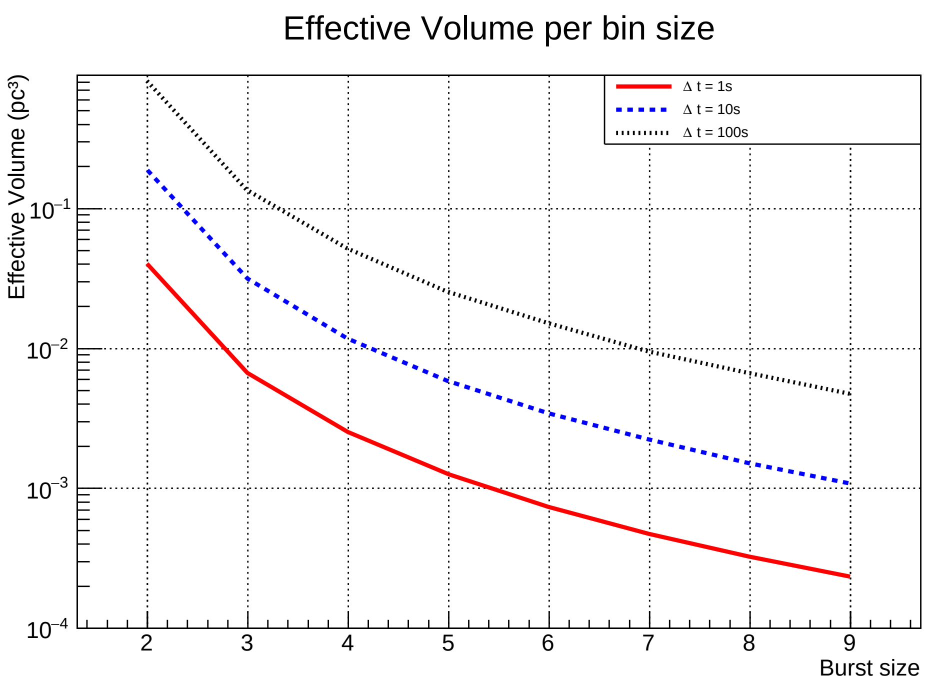

Figure 8–3: Evolution of the effective volume as a function of burst size and time window. Shown here are time windows of 1, 10 and 100 seconds.

The total effective volume $V_{eff}^{tot}(b, \Delta t)$, when combining all runs, is expressed here:

$$V_{eff}^{tot}(b, \Delta t) \;=\; \frac{\sum_j T_{obs,j} \times V_{eff,j}(b, \Delta t)}{\sum_j T_{obs,j}} \tag{8.10}$$

Note that the volume is always less than 1 pc^3, hence the rate-density of PBH evaporation found in this work (or the limit) is considered to be local. In essence, the measurement done here gives the rate-density of PBH evaporation in a very local neighborhood. This may not be representative of the overall average rate-density of PBHs across the universe, depending on how they may have clustered through its evolution. This will be explored further in Section 8.5.

8.2.2 Maximum Likelihood and Limits

With the information on the number of bursts seen in data and background, the method of maximum-likelihood can be used. The likelihood equation is expressed as such:

$$L(\dot{\rho}_{PBH}) = \prod_{b} f(n_b|\dot{\rho}_{PBH}) \tag{8.11}$$

where $f(n_b|\dot{\rho}_{PBH})$ is the likelihood function, or probability law with parameter n_b, the number of bursts seen in the data, given the rate-density of PBH evaporation $\dot{\rho}_{PBH}$ in Equation 8.8. The multiplication is done over each burst size b. The assumption is that those laws follow Poisson statistics:

$$f(n_b|\dot{\rho}_{PBH}) = \exp\left[-\left(n_{bg} + n_{excess}\right)\right] \times \left(n_{bg} + n_{excess}\right)^{n_b} / n_b! \tag{8.12}$$

which is the probability of seeing n_b bursts given a rate-density $\dot{\rho}_{PBH}$. In this, n_{bg} is the number of bursts seen in the background, n_{excess} is the excess number of bursts between data and background, and n_b is the number of bursts seen in the data. Constraining n_{excess} across each burst size will constrain the rate-density $\dot{\rho}_{PBH}$.

For each burst size b, the number n_{bg}, n_{excess} and n_b come from their respective values for b. $n_{excess}(b)$ is used to calculate $\dot{\rho}_{PBH}$ from Equation 8.8. In the maximum-likelihood technique, Equation 8.11 must first be maximized, and the upper limit will be given when the ratio between a rate-density and the maximum corresponds to the desired confidence level.

Since it is easier to use the logarithm of the likelihood equation (the multiplication becomes a sum, and the exponentials are eliminated), the test is done using the following equation:

$$-2\ln L \;=\; -2\sum_{b} n_b \ln(n_{excess} + n_{bg}) - n_{excess} \tag{8.13}$$

where all the terms from Equation 8.12 that do not depend on n_{excess} can be neglected, since they simply add a constant offset to the equation, that will cancel out when using the maximum-likelihood technique.

Because of the change of signs, the maximum-likelihood technique requires Equation 8.13 to be minimized in order to maximize Equation 8.11, and it is the difference between the minimum and the value of a given rate-density of PBH evaporation that will be used to set an upper limit:

$$-2\Delta\ln L \;\leq\; 6.63 \tag{8.14}$$

where $\Delta\ln L \;=\; \ln L(n_b|\dot{\rho}_{PBH}) - \ln L_{min}$, and the value of 6.63 is the condition for a 99% CL [14].

As was discussed af the end of Section 8.1, the burst distributions are exponential for small time windows (like in Figure 8–1) or large burst sizes (like in Figure 8–2). For large time windows and small burst sizes, they deviate from an exponential behavior and have a curvature at the low end (see Figure 8–2). This is because small bursts get merged into bigger bursts, which are more common due to the larger time windows since they let in more background.

This indicates that a cut on the minimum burst size is necessary. This is determined so that the range of burst sizes used is in the exponential region. The minimum burst size is then chosen so that for a given bin, the number of bursts N_{bin} must be $\gg N_{bin+1}$. Hence, the burst-size threshold is used to determine a burst-size range where the number of bursts in the subsequent bins are no more than 75% of the value at N_{bin}.

Figure 8–4 shows the limits on the rate-density of PBH evaporation from the scrambled data sets for time windows of 1, 2, 5, 10, 30, 45, 60, 80 and 100

Δt	Burst-size Threshold
1	2
2	2
5	2
10	2
30	2
45	3
60	4
80	5
100	6

Table 8–1: Burst-size threshold determined for each time window, used for the example shown in Figure 8–4.

seconds (see Figures 8–1 and 8–2 for the burst-size distribution of the 10 and 100-seconds time windows). For this scrambled data, the burst-size threshold were determined from the above criteria, and the values are shown in Table 8–1.

The purpose of the test described here is to get an idea of the uncertainties on the limits, and of which time windows will be the most sensitive for the final analysis. This is done by computing the limits multiple times, and looking at the scatter. Since the data were scrambled 30 times, each limit calculation used one of the scrambled data as data and 4 others, averaged, as a background estimate. This is repeated 6 times, so that each random scrambling is used once. The points in Figure 8–4 show the average limits and the RMS/$\sqrt{6}$ from those measurements. In this way, the sensitivity of the measurement is shown, as well as the potential variations

These results indicate what time windows are best to use for the PBH search on the real data. Since the minimum limit is measured around a time window of 30 seconds, the final analysis will look at time windows up to 45 seconds. This also saves precious computing time, as analyzing the burst distributions of a run for a 30-second time window takes approximately 30

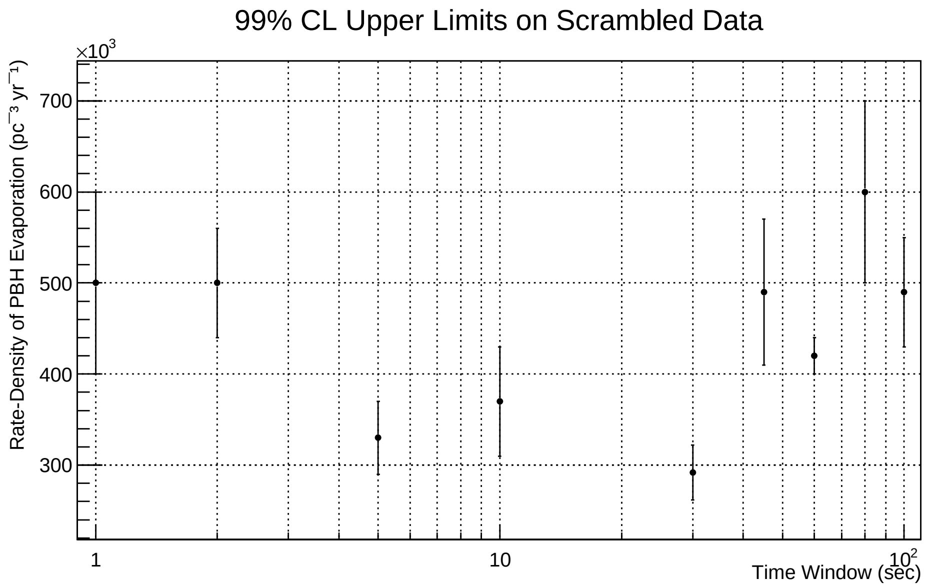

Figure 8–4: Upper limits on the rate-density of PBH evaporation, on the scrambled data set. A random scrambled data set is used as data, and another 4 are used as a background estimate. This is repeated 6 times. The uncertainties represent the RMS/$\sqrt{6}$ of those measurements.

minutes to a couple of hours (depending on the number of gamma-like events), while the 100-second time window can take up to one day to process. Also, recalling Figure 4–8, it can be seen that expanding the time windows beyond approximately 30 seconds does not give many more photons, beyond having access to a larger effective volume, so the signal-to-background ratio decreases.

8.3 Final Limits

Now equipped with all this information from randomized data, the actual data can finally be analyzed. Figures 8–5 and 8–6 shows the burst distribution for the 1 and 30-second time windows. The 1-second window is shown here, despite not being the most sensitive window, as this is the window that previous measurements from VERITAS, H.E.S.S. and Whipple used to report their limits. The distribution from the 30-second window is also shown, as it obtains the most-constraining limits. The other time windows (2, 5, 10 and 45) have also been analyzed but are not shown here.

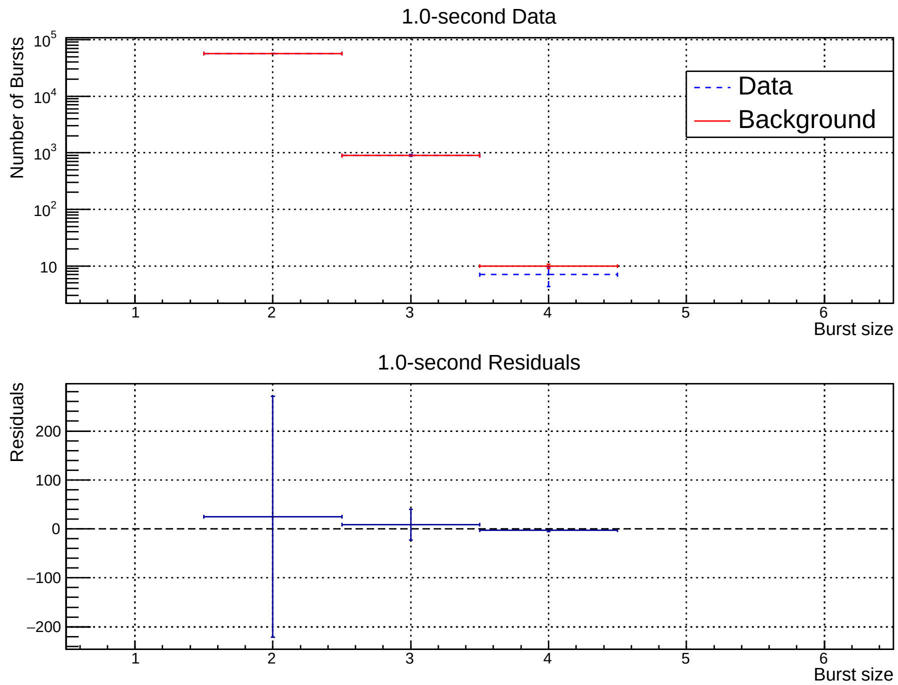

Figure 8–5: Burst distributions for a time window of 1 second.

These are then used in the maximum-likelihood calculation of Equations 8.11 to Equation 8.14 to calculate the resulting limits, taking into account the burst-size threshold of the longer time windows. Figure 8–7 shows examples of the maximum-likelihood curves, with the line at 6.63 to indicate the 99% CL, for time windows of 1, 10 and 30 seconds.

Figure 8–8 shows the final limits obtained for each time windows, compared with the results of the previous searches that have been outlined in this thesis, in Section 4.4.

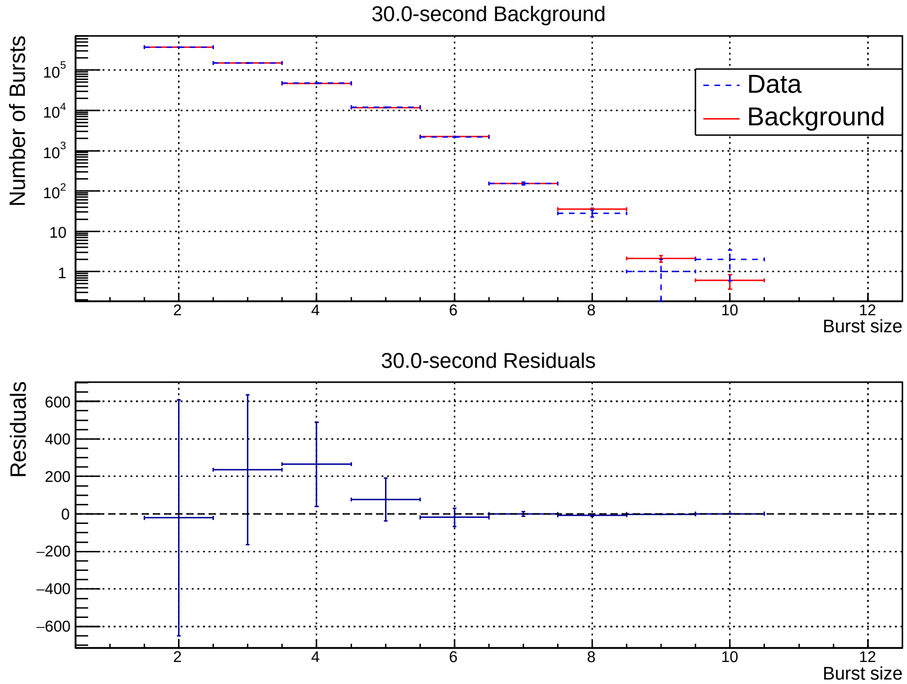

Figure 8–6: Burst distributions for a time window of 30 seconds.

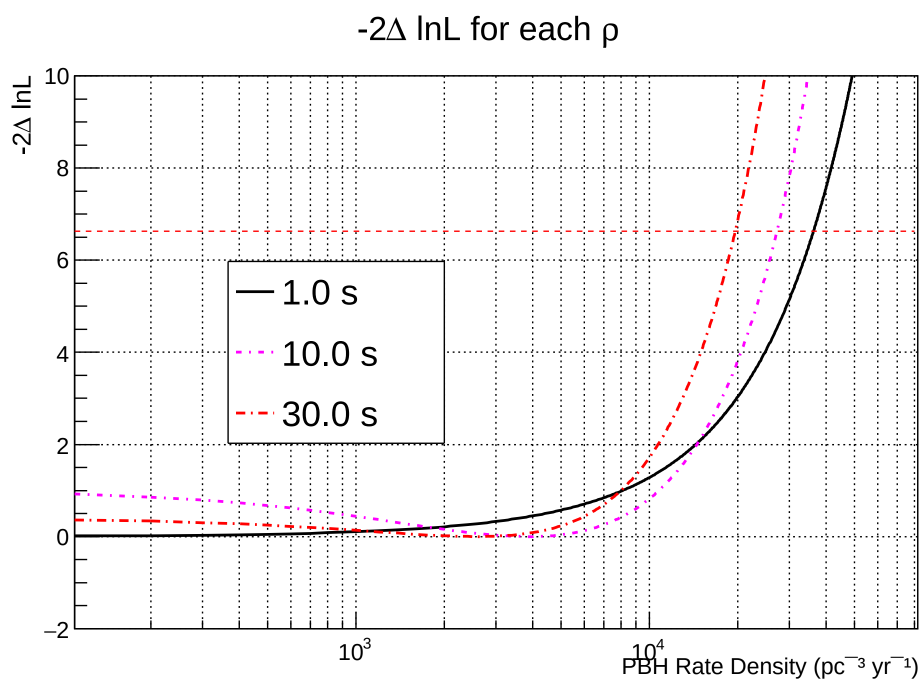

Figure 8–7: Comparison of the likelihood curves on the analyzed data for time windows of 1, 10 and 30 seconds.

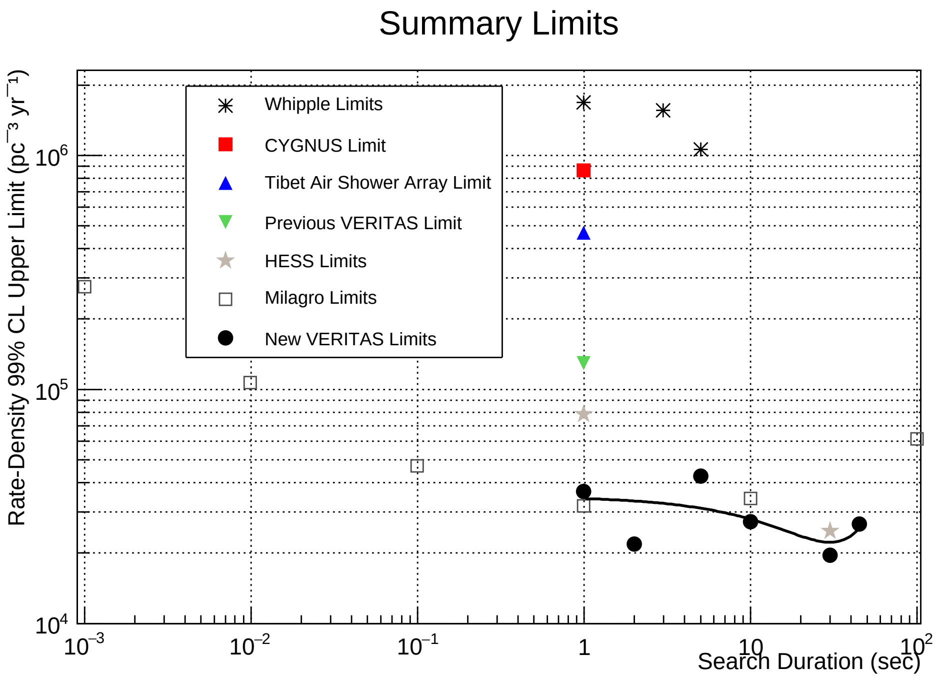

Figure 8–8: Comparison of the limits obtained in this work with previous limits, from the experiments outlined in Section 4.4. Of note are the limits from Whipple [80], the previous VERITAS results [88], and the Milagro limits[70]. The black line is a second-order fit to the limits obtained in this work.

8.4 Comparison with Previous Results

These limits were obtained from a limited set of data. The ultimate goal of this thesis is not necessarily to obtain the new best limits in the field, but to provide a feasibility study for analysing the complete VERITAS data set using new techniques. In order to improve limits, all of the VERITAS data should be used, from each of the different telescope configurations (V4, V5, V6). The behavior of the PSF under each configuration then needs to be understood, and possibly at lower elevation angles to increase the data set even further.

The data set used here comprises 747 hours of data (after deadtime correction). The scatter between the different time windows is likely due to statistical fluctuations in the data and the background. No statistical errors are shown here, as this is not customary when showing upper limits. Referring back to Figure 8–4 gives a sense of the amount of scatter involved in calculating these limits. The uncertainties from Figure 8–4 were obtained by taking the average of 10 scrambled background analyses. One can then expect a smooth curve to be fit to the points, and take its minimum as a final fair limit.

Figure 8–8 shows a second-order polynomial fit to the data, and gives a minimum at 30 seconds, with a value of 2.22×10^4 pc^{-3} yr^{-1}. With a 1-second time window, the fit gets a limit of 3.42×10^4 pc^{-3} yr^{-1}, a factor of 4 more constraining than the previous VERITAS analysis, which had a limit of 1.29×10^5 pc^{-3} yr^{-1} in [88], using 700 hours of data. Since each time window tests a different hypothesis (i.e. each time window tests a different spectrum of PBH evaporation, corresponding to the time window in question), no trials factor penalty is incurred when calculating these limits. The best limit, however, is found at a time window of 30 seconds, and improve the limits by another factor of 1.5, for a value of 2.22×10^4 pc^{-3} yr^{-1}. Prior to this work, the current best limits have been established by Milagro [70], with a time window of 1 second at a rate-density of 3.6×10^4 pc^{-3} yr^{-1}. The limits established by this work improve on that as well, by a factor of 1.5. Figure 8–8 shows the current results in relation to the different experiments. It is expected that after five years of accumulating data, HAWC will be able to reach a limit of 4.06×10^3 pc^{-3} yr^{-1} [70], improving on the measurement in this work even further.

The limits reported here were obtained using only 747 hours of data. Assuming that the background levels remain the same throughout the different configurations, a rough estimate of the limits can be given by scaling to a much larger data set ($\sim$ 4000 hours). A simple method to do this is to use the burst distributions to get a rate for each burst size, and scaling it to the new amount of time. One also needs to adjust the time in Equation 8.9. This gives an estimate of around 7×10^3 pc^{-3} yr^{-1}.

8.5 Discussion

As was briefly explained in Section 3.4.2, the density of current PBHs can constrain the relic density of PBHs, Ω_{PBH}. However, the measurement done here gives the rate-density of PBH evaporation. Therefore, this limit must be converted into a measurement of the relic density. Since the current measurement gives a *local* rate-density, another conversion needs to be done to get the relic density, determined from the average density over the entire universe. This conversion is possible, but a few assumptions have to be made.

The first assumption concerns the initial mass spectrum of PBHs. Since PBHs finishing their evaporation today all had the same mass at formation, the assumed mass spectrum could influence the number of PBHs at these masses. However, observing a certain number of PBHs of a given mass gives little information about the actual initial mass spectrum of PBHs. We can then make an assumption about the mass spectrum, which will only weakly affect the results on the rate-density measurement of PBHs [111]. Assuming that the amplitude of primordial density fluctuations is independent of mass, the mass spectrum would follow (see Section 3.4.1):

$$\frac{dn}{dM_f} = AM^{-\nu} \tag{8.15}$$

where A is a proportionality constant and ν is determined by the equation of state as follows:

$$\nu = \frac{1+3w}{1+w} + 1 \tag{8.16}$$

where $w = 1/3$ for a radiation dominated universe, for PBHs formed in that epoch, which gives ν=5/2.

Using this mass distribution, one can integrate over the number of PBHs that will evaporate within a time Δt at the present time, to get the rate-density of PBH final evaporation:

$$R = \frac{\xi}{\Delta t}\left(\frac{at_f}{at_0}\right)^3 A \int_{M_f(t_0)}^{M_f(t_0+\Delta t)} M^{-\nu} dM \tag{8.17}$$

where $a(t_f)$ and $a(t_0)$ are the scale factor of the universe at the time when the PBHs formed, and today, respectively. $M_f(t)$ is the formation mass of a PBH evaporating at time t. For a PBH evaporating at this epoch, $M_f(t_0)$ is 5×10^{14}g. The parameter ξ is the ratio of the local PBH density to the average one, necessary since, as mentioned previously, the measurement done here gives a local limit. This parameter presents the greatest theoretical uncertainty; it can be as low as 8×10^5 if PBHs cluster following dark matter distributions [112], or as high as 10^{22} if PBHs were initially strongly clustered when formed [113].

Since Δt is much smaller than the total PBH lifetime, the final rate, to first order, will be:

$$R = \xi\left(\frac{a(t_f)}{a(t_0)}\right)^3 A\frac{\alpha_f}{M_f(t_0)^{\nu+2}} \tag{8.18}$$

where α_f is defined as $\alpha(M_f(t_0))$.

This can be compared to the calculation of the relic density of PBH, Ω_{PBH}. An assumption is made that the present mass of all PBHs that had an initial mass greater than $M_f(t_0)$ to be the same as their initial mass. Since the

PBH evaporation is roughly slow and constant through most of its lifetime, and increases exponentially towards the very end, this can be justified. Using the criticial density of the universe ρ_c:

$$\Omega_{PBH} \ = \ \frac{1}{\rho_c}\left(\frac{a(t_f)}{a(t_0)}\right)^3 \int_{M_f(t_0)}^{\infty} AM^{1-\nu}dM \qquad (8.19)$$

the rate R can then be directly related to the relic density:

$$R \ = \ \frac{(\nu-2)\rho_c\alpha_f\xi}{M_f(t_0)^4}\Omega_{PBH} \qquad (8.20)$$

Converting, for example, current results on the relic density of PBHs $\Omega_{PBH} < 10^{-9}$[114], the conversion can be anywhere between 10^{-2} pc^{-3} s^{-1} to 10^{14} pc^{-3} s^{-1}. This is due to the uncertainty on ξ, which makes it difficult to reasonably compare these limits. However, if a PBH search like the one outlined in this work were to succeed in detecting PBH evaporation, this could be combined with the relic density limits, to get a measurement of ξ, the ratio of the local density of PBHs to the average density throughout the universe.

8.6 Conclusion

The results of the measurement have been outlined here. Using a maximum-likelihood technique, the data and background were used to get a 99% CL upper limit on the rate-density evaporation of PBHs. The best limit was found at a time window of 30 seconds, at a value of 2.22×10^4 pc^{-3} yr^{-1}. These are the best current limits. VERITAS, using its whole data set, can potentially reach limits a factor of 3 better, at 7×10^3 pc^{-3} yr^{-1}.

The HAWC experiment claims to be able to reach limits improved by a factor of 4 over the next 5 years [70]. These limits can be used to compare with the limits on the relic density of PBH evaporation, in the hopes of understanding the distribution and clustering of PBHs.

CHAPTER 9
Conclusion

New limits on the rate-density of primordial black hole (PBH) evaporation have been derived in this work. The best limits found here use a time window of 30 seconds, for a 99% CL rate-density of PBH evaporation upper limit of 2.22×10^4 pc^{-3} yr^{-1}. These are a factor 6 more constraining than the previous limit established by VERITAS (1.29×10^5 pc^{-3} yr^{-1}). The limits obtained in this work used 747 hours of data, and the previous VERITAS results used 700 hours. Considering the fact that the amount of data is similar, this improvement is largely obtained thanks to the use of boosted decision trees (BDTs) and the increased sensitivity from a larger time window.

This thesis is meant as a feasibility study of a search using the newly-developed analysis technique from VERITAS. An obvious technique used in this thesis is the boosted decision trees (BDTs), which indeed show a marked improvement on the results, from a similar dataset. Other improvements include the exploration of other time windows, to maximize sensitivity. This work obtained its best limits with a time window of 30 seconds. Using a 1-second window, the limits are 3.42×10^4 pc^{-3} yr^{-1}, a factor of 4 improvement over the previous VERITAS limits.

This work also explored a different treatment of the VERITAS angular resolution, studying its dependence with the energy of the gamma ray, as well as with the pointing direction of the telescope. This step does not necessarily contribute to improve limits, but ensures to properly assess the likelihood of events to be coming from the same point in the sky. Past IACT searches always assumed a fixed angular resolution, which is not the optimal search method.

This work, then, concludes that the new analysis techniques and methodologies work well. As the VERITAS experiment is progressively winding down, it is important to use and improve such analysis techniques to be able to get the most out of its existing data. Using all of VERITAS's data (4000 hours) could potentially make VERITAS reach upper limits of $\approx 7 \times 10^3$ pc^{-3} yr^{-1}, taking into account that the experiment is background-limited. In order to reach this result, further work needs to be done. Using data from the different detector configuration will be necessary. This implies studying the angular resolution of VERITAS under each configuration and possibly large elevation ranges.

The next generation of IACTs, the Cherenkov Telescope Array (CTA), could help improve on those limits even further. It will be capable of detecting VHE sources of 2% of the Crab Nebula flux in ≈ 30 minutes [115], as opposed to the few hours it would take with VERITAS, which would lead to, roughly, a factor of 3 improvement on the current limits if using a similar amount of data from CTA.

The HAWC experiment, recently online, claims to be able to reach limits, within the next five years, of 4.06×10^3 pc^{-3} yr^{-1} [70].

Appendix A
Reflectivity Measurements

This appendix gives a summary of another project that I have worked on extensively during my PhD studies, namely the measurement of the whole-dish reflectivity of VERITAS.

As was explained in Chapter 6, the amount of Cherenkov light seen by the PMTs is used to reconstruct the energy of the gamma ray that induced the shower. It is therefore important to know how much light is lost when being reflected by the mirrors. An apparatus was built to easily take a measurement of the whole-dish reflectivity, an idea first pioneered by the MAGIC collaboration [116] and reproduced with VERITAS. Another method to measure the individual mirror facets' reflectivity is also being used by VERITAS [117], however, it does not take into account the effects of shadowing from the structure of the telescopes (like the quad arms or the PMT camera) on the mirrors, or the difference in the measurement method; the individual mirror facet's measurement gives the specular reflectivity as opposed to the diffuse component from the method described here.

The newly-developed method, described here, uses an astronomical camera (SBIG (Santa Barbare Instrument Group) ST-402ME) with an integrated filter wheel. The filters used are the CFW-402 RGBC from SBIG, comprising 3 bandpass filters (red, green and blue) and a simple transparent window. The camera is installed inside a weatherproof PELCO camera box, along with a motherboard-CPU combo (ASRock E350M1 AMD E-350 APU), a power supply (APEVIA ITX-AP250W) and a hard drive (ADATA SP900S3-64GB-C 64GB SSD) (see Figure A1).

This is mounted on the dish, in place of one of the mirror facets (Figure A2),

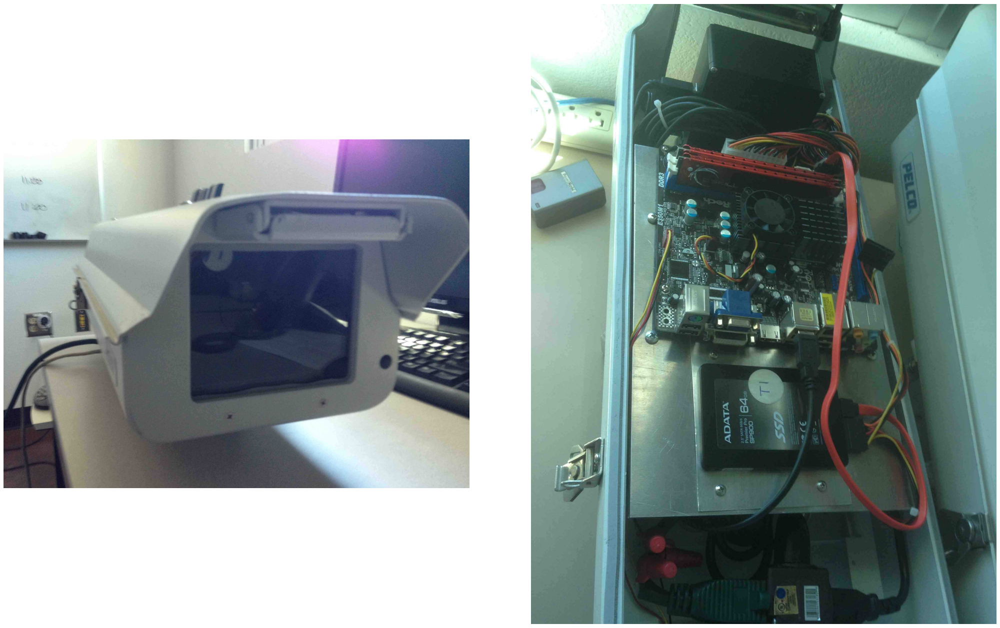

Figure A1: *Left:* Weatherproof PELCO box used for the reflectivity measurement. *Right:* Components of the reflectivity apparatus. From the front of the box (at the top of the image) is the SBIG camera, with the motherboard, CPU and hard drive installed behind it. The power supply sits below the metal plate, inside the box as well.

so that it can take a picture of both a star in the sky, and its reflection at the center of the PMT camera (Figure A3). Also visible in Figure A3 is a 20 cm-sided square target made from a fluoropolymer, called Spectralon (from Labsphere Inc.), installed at the center of the PMT camera. This polymer has a diffuse Lambertian reflectance greater than 99% over the wavelength of interest.

The reflectivity is found by getting a background-subtracted and vignetting-corrected sum of the pixel values of the CCD image of star (P_{star}) and of its reflection (P_{ref}) and calculating:

$$R_{mirror} = \left(\frac{P_{ref}}{P_{star}}\right) \pi d^2 / A_{mirror} \tag{A1}$$

Figure A2: Image of the reflectivity apparatus installed on one of the VERITAS Telescopes, in place of the mirror facet that would otherwise be mounted there.

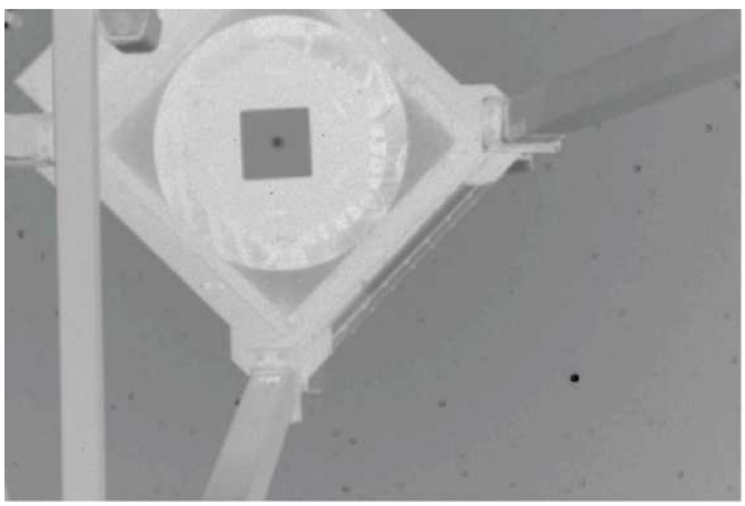

Figure A3: Example image taken by the reflectivity apparatus. Visible are the target star (brightest star on the lower right of the image) and the reflected image of that star (at the center of the PMT camera). The reflection sits on top of the Spectralon target, which reflects the light isotropically.

where d is the distance between the CCD camera and the Spectralon, and A_m is the area of the dish. The assumption is that the Spectralon's reflectivity is 100% and that the angle between the CCD camera and the star and its reflection are approximately zero.

Figure A4 shows the result from one set of pictures taken over 5 stars, for one telescope (T1). Each plot shows the results from a specific filter, as well as for the clear aperture. The reflectivity values are larger with the blue-filter data and smaller with the red-filter, as would be expected from the reflection spectrum of aluminium (recall that this is the material used to coat the mirrors). Note that the clear-aperture pictures' reflectivities have a larger spread than the filters', as the different stars have different spectra.

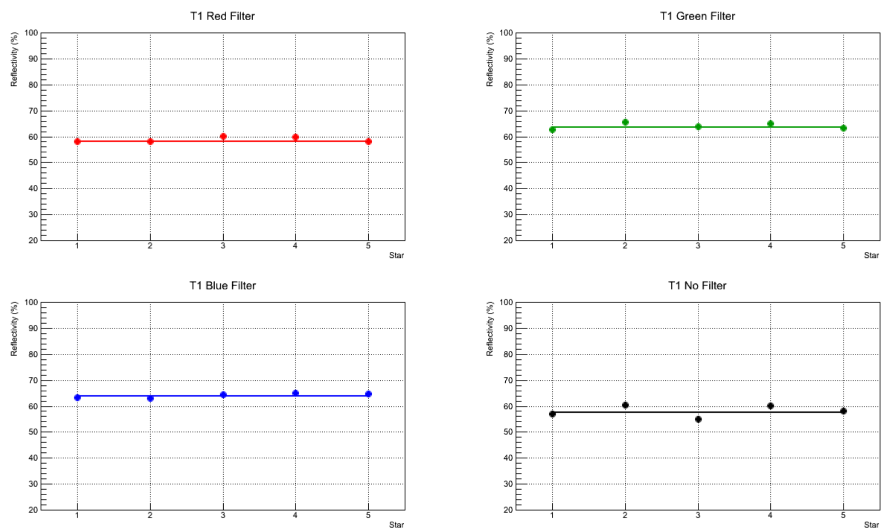

Figure A4: Example reflectivity results from telescope T1. The measured reflectivity is plotted against different stars (represented by the numbers on the x-axis) and the lines represent the average value. Statistical uncertainties are smaller than the symbol size. Each plot represents a different filter

These measurements are taken twice per observing periods (or dark runs), the period where data is being taken, between two Full Moons. The results are used to track the reflectivity of the mirrors. Figure A5 shows the long-term trend of these measurements for each telescope, using the blue filter, from January 1^{st} 2014, when the system was installed and stable, to today.

It is also an independent check of the value used in the simulations, required for the analysis of the data (as explained in the Chapter 6).

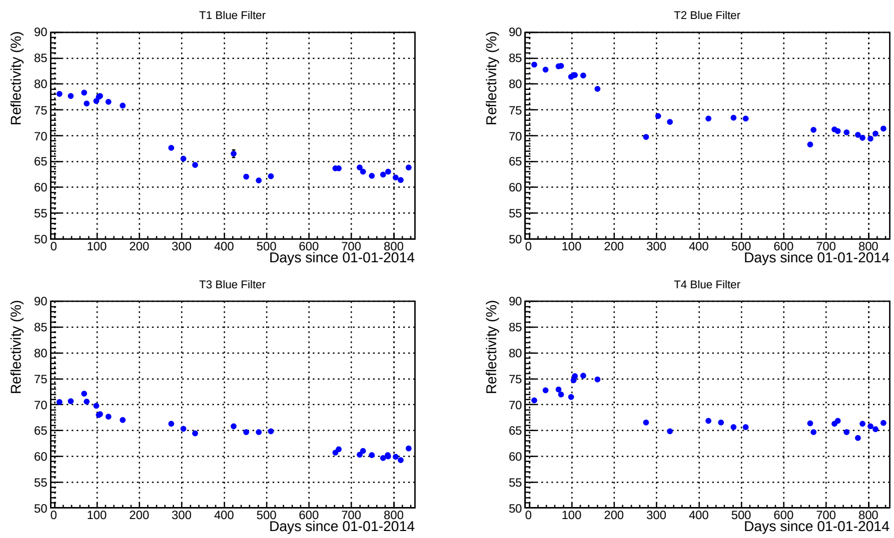

Figure A5: Long-term reflectivity of the telescopes with the blue filter. The gaps around days 200 and 600 are due to the summer shutdown, hence no measurements were taken. The mirror degradation over that time can be seen. Note that around day 100 the reflectivity goes up on T4, due to the replacement of a third of the mirror facets with recoated mirrors. The same effect can be seen around day 300 with T2.

References

[1] E. Aliu, S. Archambault, T. Aune, *et al.*, "A search for enhanced very high energy gamma-ray emission from the March 2013 Crab Nebula flare," *Astrophysical Journal*, vol. 781, no. L11, 2013.

[2] S.Hawking, "Gravitationally collapsed objects of very low mass," *Monthly Notices of the Royal Astronomical Society*, vol. 152, pp. 75–78, 1971.

[3] S. Hawking, "Black hole explosions?," *Nature*, vol. 248, p. 30, 1974.

[4] T. Weekes, *Very High Energy Gamma-Ray Astronomy*. IOP Publishing Ltd, 2003.

[5] V. Hess, "Concerning observations of penetrating radiation on seven free balloon flights," *Physikalische Zeitschrift*, vol. 13, pp. 1084–1091, 1912.

[6] L. Valcarcel, *VERITAS, 1ES1218+30.4 and the Extragalactic Background Light*. PhD thesis, McGill University, 2008.

[7] E. Fermi, "On the origin of the cosmic radiation," *Physical Review*, vol. 75, no. 8, 1949.

[8] M. Longair, *High Energy Astrophysics*. Cambridge University Press, 2011.

[9] W. Axford, E. Leer, and G. Skadron, "The acceleration of cosmic rays by shock waves," in *Proceedings of the* 15^{th} *International Cosmic Ray Conference*, vol. 11, pp. 132–135, 1977.

[10] D. Lennarz, "Search for very-high-energy gamma-ray emission from young supernovae," in *Proceedings of the* 33^{rd} *International Cosmic Rays Conference*, 2013.

[11] E. Lorenz and R. Wagner, "Very-high energy gamma-ray astronomy: A 23-year success story in high-energy astroparticle physics," *The European Physical Journal H*, vol. 37, no. 3, pp. 459–513, 2012.

[12] V. Ginzburg and S.I.Syrovatskii, "Cosmic magnetobremsstrahlung (synchrotron radiation)," *Annual Review of Astronomy and Astrophysics*, vol. 3, pp. 297–350, 1965.

[13] J. Aleksić, S. Ansoldi, and L. Antonelli, "Measurement of the Crab Nebula spectrum over three decades in energy with the MAGIC telescopes," *Journal of High Energy Astrophysics*, vol. 5, pp. 30–38, 2015.

[14] K. Olive *et al.*, *Particle Data Group*, vol. 38. Chin. Phys. C, 2014.

[15] W. Atwood, A. Abdo, M. Ackermann, *et al.*, "The large area telescope on the Fermi gamma-ray space telescope mission," *Astrophysical Journal*, vol. 697, pp. 1071–1102, 2009.

[16] F. Aharonian, A. Akhperjanian, U. B. de Almeida, *et al.*, "The energy spectrum of cosmic-ray electrons at TeV energies," *Physical Review Letters*, vol. 101, p. 261104, 2008.

[17] N. Gerson, "Variations in the index of refraction of the atmosphere," *Geofisica pura e applicata*, vol. 13, pp. 88–101, 1948.

[18] A. Einstein and M. Grossmann, "Outline of a generalized theory of relativity and of a theory of gravitation," *Zeitschrift für Mathematik und Physik*, vol. 62, 1913.

[19] K. Schwarzschild, "On the gravitational field of a mass point according to Einstein's theory," *Sitzungsberichte der Königlich Preussischen Akademie der Wissenschaften zu Berlin*, vol. 7, pp. 189–196, 1916.

[20] W. Israel, "Event horizons in static vaccum space-times," *Physical Review*, vol. 164, 1967.

[21] J. R. Oppenheimer and H. Snyder, "On continued gravitational contraction," *Physical Review*, vol. 56, pp. 455–459, 1939.

[22] S. Chandrasekhar, "The maximum mass of ideal white dwarfs," *Astrophysical Journal*, vol. 74, pp. 81–82, 1931.

[23] I. Bombaci, "The maximum mass of a neutron star," *Astronomy and Astrophysics*, vol. 305, pp. 871–877, 1996.

[24] W. Fechner and P. Joss, "Quark star with 'realistic' equations of state," *Nature*, vol. 274, pp. 347–349, 1978.

[25] S. Bowyer, E. Byram, T. Chubb, *et al.*, "Cosmic x-ray sources," *Science*, vol. 147, no. 3656, pp. 394–398, 1965.

[26] J. Ziolkowski, "Determination of the masses of the components of the HDE 226868/Cyg X-1 binary sysem," *Monthly Notices Letters of the Royal Astronomical Society*, vol. 440, pp. L61–L65, 2014.

[27] R. Rothschild, E. Boldt, S. Holt, *et al.*, "Millisecond temporal structure in Cygnus X-1," *The Astrophysical Journal*, vol. 189, pp. L13–L16, 1974.

[28] K. Brecher and P.Morrison, "Rapidly rotating degenerate dwarfs as x-ray sources in binaries," *Astrophysical Journal*, vol. 180, pp. L107–L112, 1973.

[29] A. Fabian, J. Pringle, and J. Whelan, "Is Cyg X-1 a neutron star?," *Nature*, vol. 247, pp. 351–352, 1973.

[30] H. Shipman, "The implausible history of triple star models for Cygnus X-1: Evidence for a black hole," *Astrophysical Letters*, vol. 16, pp. 9–12, 1975.

[31] T. Shahbaz, F. Ringwald, J. Bunn, *et al.*, "The mass of the black hole in V404 Cygni," *Monthly Notices of the Royal Astronomical Society*, vol. 271, no. 1, pp. L10–L14, 1994.

[32] R. Hynes, D. Steeghs, J. Casares, *et al.*, "Dynamical evidence for a black hole in GX 339-4," *Astrophysical Journal*, vol. 583, pp. L95–L98, 2003.

[33] D. Gelino, T. Harrison, and J. Orosz, "A multiwavelength, multiepoch study of the soft x-ray transient prototype, V616 Mon (A0620-00)," *The Astronomical Journal*, vol. 122, no. 5, pp. 2668–2678, 2001.

[34] B.P.Abbott *et al.*, "Observation of gravitational waves from a binary black hole merger," *Physical Review Letters*, vol. 116, no. 061102, 2016.

[35] B. Abbott *et al.*, "Gw151226: Observation of gravitational waves from a 22-solar-mass binary black hole coalescence," *Physical Review Letters*, vol. 116, no. 241103, 2016.

[36] A. Celotti, J. Miller, and D. Sciama, "Astrophysical evidence for the existence of black holes," *Classical and Quantum Gravity*, vol. 16, no. 12A, p. 301, 1999.

[37] J. Walsh, A. Barth, L. Ho, *et al.*, "The M87 black hole mass from gas-dynamical models of space telescope imaging spectrograph observations," *The Astrophysical Journal*, vol. 770, no. 2, pp. 86–97, 2013.

[38] F. Eisenhauer, R. Genzel, T. Alexander, *et al.*, "SINFONI in the galactic center: Young stars and IR flares in the central light month," *The Astrophysical Journal*, vol. 638, pp. 246–259, 2005.

[39] M. Volonteri, "Astrophysics: Making black holes from scratch," *Nature*, vol. 466, pp. 1049–1050, 2010.

[40] M. Begelman, M. Volonteri, and M. Rees, "Formation of supermassive black holes by direct collapse in pregalactic halos," *Monthly Notices of the Royal Astronomical Society*, vol. 370, pp. 289–298, 2006.

[41] R. van der Marel, "Intermediate-mass black holes in the universe: A review of formation theories and observational constraints," *Carnegie Observatories Astrophysics Series*, vol. 1, p. 37, 2003.

[42] B. Peterson, M. Bentz, L.-B. Desroches, *et al.*, "Multiwavelength monitoring of the dwarf Seyfert 1 galaxy NGC 4395. 1. a reverberation-based measurement of the black hole mass," *The Astrophysical Journal*, vol. 632, pp. 799–808, 2005.

[43] M. Krauss, R. Kilgard, M. Garcia, *et al.*, "M74 X-1 (CXOU J013651.1+154547): An extremely variable ultraluminous x-ray source," *The Astrophysical Journal*, vol. 630, pp. 228–237, 2005.

[44] K. Gebhardt, R. Rich, and L. Ho, "An intermediate-mass black hole in the globular cluster G1: Improved significance from New Keck and Hubble space telescope observations," *The Astrophysical Journal*, vol. 634, pp. 1034–1102, 2005.

[45] B. Carr and S. Hawking, "Black holes in the early universe," *Monthly Notices of the Royal Astronomical Society*, vol. 168, pp. 399–416, 1974.

[46] J. Niemeyer and K. Jedamzik, "Near-critical gravitational collapse and the initial mass function of primordial black holes," *Physical Review Letters*, vol. 80, no. 25, pp. 5481–5484, 1998.

[47] A. Green, A. Liddle, K. Malik, *et al.*, "New calculation of the mass fraction of primordial black holes," *Physical Review D*, vol. 70, no. 041502, 2004.

[48] B. Carr, "Primordial black holes as a probe of cosmology and high energy physics," *Lecture Notes in Physics*, vol. 631, pp. 301–321, 2003.

[49] H. Kim, C.H.Lee, and J. MacGibbon, "Diffuse gamma-ray background and primordial black hole constraints on the spectral index of density fluctuations," *Physical Review D*, vol. 59, no. 063004, 1999.

[50] B. Carr and J. Lidsey, "Primordial black holes and generalized constraints on chaotic inflation," *Physical Review D*, vol. 48, pp. 543–553, 1993.

[51] P. Nasel'skii, "Hydrogen recombination kinetics in the presence of low-mass primordial black holes," *Soviet Astronomy Letters*, vol. 4, pp. 387–392, 1978.

[52] Y. Zeldovich and A. Starobinskii, "Possibility of a cold cosmological singularity in the spectrum of primordial black holes," *JETP Letters*, vol. 24, no. 11, pp. 571–573, 1976.

[53] J. Barrow, "The baryon asymmetry of the universe," *Surveys in High Energy Physics*, vol. 1, no. 3, pp. 183–212, 1980.

[54] B. Vainer, O. Dryzhakova, and P. Naselskii, "Primordial black holes and cosmological nucleosynthesis," *Soviet Astronomy Letters*, vol. 4, pp. 185–187, 1978.

[55] M. Hawkins, "The case for primordial black holes as dark matter," *Monthly Notices of the Royal Astronomical Society*, vol. 415, no. 3, 2011.

[56] P. Tisserand, L. L. Guillou, C. Afonso, *et al.*, "Limits on the MACHO content of the galactic halo from the EROS-2 survey of the Magellanic Clouds," *Astronomy and Astrophysics*, vol. 469, 2007.

[57] M. Ricotti, J. Ostriker, and K. Mack, "Effect of primordial black holes on the cosmic microwave background and cosmological parameter estimates," *The Astrophysical Journal*, vol. 680, no. 2, 2008.

[58] P. Pani and A. Loeb, "Tidal capture of a primordial black hole by a neutron star: Implications for constraints on dark matter," *Journal of Cosmology and Astroparticle Physics*, vol. 2014, 2014.

[59] S. Hawking, "Black holes from cosmic strings," *Physics Letters B*, vol. 231, no. 3, pp. 237–239, 1989.

[60] S. Hawking, I. Moss, and J. Stewart, "Bubble collisions in the very early universe," *Physical Review D*, vol. 26, no. 10, pp. 2681–2693, 1982.

[61] J. Beckenstein, "Black holes and entropy," *Physical Review D*, vol. 7, no. 8, pp. 2333–2346, 1973.

[62] J. MacGibbon and B. Webber, "Quark- and gluon-jet emission from primordial black holes: The instantaneous spectra," *Physical Review D*, vol. 41, no. 10, pp. 3052–3079, 1990.

[63] T. Ukwatta, D. Stump, J. Linnemann, *et al.*, "Primordial black holes: Observational characteristics of the final evaporation," *Astroparticle Physics Journal*, Submitted.

[64] J. MacGibbon, "Quark- and gluon-jet emission from primordial black holes. ii. the emission over the black-hole lifetime," *Physical Review D*, vol. 44, no. 2, pp. 376–392, 1991.

[65] M. Vivier, *Observations du Centre Galactique et recherche de signaux exotiques avec H.E.S.S.* PhD thesis, Université de Paris XI, 2009.

[66] C. Hill, "Monopolonium," *Nuclear Physics B*, vol. 224, pp. 469–490, 1983.

[67] F.Halzen, E.Zas, J.H.MacGibbon, *et al.*, "Gamma rays and energetic particles from primordial black holes," *Nature*, vol. 353, pp. 807–815, 1991.

[68] V. Petkov, E. Bugaev, P. Klimai, *et al.*, "Searching for very-high-energy gamma-ray bursts from evaporating primordial black holes," *Astronomy Letters*, vol. 34, pp. 509–514, 2008.

[69] J. Bellm, S. Gieseke, D. Grellscheid, *et al.*, "HERWIG++ 2.7 release note," *ArXiv 1310.6877*, 2013.

[70] A. Abdo, A. Abeysekara, R. Alfaro, *et al.*, "Milagro limits and HAWC sentivity for the rate-density of evaporating primordial black holes," *Astroparticle Physics*, vol. 64, pp. 4–12, 2015.

[71] R.Hagedorn, "Statistical thermodynamics of strong interactions at high-energy," *Nuovo Cimento Suppl*, vol. 3, p. 147, 1965.

[72] K.Huang and S. Weinberg, "Ultimate temperature and the early universe," *Physical Review Letters*, vol. 25, no. 13, pp. 895–897, 1970.

[73] E. Dwek and F. Krennrich, "The extragalactic background light and the gamma-ray opacity of the universe," *Astroparticle Physics*, vol. 43, pp. 112–133, 2013.

[74] B. Czerny, A. Janiuk, D. Cline, *et al.*, "Observational constraints on the nature of very short gamma-ray bursts," *New Astronomy*, vol. 16, pp. 33–45, 2011.

[75] S. Barthelmy, L. Barbier, J. Cummings, *et al.*, "The burst alert telescope (BAT) on the SWIFT Midex mission," *Space Science Reviews*, vol. 120, no. 3-4, pp. 143–164, 2005.

[76] D. Cline, S. Otwinowski, and B. Czerny, "Do very short gamma ray bursts originate from primordial black holes? review," *International Journal of Astronomy and Astrophysics*, vol. 1, pp. 164–172, 2011.

[77] J. Bains, "Searching for evaporating primordial black holes using Fermi gamma ray telescope data," Master's thesis, Imperial College London, 2011.

[78] R. Lehoucq, M. Casse, J. Casandjian, *et al.*, "New constraints on the primordial black hole number density from galactic gamma-ray astronomy," *Astronomy and Astrophysics*, vol. 502, pp. 37–43, 2009.

[79] J.Kildea, R. Atkins, H. Badran, *et al.*, "The Whipple observatory 10 m gamma-ray telescope, 1997-2006," *Astroparticle Physics*, vol. 28, pp. 182–195, 2007.

[80] E.T.Linton, *A Search for Primordial Black Holes and a Study of Spectral Variation in Markarian 421 Using the Whipple 10-M Telescope*. PhD thesis, University of Chicago, 2006.

[81] M. Schroedter, F. Krennrich, S. LeBohec, *et al.*, "Search for primordial back holes with SGARFACE," *Astroparticle Physics*, vol. 31, pp. 102–115, 2009.

[82] C. Fichtel, D. Bertsch, B. Dingus, *et al.*, "Search of the energetic gamma-ray experiment telescope (EGRET) data for high-energy gamma-ray microsecond bursts," *The Astrophysical Journal*, vol. 434, pp. 557–559, 1994.

[83] N. Porter and T. Weekes, "A search for high energy gamma-ray bursts from primordial black holes or other astronomical objects," *Monthly Notices of the Royal Astronomical Society*, vol. 183, pp. 205–210, 1978.

[84] D. Cline, D. Sanders, and W. Hong, "Further evidence for some gamma-ray bursts consistent with primordial black hole evaporation," *Astrophysical Journal*, vol. 486, pp. 169–178, 1997.

[85] B. Carr and J. MacGibbon, "Cosmic rays from primordial black holes and constraints on the early universe," *Physics Reports*, vol. 307, pp. 141–154, 1998.

[86] K. Maki, T. Mitsui, and S. Orito, "Local flux of low-energy antiprotons from evaporating primordial black holes," *Physical Review Letters*, vol. 76, pp. 3474–3477, 1996.

[87] E. Wright, "On the density of primordial black holes in the galactic halo," *Astrophysical Journal*, vol. 459, p. 487, 1996.

[88] G.Tešić, "Searching for primordial black holes with the VERITAS gamma-ray experiment," in *Journal of Physics: Conference Series*, vol. 375, 2012.

[89] K. Bernloehr, O. Carrol, R. Cornils, *et al.*, "The optical system of the H.E.S.S. imaging atmospheric Cherenkov telescopes, part 1: layout and components of the system," *Astroparticle Physics*, vol. 20, pp. 111–128, 2003.

[90] J. Glicenstein, A. Barnacka, M. Vivier, *et al.*, "Limits on primordial black hole evaporation with the H.E.S.S. array of Cherenkov telescopes," in *Proceedings of the 33rd International Cosmic Rays Conference*, 2013.

[91] M. de Naurois and L. Rolland, "A high performance likelihood reconstruction of gamma-rays for imaging atmospheric Cherenkov telescopes," *Astroparticle Physics*, vol. 32, pp. 231–252, 2009.

[92] A. Abdo, B. Allen, and T. Aune, "Observation and spectral measurement of the Crab Nebula with Milagro," *The Astrophysical Journal*, vol. 750, no. 1, 2012.

[93] A. Abeysekara, J. Aguilar, S. Aguilar, *et al.*, "On the sensitivity of the HAWC observatory to gamma-ray bursts," *Astroparticle Physics*, vol. 35, no. 10, pp. 641–650, 2012.

[94] J. Davies and E. Cotton, "Design of the quartermaster solar furnace," *Solar Energy*, vol. 1, no. 2-3, pp. 16–22, 1957.

[95] F. Krennrich, I. Bond, P. Boyle, *et al.*, "VERITAS: The very energetic radiation imaging telescope array system," *New Astronomy Reviews*, vol. 48, no. 5-6, pp. 345–349, 2004.

[96] R. Winston, "Light collection within the framework of geometrical optics," *Journal of the Optical Society of America*, vol. 60, no. 2, pp. 245–247, 1970.

[97] B. Zitzer, "The VERITAS upgraded telescope-level trigger systems: Technical details and performance characterization," in *Proceedings of the 33rd International Cosmic Ray Conference*, 2013.

[98] A. Weinstein, "The VERITAS trigger system," in *Proceedings of the 30th International Cosmic Ray Conference*, 2007.

[99] D. Hanna, A. McCann, M. McCutcheon, *et al.*, "An LED-based flasher system for VERITAS," *Nuclear Instruments and Methods in Physics Reasearch Section A*, vol. 612, no. 2, pp. 278–287, 2010.

[100] A. Hillas, "Cerenkov light images of EAS produced by primary gamma rays and by nuclei," in *19th International Cosmic Ray Conference*, vol. 3, pp. 445–448, 1985.

[101] S. Lebohec, C. Duke, and P. Jordan, "Minimal stereoscopic analysis for imaging atmospheric Cherenkov telescope arrays," *Astroparticle Physics*, vol. 24, pp. 26–31, 2005.

[102] G. Maier, "Monte carlo studies of the VERITAS array of Cherenkov telescopes," in *Proceedings of the 30th International Cosmic Ray Conference*, 2007.

[103] F. Aharonian, A. Akhperjanian, J. Barrio, *et al.*, "The temporal characteristics of the TeV gamma-radiation from MKN 501 in 1997. I. Data from the stereoscopic imaging atmospheric Cherenkov telescope system of HEGRA," *Astronomy and Astrophysics*, vol. 342, pp. 69–86, 1999.

[104] M. Daniel, "The VERITAS standard data analysis," in *Proceedings of the 30th International Cosmic Ray Conference*, 2007.

[105] T. Li and Y. Ma, "Analysis methods for results in gamma-ray astronomy," *Astrophysical Journal*, vol. 272, pp. 317–324, 1983.

[106] M. Meyer, D. Horns, and H.-S. Zechlin, "The Crab Nebula as a standard candle in very high-energy astrophysics," *Astronomy and Astrophysics*, vol. 523, p. A2, 2010.

[107] V. Vasileiou, *A search for bursts of very high energy gamma rays with Milagro*. PhD thesis, University of Maryland, 2008.

[108] D.Staszak, A. Abeysekara, S. Archambault, *et al.*, "Science highlights from VERITAS," in *Proceedings of the 34th International Cosmic Ray Conference*, 2015.

[109] K. Meagher, "Six years of VERITAS observations of the Crab Nebula," in *Proceedings of the 34^{th} International Cosmic Ray Conference*, 2015.

[110] A. Zerbet and M. Nikulin, "A new statistic for detecting outliers in exponential case," *Communications in Statistics - Theory and Methods*, vol. 32, no. 3, 2003.

[111] J. MacGibbon and B. Carr, "Cosmic rays from primordial black holes," *Astrophysical Journal*, vol. 371, pp. 447–469, 1991.

[112] A. Barrau, D. Blais, G. Boudoul, *et al.*, "Galactic cosmic rays from PBHs and primordial spectra with a scale," *Physics Letters B*, vol. 551, pp. 218–225, 2003.

[113] J. Chisholm, "Clustering of primordial black holes: basic results," *Physical Review D*, vol. 73, no. 083504, 2006.

[114] J. MacGibbon, T. Ukwatta, J. Linnemann, *et al.*, "Primordial black holes," in *Proceedings of the 5^{th} Fermi Symposium*, 2014.

[115] M. Actis, G. Agnetta, F. Aharonian, *et al.*, "Design concepts for the Cherenkov Telescope Array (CTA), an advanced facility for ground-based high-energy gamma-ray astronomy," *Experimental Astronomy*, vol. 32, pp. 193–316, 2011.

[116] R. Mirzoyan, M. Garczarcyk, and D. Paneque, "A method to measure the mirror reflectivity of a prime focus telescope," *Astroparticle Physics*, vol. 27, no. 6, pp. 509–511, 2007.

[117] E. Roache, R. Irvin, J. Perkins, *et al.*, "Mirror facets for the VERITAS telescopes," in *Proceedings of the 30^{th} International Cosmic Ray Conference*, 2007.

KEY TO ABBREVIATIONS

AGN: Active Galactic Nuclei

ANN: Artificial Neural Network

BATSE: Burst and Transient Source Experiment

BDT: Boosted Decision Tree

CAP: Canadian Association of Physicists

CCD: Charge-Coupled Device

CDM: Cold Dark Matter

CFD: Charge Fraction Discriminator

CGRO: Compton Gamma Ray Observatory

CL: Confidence Level

CRAQ: Centre de Recherche en Astrophysique du Québec

d.c.: digital counts

DEC: Declination

DQM: Data-Quality Monitoring

EBL: Extragalactic Background Light

EGRET: Energetic Gamma Ray Experiment Telescope

FADC: Flash Analog-to-Digital Converter

FIR: Far-Infrared

FLWO: Fred Lawrence Whipple Observatory

FPGA: Field Programmable Gate Array

GRB: Gamma-Ray Burst

HAWC: High-Altitude Water Cherenkov Observatory

HERWIG: Hadron Emission Reactions With Interfering Gluons

H.E.S.S.: High Energy Stereoscopic System

IACT: Imaging Array of Cherenkov Telescope

ICRC: International Cosmic Ray Conference

IRF: Instrument Response Function

IMBH: Intermediate-Mass Black Hole

LAT: Large Area Telescope

LED: Light-Emitting Diode

MACHO: Massive Compact Halo Object

MAGIC: Major Atmospheric Gamma Imaging Cherenkov

MSCL: Mean Reduced Scaled Length

MSCP: Mean Reduced Scaled Parameter

MSCW: Mean Reduced Scaled Width

MSL: Mean Scaled Length

MSP: Mean Scaled Parameter

MSW: Mean Scaled Width

NASA: National Aeronautics and Space Administration

NSB: Night Sky Background

NSERC: National Scientific and Engineering Research Council

OSS: Optical Support Structure

PBH: Primordial Black Hole

PMT: PhotoMultiplier Tube

PQE: Peak Quantum Efficiency

PSF: Point Spread Function

QCD: Quantum Chromodynamics

RMS: Root-Mean-Square

RA: Right Ascension

RF: Random Forest

SAO: Smithsonian Astrophysical Observatory

SBIG: Santa Barbara Instrument Group

SGARFACE: Short Gamma-Ray Front Air-Cherenkov Experiment

S/N: Signal-to-Noise

UV: Ultraviolet

VERITAS: Very Energetic Radiation Imaging Telescope Array System

VHE: Very High Energy

VSGRB: Very Short Gamma-Ray Burst

WMAP: Wilkinson Microwave Anisotropy Probe